

From polymer chains to enzyme-mimetic soft nanoparticles

Irma Perez Baena

Donostia-San Sebastián 2014

eman ta zabal zazu



Universidad
del País Vasco

Euskal Herriko
Unibertsitatea

CFM CFM CFM
CFM CFM CFM
CFM CFM CFM

Materialen Fisika Zentroa

Materials Physics Center

Centro de Física de Materiales

Agradecimientos

Quisiera agradecer en primer lugar a Juan Colmenero , por darme la oportunidad de trabajar en el grupo de “Polymers and Soft Matter”, donde he tenido la oportunidad de trabajar en un proyecto muy interesante.

Quisiera agradecer especialmente a mi director de Tesis, Josetxo Pomposo, por su ayuda constante y seguimiento diario de mi trabajo. Quisiera agradecerle también la cercanía y disponibilidad mostradas durante todos estos años.

Tengo mucha gente a la que agradecer esta tesis.

Zurekin hasiko naiz, Ibon. Euskera batuan idaztia gustatze etzaizunez, zarauztarrez idatzikoet. Asko eskertzeizut tesi garaian eskeini diazun laguntza guztiya ta aukiezun pazientziya. Baño benetan eskertzeizutena, nere onduan eontzean denbora guztiya da.

A lo largo de estos años trabajando aquí, he tenido la oportunidad de conocer a gente muy especial. Primero quiero nombrar a Lorea y a Lourdes, que aunque no estén ahora aquí, las considero imprescindibles. Pueden pasar meses sin hablar con ellas, pero cuando lo hago es como si no hubiese pasado el tiempo.

Que haría yo sin mis nadadores favoritos, Luisa y Manuel. No sé cómo explicar todo lo que me han ayudado. En mis momentos malos, que han sido bastantes, siempre he tenido la confianza de ir a donde ellos para contarles todo lo que se me pasaba por la cabeza. También os agradezco todos los momentos buenos que me hacéis pasar, me encanta estar con vosotros, no lo podéis imaginar... Tenéis una amiga para toda la vida. Isabel, otro gran apoyo para mi, eres una persona increíble y sabes escuchar, a mi me has ganado para siempre. La verdad que el grupo “los poliméricos” será difícil de superar; Natalia, Izaskun, Marina, Alex, Ana, Alicja, Luciana, Ana Lucia... gracias a todos por ser como sois. Tampoco me olvido de Itziar, Giuseppe y Gerardo.

Por último quiero agradecer a mis padres, a mi hermano, a Vanesa y a mis tías Teresa y Conchi por quererme tal y como soy y por aguantarme todo este tiempo porque sé que muchas veces se necesita mucha paciencia.

CONTENTS

CHAPTER 1. MOTIVATIONS, GOALS AND METHODOLOGY	1
1.1. Motivation of this work	3
1.1.1. Nanoparticles (NPs)	3
1.1.2. Polymer nanoparticles	4
1.1.3. Single-chain polymer nanoparticles (SCNPs)	5
1.2. Goals and methodology	6
1.2.1. Scaling laws of SCNPs	7
1.2.2. Mimicking enzyme behavior with SCNPs	7
1.2.3. Photoactivated synthesis of SCNPs through thiol-ene and thiol-yne coupling reaction	7
1.3. Structure of this text	8
1.4. References	9
CHAPTER 2. FUNDAMENTAL ASPECTS	11
2.1. Synthesis of single-chain polymer nanoparticles (SCNPs)	13
2.1.1. Precursor synthesis	13
A. Free radical polymerization (FRP)	14
B. Controlled radical polymerization (CRP)	16
C. Reversible addition fragmentation chain transfer (RAFT) polymerization	16
D. Redox initiated RAFT polymerization	20
2.1.2. Polymer functionalization	21
2.1.3. Intrachain folding/collapse techniques for the synthesis of SCNPs	22
A. Intrachain homocoupling	22
B. Intrachain heterocoupling	22
C. Cross-linker induced collapse	23
2.2. Characterization techniques of polymer precursors and SCNPs	25
A. Molecular weight and polydispersity index	25
B. Dimensional characterization techniques	25
C. Structural characterization techniques	26
D. Thermal characterization techniques	26
2.2.1. Size Exclusion Chromatography (SEC)	26
2.2.2. Nuclear Magnetic Resonance (NMR) Spectroscopy	27
2.2.3. Dynamic Light Scattering (DLS)	27

2.2.4.	Fourier Transform Infrared Spectroscopy (FTIR)	28
2.2.5.	Thermal Gravimetric Analysis (TGA)	28
2.2.6.	Differential Scanning Calorimetry (DSC)	29
2.2.7.	Atomic Force Microscopy (AFM)	29
2.2.8.	Transmission Electron Microscopy (TEM)	30
2.2.9.	X-Ray Photoelectron Spectroscopy (XPS)	30
2.2.10.	Small Angle Neutron Scattering (SANS)	30
2.2.11.	Small Angle X-Ray Scattering (SAXS)	31
2.2.12.	Elemental Analysis (EA)	32
2.3.	Modeling and simulation	32
2.3.1.	Molecular dynamics	33
2.3.2.	Bead-spring model of isolated polymers	34
2.3.3.	Modeling the effects of the solvent	35
2.4.	References	37
 CHAPTER 3. SCALING LAWS FOR APPARENT MOLECULAR WEIGHT, APPARENT POLYDISPERSITY INDEX, HYDRODYNAMIC RADIUS AND INTRINSIC VISCOSITY IN SCNPs		41
3.1.	Introduction and objectives	43
3.2.	Apparent molecular weight and polydispersity reduction upon intramolecular collapse of polydisperse chains to unimolecular nanoparticles	45
3.2.1.	Introduction and objectives	45
3.2.2.	Apparent molecular weight decrease upon unimolecular nanoparticle formation	46
A.	Theory	46
B.	Results	48
3.2.3.	Apparent polydispersity narrowing upon unimolecular nanoparticle formation	53
A.	Theory	53
B.	Results	54
3.2.4.	Conclusions	56
3.3.	How far are single-chain polymer nanoparticles in solution from the globular state?	58
3.3.1.	Introduction and objectives	58
A.	Results	59
3.3.2.	Conclusions	71
3.4.	SCNPs vs. star, hyperbranched and dendrimeric polymers: Effect of nanoscopic architecture on the flow properties of diluted solutions	72

3.4.1.	Introduction and objectives	72
3.4.2.	Obtaining of a scaling power-law between $[\eta]$ and M	73
3.4.3.	Comparison between η_{calc} and η_{exp} for SCNPs of different chemical nature	75
3.4.4.	Comparison of the intrinsic viscosity of SCNPs vs. star, hyperbranched and dendrimeric polymers	77
3.4.5.	Conclusions	79
3.5.	References	81

CHAPTER 4. ENDOWING SCNPS WITH ENZYME-MIMETIC ACTIVITY **87**

4.1.	Introduction, objectives and methodology	89
4.2.	Experimental part	90
4.2.1.	Reagents	90
4.2.2.	Synthesis of high molecular weight P(BzMA-co-GMA) (P1) and P(CHMA-co-GMA) (P3) copolymers ($M_w > 1000$ kDa)	91
4.2.3.	Synthesis of low molecular weight P(BzMA-co-GMA) (P2) and P(CHMA-co-GMA) (P4) copolymers ($M_w < 100$ kDa)	91
4.2.4.	Synthesis of SCNPs from polymer precursors	92
4.2.5.	Reductase properties of SCNPs	93
4.2.6.	Polymerase-like properties of SCNPs: polymerization of THF	94
4.2.7.	Synthesis of poly(glycidyl phenyl ether) (poly(GPE))	94
4.3.	Results and discussion	94
4.3.1.	Synthesis of linear polymer precursors	94
4.3.2.	Synthesis of SCNPs	96
4.3.3.	Characterization of polymer precursors and SCNPs	96
4.3.4.	Molecular dynamics (MD) simulations and small angle neutron scattering (SANS) measurements	101
4.3.5.	Catalytic activity of SCNPs	104
4.4.	Conclusions	109
4.5.	References	110

CHAPTER 5. PHOTOACTIVATED SYNTHESIS OF COMPACT SCNPs VIA THIOL-YNE COUPLING REACTION **113**

5.1.	Introduction, objectives and methodology	115
5.2.	Experimental part	117

5.2.1.	Reagents	117
5.2.2.	Synthesis of P(MMA-AMA) precursor (P5)	117
5.2.3.	Synthesis of P(MMA-PGA) precursor (P6)	117
5.2.4.	Photoactivated synthesis of SCNPs through TEC/TYC reactions	118
5.3.	Results and discussion	119
5.3.1.	Synthesis of linear polymer precursors	119
5.3.2.	Photoactivated synthesis of SCNPs	120
5.3.3.	Characterization of polymer precursors and SCNPs	121
5.3.4.	Molecular dynamic (MD) simulations and small angle X-ray scattering (SANS)	130
5.4.	Conclusions	138
5.5.	References	140
CHAPTER 6. CONCLUSIONS		143
APENDIX I. SIZE EXCLUSION CHROMATOGRAPHY		149
7.1.	Size Exclusion Chromatography (SEC)	151
7.1.1.	Molecular weight and SEC	153
7.1.2.	Direct calibration	153
7.1.3.	Universal calibration	155
7.1.4.	SEC as a direct technique for the determination of molecular weights	156
7.1.5.	Complementary techniques to SEC	156
7.2.	References	158

Chapter 1. Motivations, goals and methodology

1.1. Motivation of this work

1.1.1. Nanoparticles (NPs)

Nanoparticles are typically defined as objects with a size in the range of 1 - 100 nm, at least in one of the three spatial dimensions. Against all intuition, while at the macroscopic scale, a material has the same physical, electrical, mechanical and chemical properties, regardless of its size, at the nanoscale this is not often the case. The properties at the nanoscale are often different from those of the corresponding bulk material because of two reasons. In first place at the nanoscale there is a significant increase in the number of atoms at the surface with respect to the total number of atoms in the particle. Surface atoms have different coordination (i.e. number of chemical bonds) and therefore strongly influence the chemistry and physics of the system if their proportion increases. The second reason is that at the nanoscale the relatively reduced numbers of atoms make the collective effects less important, in favor of individual effects, governed by the quantum laws of the microscopic world.

As it is not possible to anticipate nanoparticle properties from a simple extrapolation of the properties of the bulk material, the exploration of the world of nanoparticles has led to a full area of research on its own, with contributions from many others. This new area of knowledge is vast. The reason lies in the immense variety of the nanoparticles that come up from their wide chemical nature, shapes and morphologies, the medium in which the particles are present, the state of dispersion and, the numerous possible modifications that can be done in order to tune and meet the needs from specific applications^[1] (see Figure 1.1). This large choice of possibilities and the variety of new properties has enabled many applications. Just to name a few examples: titanium dioxide nanoparticles are widely used as pigment in paints^[2] but also in sunscreens^[3] because their strong UV light absorbing capabilities. Polymer nanoparticles, composed of a cross-linked core and elastomeric shell, are used as reinforcing agents and performance-enhancing additives in rubber vulcanizates.^[4] Silver nanoparticles are used extensively as anti-bacterial agents in the health industry, food storage, textile coatings and a number of environmental applications.^[5] Although bulk gold is chemically inert and is regarded as poor catalyst, when gold is in very small particles with diameters below 10 nm and is deposited on metal oxides or active carbon, it becomes surprisingly active for many reactions such as CO oxidation and propylene epoxidation.^[6]

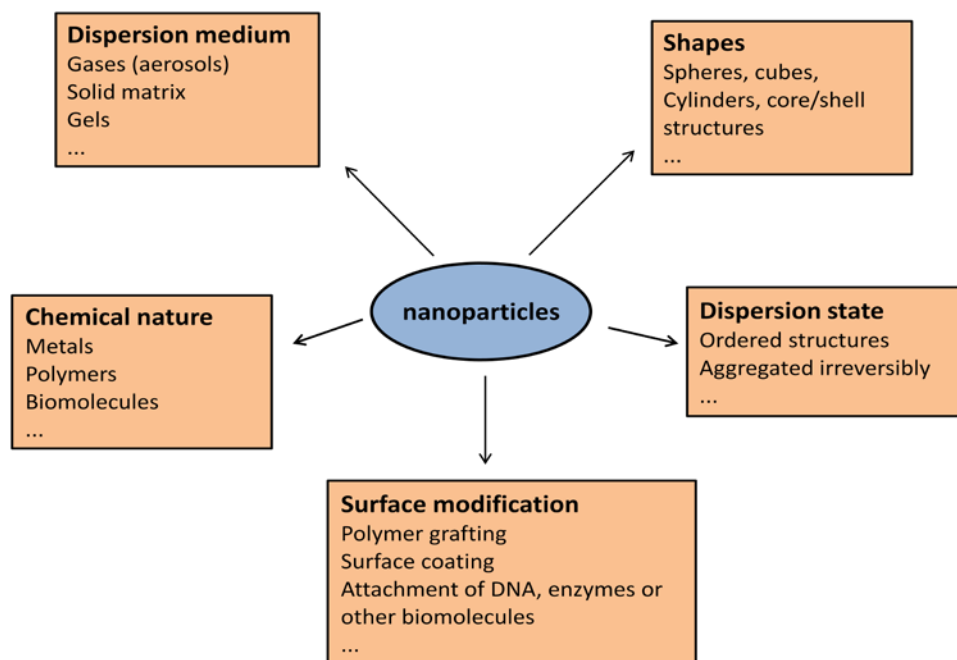


Figure 1.1. Various features contributing to the diversity of engineered nanoparticles.

It is worth mentioning that the transition from concept and laboratory model to real life applications will depend critically in the capacity to manufacture large quantities of nanoparticles in an economical, robust and reproducible way. Because of this, certain types of nanoparticles are gaining importance and the processes by which they are synthesized are receiving strong attention.

1.1.2. Polymer nanoparticles

In recent years, polymeric nanoparticles have attracted significant attention due to their numerous applications in different areas such as electronics,^[7] coatings^[8] and drug delivery,^[9,10] to name only a few. This type of particles is also attractive because they can be fabricated employing robust and versatile chemical processes, based either in transforming a wide variety of commercially available polymers, or in synthesizing from appropriate monomers. Furthermore, the nanoparticles can be modified at a later stage through functionalization processes, which allow enabling new properties.

The various methods employed for synthesis of polymer nanoparticles are often classified into two classes. On one hand, top-down techniques use preformed polymers, which are dispersed into a colloidal suspension in order to form nano-sized particles. On the other hand, bottom-up techniques follow the approach of synthesizing nanoparticles from monomers.^[11] The morphology, structure and size of the resulting nanoparticle largely depend in the fabrication method employed.

1.1.3. Single-chain polymer nanoparticles (SCNPs)

Single-chain polymer nanoparticles are collapsed, soft nano-objects of ultra-small size (typical diameter size < 20nm) synthesized from an individual polymer chain (usually named precursor) through intrachain cross-linking techniques under appropriate dilute conditions^[12-18] (Figure 1.2).



Figure 1.2. Schematic figure of single-chain polymer nanoparticle formation by intramolecular collapse of a polymer precursors.

The dimensions of the resulting nanoparticles depend mainly on the molecular weight of the polymer precursor, the number of intramolecular bonds generated in the intrachain collapsing process, as well as the own chemical nature of the polymer backbone and the quality of the solvent in which the intrachain cross-linking process takes place.

SCNPs have recently gained prominence in nanoscience due to their exceptional and sometimes unique properties. For example, polymeric SCNPs have been evaluated as rheology agents.^[19] Functional polystyrene nanoparticles were mixed with neat natural rubber (*cis*-1,4-polyisoprene) and it was observed that the viscosity of the natural rubber decreases significantly as a consequence of the presence of the ultra small nanoparticles. SCNPs have also been used as catalyst. For instance, water soluble polymethyl methacrylate nanoparticles containing L-proline catalytic units were able to catalyze the aldol reaction between *p*-nitrobenzaldehyde and cyclohexanone.^[20] In another case, nanoparticles contained Ru as catalyst and they showed transfer hydrogenation in water^[21] (Figure 1.3a). Another application could be as image contrast agents. For this purpose, polyacrylic nanoparticles containing multiple Gd^{III} centres were synthesized in order to obtain magnetic resonance imaging (MRI) agents with enhanced relaxivity^[22] (Figure 1.3b). Another application is as gene delivery. It was found that SCNPs that worked as gene vectors interacted differently with plasmid DNA compared with conventional vectors and when tested in different type of cells, they showed superior transfection profile.^[23] Apart from these examples, SCNPs have many different applications, such as, sensors,^[24] smart gels^[25] and peptide delivery^[26] (Figure 1.3c) among others.

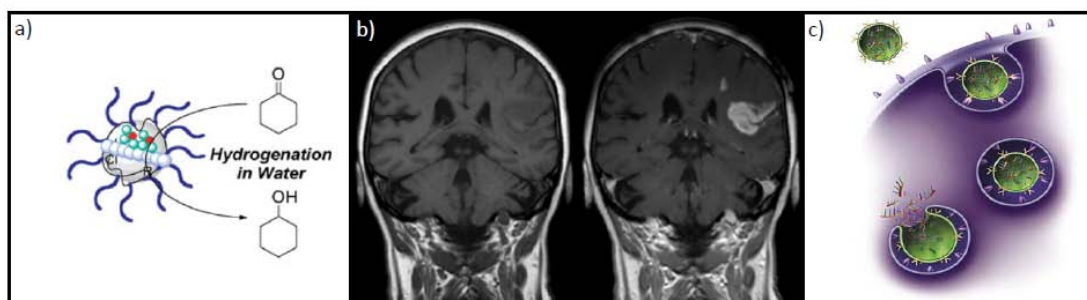


Figure 1.3. Some applications of SCNPs: a) Nanoparticles that acts as catalyst showing transfer hydrogenation in water. b) Nanoparticles for image contrast agent. c) Nanoparticles for peptide delivery.

The process of intrachain cross-linking used to synthesize the SCNPs has emerged as a reliable and efficient alternative, which offers good control over the properties of the resulting nanoparticles while remaining a simple procedure. This is possible because, in principle, the dimensions of the nanoparticles can be tuned by controlling the molecular weight of the precursor, and the quantity of intramolecular bonds generated in the collapse. Additionally, the functionalities integrated in the polymer precursor will ultimately determine those of the nanoparticles. All these features allow engineering efficient processes, although there are still several aspects of the process that have to be understood in order to harness its potential.

1.2. Goals and methodology

The general aim of this work was to explore several aspects of the process of synthesis of SCNPs through intrachain cross-linking reaction. Several synthesis paths were studied in order to gain a deeper insight and understanding that could allow for future researchers and engineers to develop specific applications based on these systems.

This work takes advantage of the fact that there are several powerful characterization techniques, which allow extracting information from the nanoscale in order to obtain a detailed description of the structures.

Computer-assisted simulation techniques, which allow replicating the world at the nanoscale, were extensively employed. They were very helpful for analyzing the information obtained in the experiments and understanding the behavior of the NPs at the microscale.

The specific issues analyzed in this Thesis are the following:

1.2.1. Scaling laws of SCNPs

Scaling laws are sets of equations that establish the relationship between the properties of a NP and those of the precursor from which is synthesized. They play a relevant role during the engineering of the synthesis process of a NP with defined properties.

This study was focused on critically reviewing and validating the scaling laws for dynamic properties, which define the behavior of NPs in solution.

Part of the work consisted in retrieving and analyzing a large collection of data obtained from the bibliography. These data were used for testing thoroughly as possible the reliability of the scaling laws.

1.2.2. Mimicking enzyme behavior with SCNPs

The efficiency of enzymes for performing their fundamental tasks in biological systems is a continuous source of inspiration for researchers in the field of nanoparticles. In the case of SCNPs, the controlled collapse process is a rough mimic of protein folding, and this image drives its optimization.

The effort was focused in trying to imitate the catalytic capabilities of some enzymes by developing a process that enables such feature in SCNPs, and evaluating the results at two levels: characterizing the properties of the resulting NPs and determining their efficiency in specific catalytic reactions.

1.2.3. Photoactivated synthesis of SCNPs through thiol-ene and thiol-yne coupling reaction

Thiol-ene (TEC) and thiol-yne (TYC) coupling reactions are emerging as powerful click chemistry tools. However, they have rarely used as cross-linkers for the synthesis of SCNPs. This possibility was explored in this study, paying special attention to the properties of the NPs produced.

Another aspect explored was the possibility of photoactivating the reaction (instead of the usual thermoactivation). This type of activation has some interesting advantages for better control, through selective irradiation of the region where the reaction takes place.

Finally, in order to obtain deeper information about the processes studied, the results were complemented with some simulation work.

1.3. Structure of this Thesis

This chapter provides a general perspective and puts in context the research work that has been developed along this Thesis.

The following chapter is intended for the reader unfamiliar with some of the concepts and techniques that have been employed in this work. This includes details on the synthesis of SCNPs, the different characterization techniques, and the theoretical methods employed. Some summarized information and guidelines for further reading can be found there.

Each one of the goals mentioned in the previous section is independent from each other, and therefore are treated in separated chapters. These chapters are intended for readers familiar with the topics, and therefore focus quickly in providing details about methodology used for the synthesis and characterization, the presentation of the results and the critical discussion.

1.4. References

1. R. Nagarajan, *ACS Symposium Series* **2008**, 996, 2.
2. J. H. Braun, A. Baidins, R. E. Marganski, *Progress in Organic Coatings*, **1992**, 20, 105.
3. C. Contado, A. Pagnoni, *Anal. Chem.* **2008**, 80, 7594.
4. X. Wang, J. E. Hall, S. Warren, J. Krom, J. M. Magistrelli, M. Rackaitis, G. G. A. Bohm, *Macromolecules* **2007**, 40, 499.
5. K. M. M. A. El-Nour, E. Eftaiha, A. Al-Warthan, R. A. A. Ammar, *Arabian Journal of Chemistry* **2010**, 3, 135.
6. M. Haruta, *The Chemical Record* **2003**, 3, 75.
7. E-J. Park, T. Erdem, V. Ibrahimova, S. Nizamoglu, H. V. Demir, D. Tuncel, *ACS Nano*. **2011**, 5, 2483.
8. F. Chen, P. Liu, *ACS Appl. Mater. Interfaces* **2011**, 3, 2694.
9. J. K. Oh, R. Drumright, D. J. Siegwart, K. Matyjaszewski, *Prog. Polym. Sci.* **2008**, 33, 448.
10. Z. L. Tyrrell, Y. Shen, M. Radosz, *Prog. Polym. Sci.* **2010**, 35, 1128.
11. R. Jelinek, *Cellular and Biomolecular Recognition*, John Wiley & Sons, **2009**.
12. E. Hart, B. Van Horn, V. Y. Lee, D. S. Germack, C. P. Gonzales, R. D. Miller, C. J. Hawker, *J. Amer. Chem. Soc.* **2002**, 124, 8653.
13. A. Ruiz de Luzuriaga, N. Ormategui, H. J. Grande, I. Odriozola, J. A. Pomposo, I. Loinaz, *Macromol. Rapid Commun.* **2008**, 29, 1156.
14. D. Mecerreyes, V. Lee, C. J. Hawker, J. L. Hedrick, A. Wursch, W. Volksen, T. Magbitang, E. Huang, R. D. Miller, *Adv. Mater.* **2001**, 13, 204.
15. J. Jiang, S. Thayumanavan, *Macromolecules*. **2005**, 38, 5886.
16. T. A. Croce, S. K. Hamilton, M. L. Chen, H. Muchalski, E. Harth, *Macromolecules* **2007**, 40, 6028.
17. A. C. Cherian, F. C. Sun, S. S. Sheiko, G. W. Coates, *J. Am. Chem. Soc.* **2007**, 129, 11350.
18. J. B. Beck, K. L. Killops, T. Kang, K. Sivanandan, A. Bayles, M. E. Mackay, K. L. Wooley, C. J. Hawker, *Macromolecules*. **2009**, 42, 5629.
19. L. Oria, R. Aguado, J. A. Pomposo, J. Colmenero, *Adv. Mater.* **2010**, 22, 3038.
20. E. Huerta, P. J. M. Stals, E. W. Meijer, A. R. A. Palmans, *Angew. Chem. Int. Ed.* **2013**, 52, 2906.

21. T. Terashima, T. Mes, T. F. A. De Greef, M. A. J. Gillissen, P. Besenius, A. R. A. Palmans, E. W. Meijer, *J. Am. Chem. Soc.* **2011**, 133, 4742.
22. I. Perez-Baena, I. Loinaz, D. Padro, I. Garcia, H. J. Grande, I. Odriozola, *J. Mater. Chem.* **2010**, 20, 6916.
23. B. Ben Newland , Y. Zheng, Y. Jin, M. Abu-Rub, H. Cao, W. Wang, *J. Am. Chem. Soc.* **2012**, 134, 4782.
24. M. A. J. Gillissen, I. K. Voets, E. W. Meijer, A. R. A. Palmans, *Polym. Chem.* **2012**, 3, 3166.
25. D. E. Whitaker, C. S. Mahon, D. A. Fulton, *Angew. Chem. Int. Ed.* **2013**, 52, 956.
26. G. Njikang, G. Liu, L. Hong, *Langmuir* **2011**, 27, 7176.

Chapter 2. Fundamental aspects

2.1. Synthesis of single-chain polymer nanoparticles (SCNPs)

Single-chain polymer nanoparticles are collapsed, soft nano-objects of ultra-small size (typical diameter size < 20 nm) synthesized from an individual polymer chain through intrachain cross-linking techniques under appropriate dilute conditions.

As illustrated schematically in Figure 2.1, in general, the synthesis of SCNPs is composed of three different steps. The first step is the “precursor synthesis” process. The objective of this step is the synthesis of well-defined polymeric precursors of controlled molar mass and narrow size distribution in order to guarantee as much as possible the uniformity of the resulting unimolecular nanoparticles. The second step is the “polymer functionalization” process, in which the polymer precursor is decorated with appropriate functional groups for the intrachain folding process. Finally, the last step is “the intrachain folding/collapse” process of the polymer precursors. Each step is analyzed in more detail below.

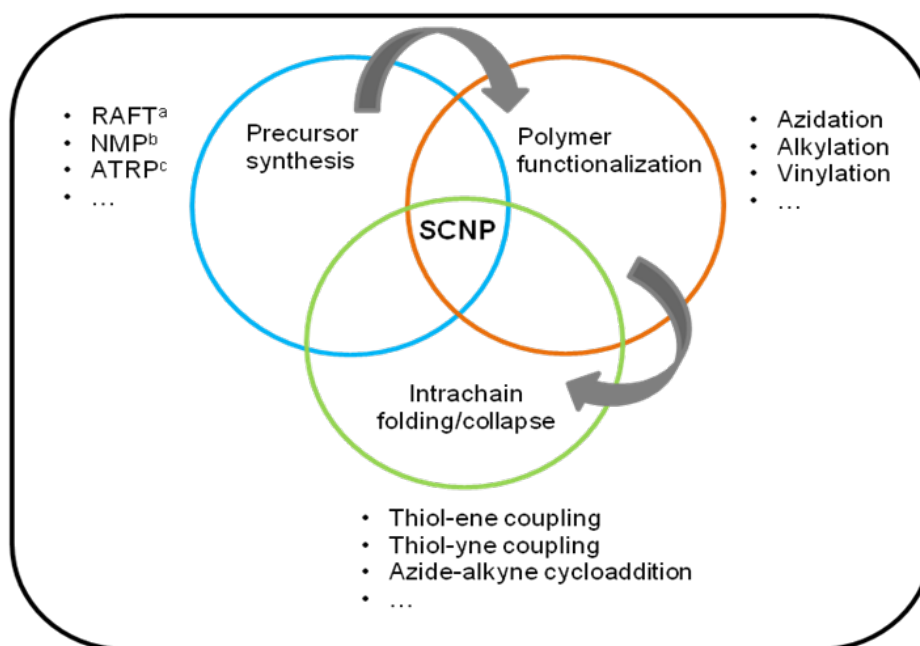


Figure 2.1. Illustration of the different steps involved in the construction of single-chain polymer nanoparticles (SCNPs). a) Reversible addition fragmentation chain transfer polymerization. b) Nitroxide mediated radical polymerization. c) Atom transfer radical polymerization.

2.1.1. Precursor synthesis

For obtaining nanoparticles of the same size, the length of the polymer precursors has to be as similar as possible, but it is not always easy to control the polymerization, especially when high molecular weights are desired or when working with some

specific monomers. The polymers used in this work for the synthesis of single-chain nanoparticles were synthesized using different polymerization techniques depending on the desired molecular weight. To obtain high molecular weight polymer precursors, free radical polymerization was used. This polymerization technique is not a controlled polymerization and therefore there is no control over the polydispersity index, but it allows obtaining really high molecular weight polymer precursors. For obtaining low or moderate molecular weight polymers, RAFT polymerization technique was used, which is one of the most important process within controlled radical polymerization (CRP) techniques. Using RAFT polymerization, the control over the polydispersity is really good, obtaining low values of polydispersity and low to moderate molecular weight polymers. Inside the RAFT polymerization, redox initiated RAFT polymerization was used for polymerizing monomers that are unstable with the temperature. The polymerization techniques employed in this thesis are explained in detail in the next sections.

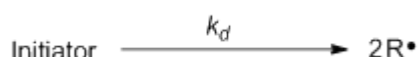
A. Free radical polymerization (FRP)

Free radical polymerization is a chain polymerization technique and it is widely used for polymerizing vinyl monomers. The mechanism of FRP is well understood and extension of the concepts to new monomers is generally straightforward. Another advantage is that the conditions for the polymerization are relatively easy, rigorous removal of moisture is generally unnecessary while polymerization can be carried out in bulk, in solution and also in dispersed media (suspension, emulsion, microemulsion...).[1]

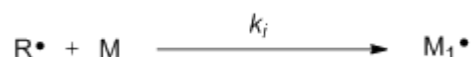
Like any chain reaction, free radical polymerization is composed of four elementary reactions:

Initiation

The initiation step is considered to involve two reactions. The first reaction is the dissociation of an initiator, forming a pair of radicals. k_d is the rate constant for the catalyst dissociation.

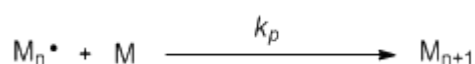


The second part of the initiation involves the addition of this radical to the first monomer to produce the chain-initiating radical M_1^\bullet . M represents a monomer and k_i is the rate constant for the initiation step.



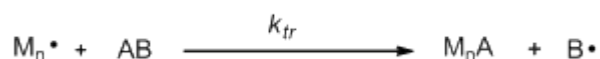
Propagation

This step consists of the growth of M_1^{\bullet} by the successive additions of large amount of monomer. k_p is the rate of constant for propagation.



Transfer

Transfer occurs when an active site is transferred to an independent molecule such as monomer, initiator or solvent. This process results in both a terminated molecule (step four) and a new active site that is able to undergo propagation. k_{tr} is the rate constant for transfer.



Termination

The active sites are eliminated. Usually, the termination occurs by two ways: combination and disproportionation.

Combination occurs when two propagating radical chains of arbitrary degrees of polymerization of n and m join to form a single terminated chain of degree of polymerization $n+m$. k_{tc} is the rate constant for termination by combination.



Termination can also occur by disproportionation, giving two terminated chains. In this case, a radical chain abstracts a hydrogen atom from another radical chain. Thus, a double bond is formed of the missing hydrogen. k_{td} is the rate constant for termination by disproportionation.



In FRP, the propagation rate is much faster than the termination and initiation rates, and taking into account that transfer is only a secondary reaction, high molecular weight polymer can be obtained from most monomers. Slow initiation can be

accomplished by using radical initiators with appropriately long half lifetimes (e.g., ~10h). Initiators are typically peroxides, diazenes, redox systems and high-energy sources which slowly produce initiating radicals.

In addition, in FRP, the average life of a propagation chain is very short, being the reason of the poor control over the molecular weight and consequently obtaining high values of polydispersity.^[2]

B. Controlled radical polymerization (CRP)

In the late 80s, new strategies of radical polymerizations appeared, known as controlled radical polymerizations (CRPs). These techniques allow the synthesis of polymer precursors of controlled molar mass and narrow size distribution in order to guarantee as much as possible the uniformity of the unimolecular nanoparticles. Currently, the most common CRP technique employed is reversible addition fragmentation chain transfer (RAFT) polymerization, followed by atom transfer radical polymerization (ATRP) and nitroxide mediated radical polymerization (NMP). A common feature for all CRP procedures is the dynamic equilibrium between active propagating radicals and dormant, deactivated species.

Fast exchange among active and dormant species is necessary for good control over molecular weight, polydispersity and chain architecture in all CRP systems. The lifetime of a propagating chain in the active state in a CRP process is comparable to the lifetime of a chain in conventional RP process. However, because the whole propagation process may take approximately one day in CRP, there is opportunity to carry out different synthetic procedures, such as chain-end functionalization and chain extension.^[2]

In this Thesis, among the different CRP techniques, RAFT polymerization was chosen as a polymerization technique for the synthesis of most linear polymer precursors used for the synthesis of single-chain polymer nanoparticles.

C. Reversible addition fragmentation chain transfer (RAFT) polymerization

RAFT polymerization was introduced in 1998 by the group of Rizzardo.^[3] It is one of the most successful controlled radical polymerization processes due to its applicability for a wide range of monomers, including (meth)acrylates, (meth)acrylamides, acrylonitrile, styrenes, dienes, and vinyl monomers. Also, this polymerization technique shows wide tolerance of reaction conditions as the conventional process. Another important advantage is that it is a “metal-free” technique when compared with other CRP

techniques such as ATRP, which is an important advantage especially for biomedical applications.

In RAFT polymerization, the deactivation/activation equilibria are based on chain-transfer reactions, which are carried out using RAFT agents, also known as chain transfer agents (CTAs). These RAFT agents are thiocarbonylthio compounds that have a free radical leaving group R and a group Z (Figure 2.2).

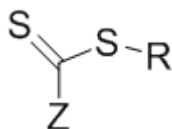


Figure 2.2. A general structure of a RAFT agent is based on a thiocarbonylthio compound bonded to a group Z and a free radical leaving group R.

The choice of the RAFT agent is an important factor to provide appropriate control over the polymerization. There is a broad variety of thiocarbonylthio RAFT agents, such as dithiobenzoates, trithiocarbonates, xanthates, dithiocarbamates...(Figure 2.3). The effectiveness of the RAFT agent depends on the monomer that is going to be polymerized and also depends on the free radical leaving group R and the group Z which activates or deactivates the thiocarbonyl double bond and modify the stability of the intermediate radicals.

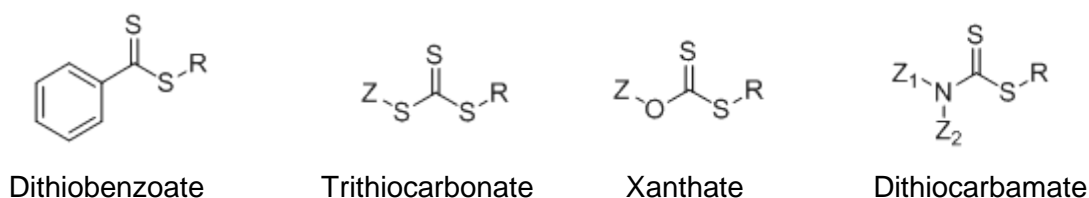


Figure 2.3. Chemical structure of some transfer RAFT agents used in RAFT polymerization.

This polymerization technique is performed by adding a chosen amount of RAFT agent to a conventional free radical polymerization system, using the same monomers, initiators, solvents, temperatures... as in FRP. In this way, it provides similar versatility and advantages to conventional FRP but obtaining polymers with narrow polydispersity and controlled molecular weights.

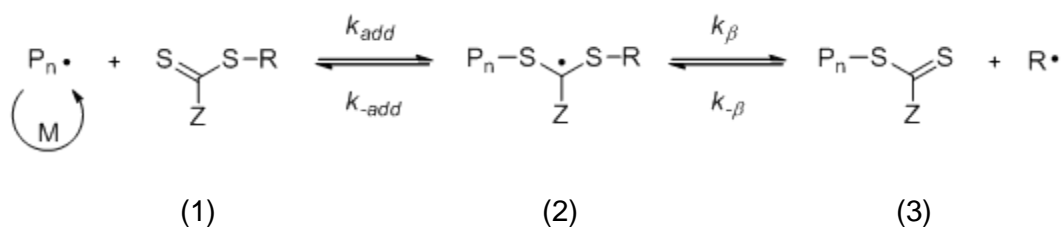
The general mechanism of RAFT polymerization is the following:^[4]

Initiation

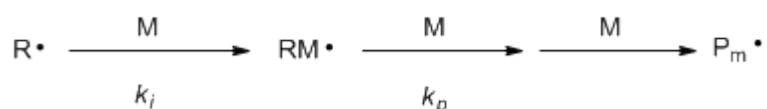
Upon the decomposition of the initiator (I), the radical reacts with a monomer unit to create a radical specie which starts an active polymerizing chain.

Reversible chain transfer

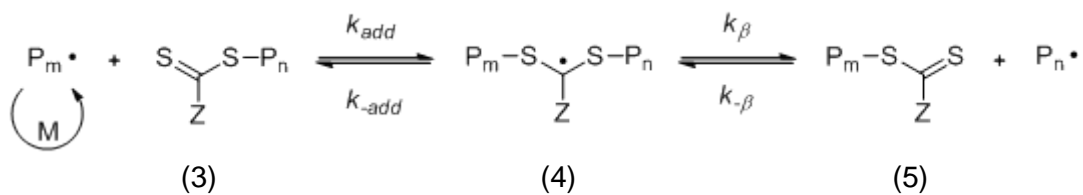
In the early stages of the polymerization, the propagating radical ($\text{P}_n\cdot$) reacts with the CTA (1) and the R leaving group becomes a new radical ($\text{R}\cdot$) while the polymeric thiocarbonylthio compound (3) stays in a deactivated state.

Reinitiation and propagation

The reaction of the radical ($\text{R}\cdot$) with monomers forms a new propagating radical ($\text{P}_m\cdot$), which participates in the chain equilibrium steps.

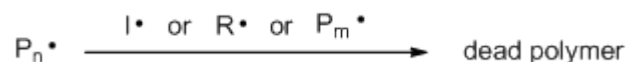
Chain equilibration

It is the fundamental step in which a rapid equilibrium between propagating radicals ($\text{P}_n\cdot$ and $\text{P}_m\cdot$) and the dormant polymeric thiocarbonylthio compounds (3 and 5) provides equal probability for all chains to grow.



Termination

This side reaction involves the coupling between two active polymer chains to give a dead polymer chain.



In order to obtain an efficient control over the molecular weight distribution, several conditions are necessary.^[5] First, it is necessary that the chains be initiated within a short period of time in order to grow simultaneously. Second, the number of monomers that are added to the propagation radical during each cycle of activation/deactivation must be low in order to guarantee similar growth rate for all the chains. Finally, it is necessary to minimize any reaction that leads to the formation of dead chains. Relating to the last one, the concentration of radical species should be as low as possible (high $[CTA]_0/[initiator]_0$ ratio) to reduce the probability of termination reactions, while maintaining a satisfactory polymerization rate. As a consequence, most of the radicals will be formed from the thiocarbonylthio $[S=C(Z)S-]$ group and just a small number of polymer chains will be formed from radical initiator and therefore “dead”.

Thus, the maximum number of dead chains will be equal to the number of initiating radicals derived from the initiator used in the polymerization.^[6] The total number of chains will be equal to the number of chains initiated by the radical R^{\bullet} expelled from the dithio compound plus the number of chains generated from the initiator (Figure 2.4). As a result, in order to obtain low polydispersity values, high ratio of CTA to initiator gives better results, nevertheless, at the expense of the molecular weight of the final polymer. Consequently, RAFT polymerization can be used to synthesize narrow polydispersity polymers of moderate molecular weight at rates of polymerization slower than in FRP. Furthermore, when the polymerization is complete or stopped, most of the polymer chains are in the dormant form, i.e., they retain the thiocarbonylthio end group that can be reactivated. Reactivation of these chains in the presence of a second monomer will give rise to A-B diblock copolymers, again with relatively low polydispersity values.

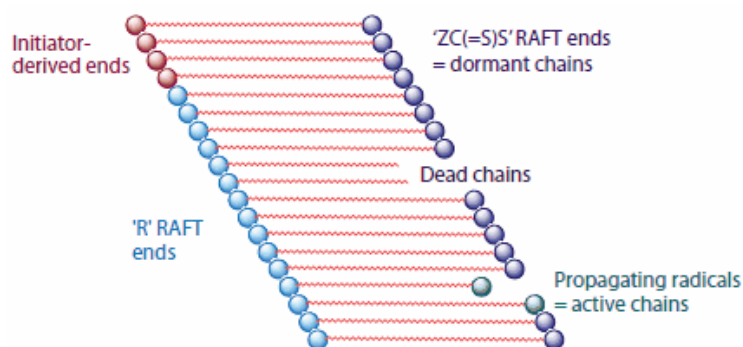


Figure 2.4. Schematic representation of RAFT polymerization.

D. Redox initiated RAFT polymerization

Many oxidation-reduction reactions produce radicals that can be used to initiate polymerization. Recently, it was found that RAFT polymerizations of vinyl monomers proceed very well at room temperature with a traditional redox system, using benzoyl peroxide (BPO) and *N,N*-dimethylaniline (DMA) redox pair as initiator (Figure 2.5). Redox initiation has many advantages such as low activation energy (10-20 kcal/mol) compared to the thermal activation (30 kcal/mol). This enables the polymerization to be carried out at room or even lower temperature, thereby decreasing the possibility of side reactions which may change the reaction kinetics and the properties of the resulting polymer.^[7]

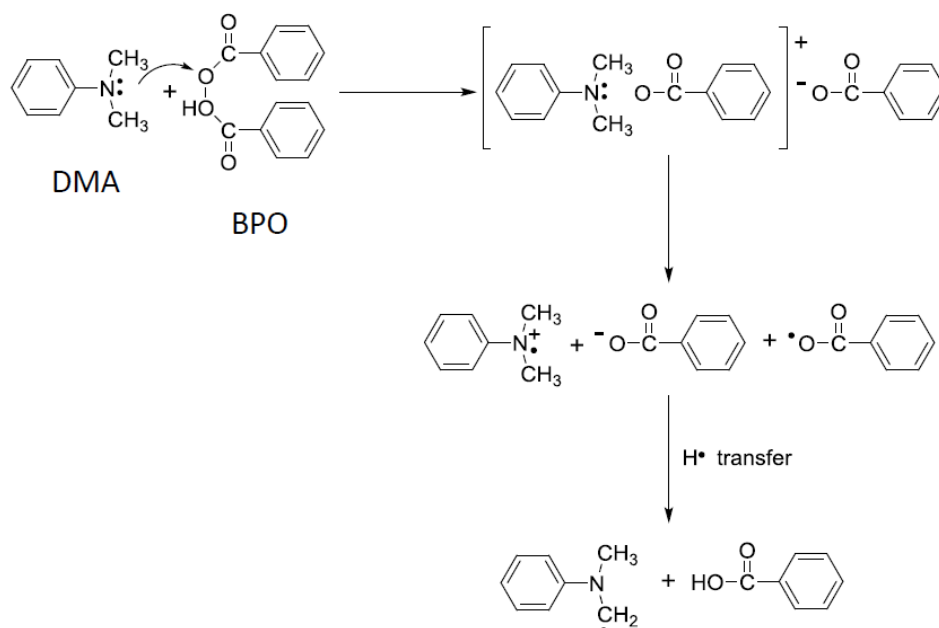


Figure 2.5. Mechanism of radical formation for BPO/DMA redox system.

2.1.2. Polymer functionalization

Polymer functionalization is based on the quantitative and selective modification of a given polymer using relatively mild conditions without any side reactions. Polymer functionalization is also known as post-polymerization modification or polymer analogous modification and it has a long history in polymer science.^[8] For natural polymers, the first report of sulfur-modified natural rubber was made independently about 1840 by Hancock, Ludersdorf and Goodyear.^[9] Concerning synthetic polymers, the functionalization of butadiene polymers via thiol-ene addition was reported by Serniuk et al. in 1948.^[10]

In some cases, the monomers contain the appropriate functional group for the collapse process. In other cases, on the contrary, the monomers do not contain the desired functional groups and after the polymerization, the functionalization step is necessary. The most efficient and used polymer functionalization reactions are:^[8] (1) thiol-ene/thiol-yne additions, (2) modifications of epoxides, anhydrides, oxazolines and isocyanates by reaction with amines/alcohols/thiols, (3) modification of active esters by reaction with amines, (4) thiol-disulfide exchange, (5) Diels-Alder reaction, (6) Michael-type addition, (7) Copper-catalyzed azide alkyne cycloaddition (CuAAC) and (8) Modification of ketones and aldehydes with amines / alkoxyamines / hydrazines. A summary of the different groups needed for the preparation of functionalized polymers via the above functionalization reactions is shown in Table 2.1.

Table 2.1. Highly efficient reactions for the preparation of functionalized polymers.

Polymer functionalization technique	Functional groups involved	Functionalizable polymers
Thiol-ene / thiol-yne additions ^[11]	Thiol / alkene, alkyne	Polymers bearing alkene-, alkyne- or thiol- groups
Modification of epoxides, anhydrides, oxazolines and isocyanates by reactions with amines / alcohols / thiols ^[12,13]	Epoxy, anhydride, oxazoline, isocyanate / amine, alcohol, thiol	Polymers containing epoxide-, anhydride-, oxazoline-, isocyanate-, amine-, alcohol- or thiol- groups
Modification of active esters by reaction with amines ^[14]	N-Hydroxysuccinimide, pentafluorophenyl ester / amine	Polymers bearing N-hydroxysuccinimide-, pentafluorophenyl ester- or amine- groups
Thiol-disulfide exchange ^[15,16]	Pyridyl disulfide / thiol	Polymers containing pyridyl disulfide- or thiol- groups
Diels-Alder reaction ^[17,18]	Diene / alkene	Diene- or alkene- bearing polymers
Michael-type addition ^[19,20]	Acrylate, N-substituted-maleimide, vinyl sulfone / thiols	Polymers bearing acrylate-, N-substituted-maleimide-, vinyl sulfone- or thiol- groups.
Copper-catalyzed azide alkyne cycloaddition ^[21,22,23]	Azide / alkyne	Azide- or alkyne- bearing polymers
Modification of ketones and aldehydes with amines / alkoxyamines / hydrazines ^[24]	Ketone, aldehyde / amine, alkoxyamine, hydrazine	Polymers containing ketone-, aldehyde-, amine-, alkoxyamine-, or hydrazine- groups

2.1.3. Intrachain folding/collapse techniques for the synthesis of SCNPs

The intramolecular collapse of the linear polymer precursors occurs through the cross-linking of the reactive functional groups. As mentioned in section 2.1.2, the functional groups can be introduced directly in the polymer, this occurs when the monomers contain the desired functional groups that are necessary for the cross-linking process. In other cases, the monomers do not contain the appropriate functional groups and the polymer has to be functionalized. Once the linear polymer precursors have the correct functional groups, the intramolecular chain collapse can be carried out using different strategies:

A. Intrachain homocoupling

The polymer chain is functionalized with reactive self-complementary “R” groups (e.g., double bonds) which are then reacted intramolecularly (Figure 2.6).

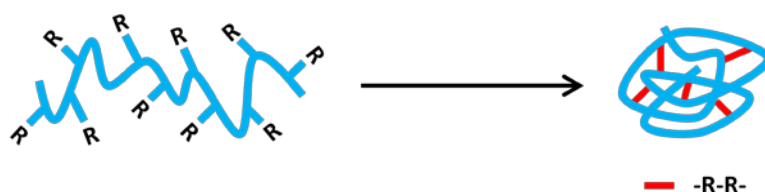


Figure 2.6. Schematic representation of intrachain homocoupling process.

B. Intrachain heterocoupling

It is very similar to the previous one, but instead of using one functional group, it requires two complementary functionalities (“R” and “X”) simultaneously on the same polymer chain. The complexity of the synthesis of the precursor copolymers is one of the major drawbacks of this approach. It is often difficult to incorporate two complementary reactive groups randomly along the precursor chain (Figure 2.7).

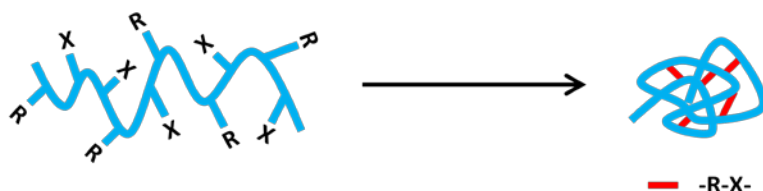


Figure 2.7. Schematic representation of intrachain heterocoupling process.

C. Cross-linker induced collapse

In this strategy, a multifunctional cross-linker is used in order to synthesize the unimolecular nanoparticles. The polymer chain is functionalized with suitable "R" functional groups and is collapsed by reacting with the "X" end-groups of the cross-linker. The difficulty of incorporating two complementary functional groups in the polymer chain by using the intrachain heterocoupling can be solved by using this technique (Figure 2.8).

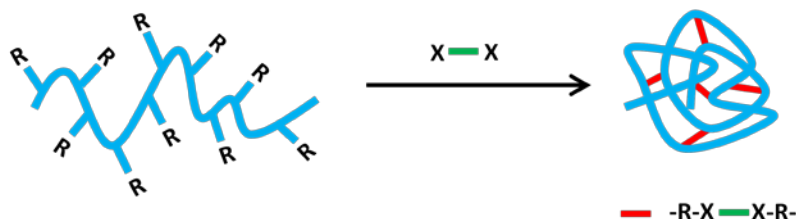


Figure 2.8. Schematic representation of intrachain cross-linker induced process.

In this work, three different synthesis routes were employed for obtaining SCNPs. The first route is based on the intrachain homocoupling strategy, where the collapse process is carried out through glycidyl groups (Figure 2.9).

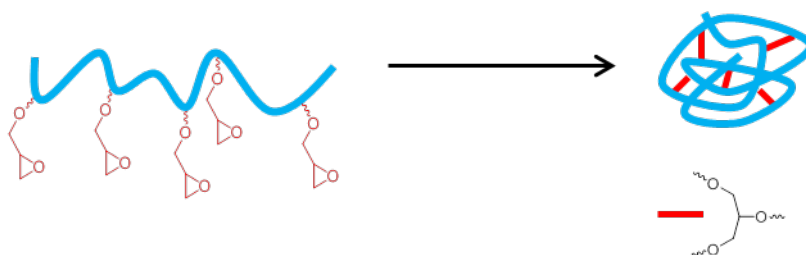


Figure 2.9. Schematic representation of intrachain homocoupling collapse through the reactions of glycidyl groups.

The other two routes are based on the cross-linker induced collapse. In the first case, the polymer is functionalized with double bonds and it is collapsed through the reaction with the thiol groups of the cross-linker (Figure 2.10).

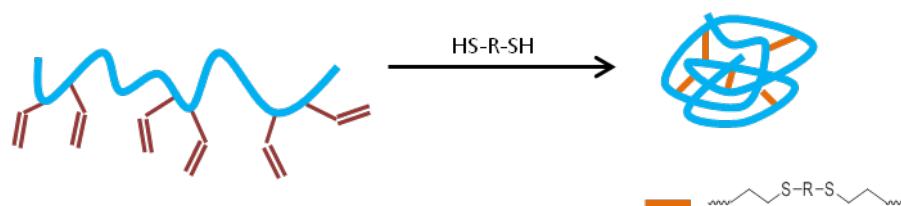


Figure 2.10. Schematic representation of cross-linker induced collapse through the reaction between double bonds of the polymer and thiol groups of the cross-linker.

In the other case, the collapse process occurred through the reaction between triple bonds of the polymer and thiol groups of the cross-linker (Figure 2.11).

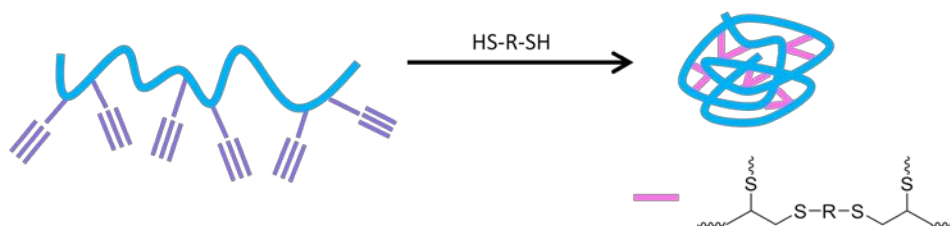


Figure 2.11. Schematic representation of cross-linker induced collapse through the reaction between triple bonds of the polymer and thiol groups of the cross-linker.

Depending on the chemical nature of the cross-linking, SCNPs can be classified in reversible (covalent bonds) and irreversible (non-covalent bonds). Irreversible nanoparticles are appropriate for applications in which excellent thermal and dimensional stability are necessary, such as processing additives or blend compatibilizers. In the other hand, reversible SCNPs could be useful in nanomedicine, for smart delivery of different bioactive cargos or enzyme-mimics applications, due to the potential responsiveness towards different assembly/disassembly stimuli like pH, temperature, salt concentration... Table 2.2 shows a summary of different covalent bonding interactions used for the synthesis of permanent SCNPs. On the contrary, Table 2.3 shows a summary of different non-covalent (NC) and dynamic-covalent (DC) bonding interactions used for the synthesis of reversible SCNPs.

Tabla 2.2. Covalent bonding interactions employed during SCNP construction for permanent polymer folding/collapse.

Reactive functional groups	Irreversible intrachain reactions
Vinyl ^[25,26,27]	Radical coupling and
Benzocyclobutene ^[28,29]	Diels-Alder
Benzosulfone ^[30,31]	Diels-Alder
Azide + alkyne ^[21,22,23,32]	Cooper-catalyzed [3+2] cycloaddition
Carboxylic acid + diamine ^[33]	Amide formation
Isocyanate + diamine ^[13]	Urea formation
Eneidyne ^[34,35,36,37]	Bergman and photo-Bergman cyclization
Sulfonyl azide ^[38]	Nitrene-mediated cross-linking
Benzoxazine ^[39]	Ring opening polymerization
Alkyne ^[40]	Glaser-Hay coupling

Table 2.3. Non-covalent (NC) and dynamic-covalent (DC) bonding interactions in SCNPs construction.

Reactive functional groups	Reversible intrachain reactions
Benzamide ^[41]	Benzamide hydrogen bonding
2-Ureido-pyrimidone (UPy) ^[42]	UPy dimerization
Coumarin ^[43]	Coumarin photo-dimerization
Benzaldehyde ^[44]	Acylhydrazone formation
β -Ketoester ^[45]	Enamine formation
Methyl viologen + Naphtyl ^[46]	Cucurbit[<i>n</i>]uril complexation
L-Phenylalanine (Phe) ^[47]	Hydrophobic Phe-Phe interactions
Aminophenyl disulfide ^[48]	Disulfide formation

2.2. Characterization techniques of polymer precursors and SCNPs

Characterization techniques have played a fundamental role in the development of this thesis. A large set of techniques has allowed extracting information concerning properties at the nano-scale. This information has been used to understand and relate the final characteristics of the SCNPs with respect to specific configurations of the synthesis processes and characteristics of the precursors. These techniques can be classified depending on the information provided:

A. Molecular weight and polydispersity index

Size exclusion chromatography / gel permeation chromatography (SEC/GPC) was used to determine the molecular weight and polydispersity index of polymer precursors and the corresponding SCNPs and to follow the evolution of the intrachain collapse process.

B. Dimensional characterization techniques

The techniques used were: transmission electron microscopy (TEM), atomic force microscopy (AFM), dynamic light scattering (DLS), small angle neutron scattering (SANS) and small angle X-ray scattering (SAXS). TEM and AFM were used for obtain

information about the size of the nanoparticle in the dry state and DLS was used to determine the size of SCNPs in solution.

SANS and SAXS techniques were employed to compare the size and the shape of polymer precursors and the corresponding SCNPs in solution.

C. Structural characterization techniques

Proton nuclear magnetic resonance (^1H NMR), fluorine nuclear magnetic resonance (^{19}F NMR), infrared spectroscopy (IR), X-ray photoelectron spectroscopy (XPS) and elemental analysis (EA) were used. ^1H NMR and ES provided quantitative information about the structural composition of polymer precursors and they were also used to calculate the degree of cross-linking of SCNPs. IR measurements were performed in order to corroborate the presence of some specific functional groups. ^{19}F NMR and XPS were used to analyze a specific atom of SCNPs.

D. Thermal characterization techniques

These techniques include differential scanning calorimetry (DSC) and thermogravimetric analysis (TGA). DSC was used to provide information about the main thermal transitions (e.g., glass transition and melting transition) and to compare the results of polymers precursors and the corresponding SCNPs. TGA gave the comparison of the decomposition temperature between polymer precursors and SCNPs.

In the following pages, a brief description of the main techniques is provided.

2.2.1. Size Exclusion Chromatography (SEC)

SEC is a chromatographic method in which molecules in solution are separated by their size, not by molecular weight. Separation is achieved by the differential exclusion from the pores of the packing material, of the sample molecules as they pass through a bed of porous particles. When dissolved molecules of various sizes flow into the column, smaller dissolved molecules flow more slowly through the column because they penetrate deep into the pores, whereas large dissolved molecules flow quickly through the column because they do not enter the pores, consequently, larger molecules elute faster from the column than smaller molecules.

SEC was used to obtain the molecular weight and polydispersity index of polymer precursors and SCNPs, and to follow the evolution of nanoparticle formation. Measurements were performed at 30 °C on an Agilent 1200 system equipped with

PLgel 5 μ m Guard and PLgel 5 μ m MIXED-C columns, a differential refractive index (RI) detector (Optilab Rex, Wyatt) and a multi-angle laser light scattering (MALS) detector (Minidawn Treos, Wyatt). Data analysis was performed with ASTRA Software from Wyatt. THF was used as eluent at a flow rate of 1 mL/min. dn/dc values in THF were determined using the Optilab Rex detector.

2.2.2. Nuclear Magnetic Resonance (NMR) Spectroscopy

Nuclear magnetic resonance spectroscopy is a powerful, nondestructive technique that determines the structural and conformational analysis of complex molecules, quantitative analysis of complex mixtures and reaction rates of chemical systems.

This spectroscopic technique can be used only to study atomic nuclei with an odd number of protons or neutrons (or both). This situation occurs in atoms of ^1H , ^{13}C , ^{19}F and ^{31}P . These types of nuclei are magnetically active, that means that they possess spin, like electrons, since the nuclei have positive charge and have a rotational movement about an axis that makes them behave like tiny magnetic dipoles. In the absence of magnetic field, the nuclear spins are oriented randomly. However, when a sample is placed in a magnetic field, the nuclei with positive spin are oriented in the same direction of the field (spin α), while the nuclei with negative spin are oriented in opposite direction to the magnetic field (spin β). When the nuclei return to their initial state emit signals whose frequency depends on the energy difference between the spin states α and β . The NMR spectrometer detects these signals and records them as a graph of frequency versus intensity, which is called the NMR spectrum.

^1H NMR was used to calculate the composition of the polymers and to obtain the cross-linking degree of SCNPs. ^{19}F NMR was used to analyze the fluorine atom in the nanoparticles. ^1H and ^{19}F Nuclear Magnetic Resonance (NMR) spectra were recorded at room temperature on Bruker spectrometers operating at 300 and 500 MHz for ^1H NMR and 400 MHz for ^{19}F NMR, using CDCl_3 as solvent in all the cases.

2.2.3. Dynamic Light Scattering (DLS)

This technique is one of the most popular methods used to determine the size of particles. In DLS the sample is illuminated by a laser beam and the fluctuations of the scattered light are detected at a known scattering angle θ by a fast photon detector (Figure 2.12). From a microscopic point of view the particles scatter the light and thereby imprint information about their motion. Analysis of the fluctuation of the scattered light thus yields information about the particles.

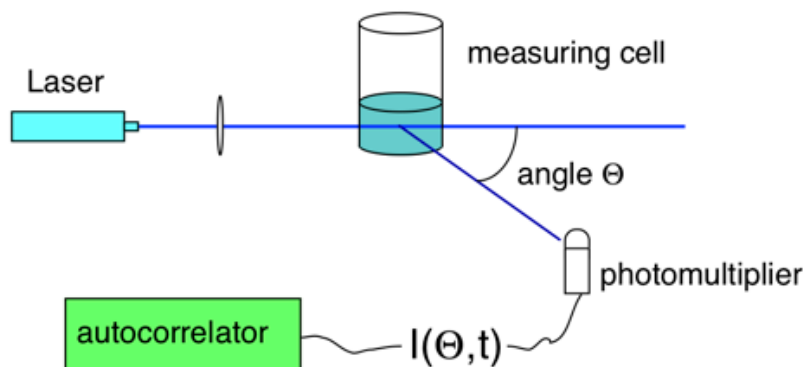


Figure 2.12. Schematic explanation of the operation of DLS.

Malvern Zetasizer Nano ZS apparatus was used to determine the hydrodynamic radius at room temperature in CHCl_3 solvent. The “size distribution by number” plot was employed in this work. All measurements were determined at 173° to the incident beam. DLS was used to compare the hydrodynamic size of polymer precursors and SCNPs.

2.2.4. Fourier Transform Infrared Spectroscopy (FTIR)

FTIR is a very important technique to qualitatively identify organic materials and to determine the molecular structure. This technique is based on the absorption of the electromagnetic radiation by the molecules at specific frequencies (resonant frequencies) that are characteristic of their structure. Thus, the frequency of the vibrations can be associated with a particular bond type.

FTIR was employed as a complementary technique to ^1H NMR, analyzing the disappearance of specific bonds after the intrachain collapse process. FTIR spectroscopy spectra were recorded at room temperature on a JASCO 3600 FTIR spectrometer.

2.2.5. Thermal Gravimetric Analysis (TGA)

TGA is an analytical technique used to determine a material's thermal stability and its fraction of volatile components by monitoring the weight change that occurs as sample is heated. The measurement is normally carried out in air or in an inert atmosphere, and the weight is recorded as a function of temperature (or time).

The measurements were performed in a Q500-TA Instruments apparatus at a heating rate of 10 °C/min under nitrogen atmosphere. The decomposition temperature was determined as the temperature at which 50% of the total weight loss takes place.

2.2.6. Differential Scanning Calorimetry (DSC)

DSC monitors heat effects associated with phase transitions and chemical reactions as a function of temperature. In a DSC the difference in heat flow to the sample and a reference at the same temperature, is recorded as a function of temperature. The reference is an inert material such as alumina, or just an empty aluminum pan. The temperature of both the sample and reference are increased at a constant rate.

Through this technique, the glass transition temperatures of the polymer precursors and SCNPs were obtained. Measurements were carried out in a differential scanning calorimeter (DSC-Q2000) from TA-Instruments. All measurements were performed under nitrogen atmosphere and the samples were placed in aluminum pans at a heating rate of 10 K/min from 173 K to 473 K.

2.2.7. Atomic Force Microscopy (AFM)

AFM is a technique to obtain images of the surface of the sample and other information (height, friction, magnetism...) from a wide variety of samples, at really high resolution, covering from a few nanometers to micra. AFM works by scanning a very sharp probe along the sample surface (Figure 2.13). Depending on the nature of the tip motion, AFM can measure in three different modes, contact mode, tapping mode and non-contact mode.

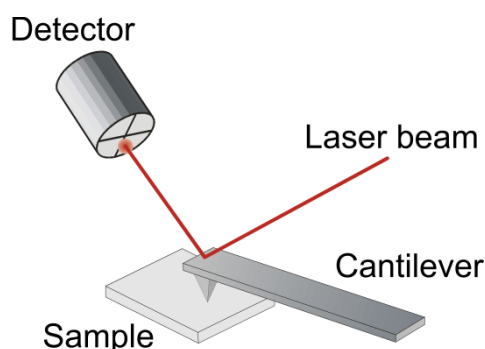


Figure 2.13. Working principle of an Atomic Force Microscope.

The AFM was used to measure the size of SCNPs in the dry state. In this case, the measurements were done in the tapping mode in a MultiMode V-Veeco atomic force microscope after depositing nanoparticles onto gold substrates from highly diluted

solution in CHCl_3 and removing the solvent at room temperature. Conventional AFM tips with a radius of ca. 20 nm were used.

2.2.8. Transmission Electron Microscopy (TEM)

Transmission electron microscopy produces a high-resolution, black and white image from the interactions that take place between samples and energetic electrons in a vacuum chamber, providing information about the structure, shape and size of the sample. It is a technique where an electron beam is transmitted through an ultra-thin sample, interacting with the sample as it passes through. Depending on the density of the material present, some of the electrons are scattered and disappear from the beam. At the bottom of the microscope the unscattered electrons hit a fluorescent screen, which gives rise to a “shadow image” of the specimen with its different parts displayed in varied darkness according to their density.

This technique was used to obtain information about the size of the nanoparticles in the dry state. Measurements were performed using a high-resolution transmission electron microscope TECNAI G220 TWIN. Nanoparticles were deposited onto a carbon-coated TEM support grid from a highly diluted solution in CHCl_3 (0.025 mg/mL) and the solvent was evaporated at room temperature. The measurements were carried out using an accelerating voltage of 200 kV, under low dose conditions.

2.2.9. X-Ray Photoelectron Spectroscopy (XPS)

In XPS, the sample is irradiated with mono-energetic x-rays causing photoelectrons to be emitted from the sample surface. An electron energy analyzer determines the binding energy of the photoelectrons. From the binding energy and intensity of a photoelectron peak, the element identity, chemical state, and quantity of an element are determined.

The SCNPs were analyzed by this technique in order to know the presence of a specific atom, the boron atom. X-ray photoelectron spectroscopy spectra were recorded at room temperature on a SPECS-XPS apparatus. Al $K\alpha$ X-ray line at 1486 eV was used. Powder samples were embedded in carbon tape and the spectra were referenced to the C_{1s} peak.

2.2.10. Small Angle Neutron Scattering (SANS)

SANS is a neutron scattering technique that enables the study of materials on the nanometre to micrometre length scales. The experiment consists of a well-collimated

beam of neutrons being passed through a sample and detectors to count the number of neutrons scattered as a function of angle and neutron wavelength. This data can then be used to extract information about the shape, size, arrangement, and interactions of the components of the sample.

SANS measurements were performed in order to analyze the size and the morphology of polymer precursors and the corresponding SCNPs. The measurements were carried out at the SANS-II instrument at the Swiss spallation neutron source SINQ, Paul Scherrer Institute, Villigen, Switzerland. By using two incoming wavelengths ($\lambda=10.5$ and 5.27 \AA) and three different sample-detector distances (6, 4 and 1.2 m) a momentum transfer range from $Q= 0.0035 \text{ \AA}^{-1}$ to $Q= 0.25 \text{ \AA}^{-1}$ was covered. Solutions of the nanoparticles at $25 \text{ }^\circ\text{C}$ in DMSO-d₆ at a concentration of 8 mg/ml were investigated in quartz cells of 2 mm thickness. The data were corrected for background scattering due to sample cuvettes and detector dark counts; the detector efficiency was calibrated with a H₂O measurement. Measurements were not limited by the huge neutron absorption of Boron; due to the small concentration of this element (0.0086 mg/mL) transmissions of 0.78 for $\lambda = 10.5 \text{ \AA}$ and 0.89 for $\lambda = 5.27 \text{ \AA}$ were determined.

2.2.11. Small Angle X-Ray Scattering (SAXS)

SAXS is based on the detection of the elastic scattering of X-rays by samples which have inhomogeneities of the electron density in the nm-range, at very low angles. In a SAXS instrument a monochromatic beam of X-Rays is brought to a sample from which some of the X-Rays scatter, while most simply go through the sample without interacting with it. The scattered X-Rays form a scattering pattern which is recorded at a detector (Figure 2.14). The angular range covered contains information about shape, size of the particles, internal structure of disordered and partially ordered systems.

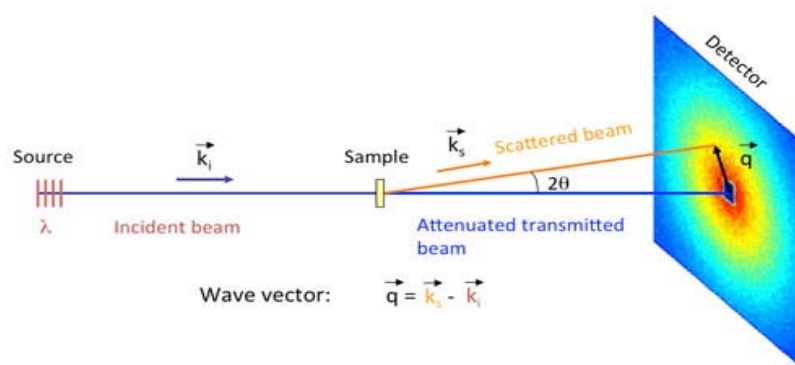


Figure 2.14. Schematic representation of Small Angle X-Ray Scattering.

SAXS measurements were carried out to determine the size and morphology of polymer precursors and the corresponding SCNPs. The experiments were conducted on Rigaku 3-pinhole PSAXS-L equipment operating at 45 kV and 0.88 mA. The MicroMax-002+ X-Ray Generator System is composed by a microfocus sealed tube source module and an integrated X-Ray generator unit which produces $\text{CuK}\alpha$ transition photons of wavelength $\lambda = 1.54 \text{ \AA}$. The flight path and the sample chamber in this equipment are under vacuum. The scattered X-Rays are detected on a two-dimensional multiwire X-Ray Detector (Gabriel design, 2D-200X) and converted to one-dimensional scattering curves by radial averaging. This gas-filled proportional type detector offers a 200 mm diameter active area with *ca.* 200 micron resolution. After radial integration, the scattered intensities were obtained as a function of momentum transfer $Q = 4\pi\lambda^{-1} \sin \theta$, where θ is half the scattering angle. Reciprocal space calibration was done using silver behenate as standard. The sample to detector distance was 2 m, covering a Q-range between 0.01 \AA^{-1} and 0.20 \AA^{-1} . The measurements were performed at room temperature on solutions of SCNPs or precursors in THF at a concentration of 8 mg/mL in capillaries of 2 mm thickness. The data were corrected for background scattering due to capillaries and solvent. Scattering cross-sections were obtained in absolute units by using water as calibration standard.

2.2.12. Elemental Analysis (EA)

Elemental analysis identifies and quantifies elements in a sample. Just as there are many different elements, there are many different experimental methods for determining elemental composition.

Elemental analysis measurements were carried out in order to determine the empirical formula of the polymer precursor and the corresponding SCNP and to calculate the cross-linking degree of the nanoparticles. Measurements were performed in a Euro EA3000 Elemental Analyzer (CHNS).

2.3. Modeling and simulation

Understanding the behavior of complex systems such as the nanoparticles is sometimes difficult through direct analysis of the experimental data and intuition. Fortunately, the advances in computing allow using theoretical models that provide further insight.

The behavior of systems at the nanoscale is strongly governed by the interactions between its constituent particles (electron and nuclei), which ultimately determine the chemical bonding. Therefore, models that were able to describe the systems at microscopic level were necessary. On the other hand, the transformation of a polymer chain into a SCNP is a dynamic process, in which bonds are destroyed and new ones created along a given period. The models should also be capable of accounting for this process.

The other factor to take into account is the computational cost. The number of equations that describe the interactions within a given system grows exponentially with the number of constituent particles. In practice, the simulation of macromolecules containing hundreds of atoms makes the cost of the calculations unbearable when using the most sophisticated and detailed models.

Among the wide variety of modeling techniques that is available nowadays, molecular dynamics was chosen, because of its good compromise between the cost and the level of description.

2.3.1. Molecular dynamics

This technique simulates the evolution in time of a microscopic system, described as a set of charged particles (each particle represents a nuclei and a certain number of electrons). The interaction between particles is defined by a set of potentials V_{ij} , which are functions describing the force acting between particles as a function of the distance between them. The propagation along time is simulated by solving the Newtonian equations of motion:

$$m_i \frac{d^2 \bar{r}_i}{dt^2} = \bar{F}_i$$
$$\bar{F}_i = -\nabla_i \sum_{j=1}^N V_{ij}$$

where m_i is the mass of the particle, \bar{r}_i its position coordinate, and \bar{F}_i the force acting on it. At each iteration of the calculation, the force acting over each particle is calculated, and then used to estimate its acceleration. This information is used to estimate the position of the atoms after a given time step. Then the forces are calculated once more and the process iterated for a certain number of timesteps (this process is illustrated in Figure 2.15).

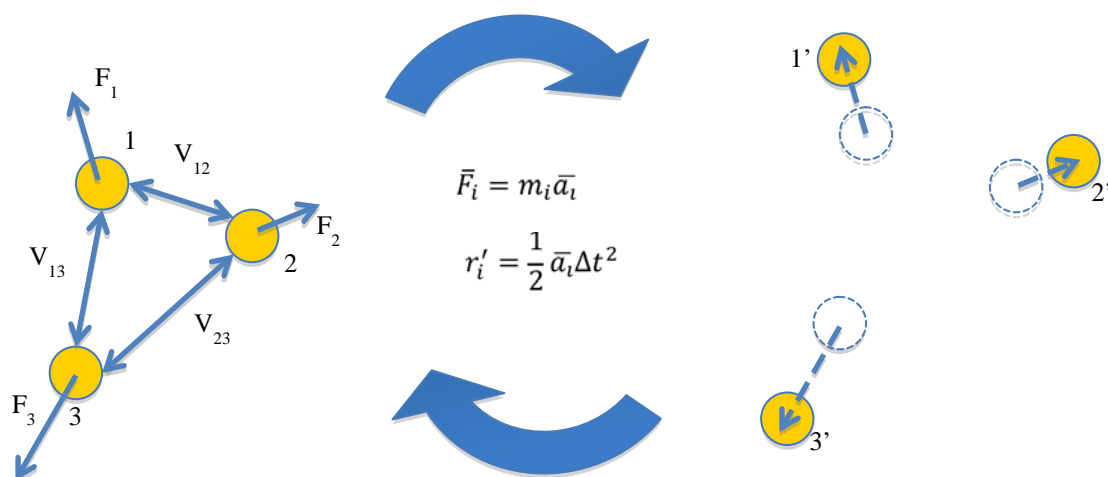


Figure 2.15. Schematic representation of a Molecular Dynamics simulation. The computer calculates the force acting on each atom by adding the potentials V_{ij} . Each potential represents the force between two given particles, as a function of the distance between them. Once Forces are calculated, Newtonian equations are used to estimate the acceleration undergone by each particle, and where the particle will be displaced after a period Δt . Then the calculation is iterated for a number of steps specified as input.

In systems with many particles, the analytical solution of these set of equations cannot be found, and numerical methods are used instead to find approximated solutions. Although it will not be described here, it is worth noting that a careful set up of the parameters controlling the algorithms is necessary in order to ensure quality of the results.

2.3.2. Bead-spring model of isolated polymers

From the brief description of the MD technique provided above, it is obvious that the correct description of the interactions between particles, provided through the potential V_{ij} is critical in determining whether the virtual system will reproduce correctly the behavior of the real system.

The most direct approach would be to describe the polymer as a chain of atoms. This, however, will require having an accurate potential for describing the interaction between each pair of atomic species. On top of this, the amount of atoms contained in a polymer is too large and would make the calculation too expensive to run.

A more effective approach towards modeling of the polymer chains is to group several atoms or monomer units into bigger chain sub-units. The polymer is then described as a chain composed of several of these sub-units (Figure 2.16), in what is typically known as a coarse-grained model. This description reproduces well the essence and nature of the polymer chain, while substantially reducing the computational cost of the

calculation. This allows performing simulations with chains of much larger size, and/or reproducing larger periods of time.

Several coarse-grained models have been proposed along the last decades. In this work a well-understood model was used, known as bead-spring, in which each sub-unit represent one or a few monomer units. The beads along the chain are coupled through a quasiharmonic potential, and a repulsive part is used for the excluded volume. This makes the beads behave like soft spheres, which become rigid as they come close together. This reproduces well the essential physics of the polymeric chain.

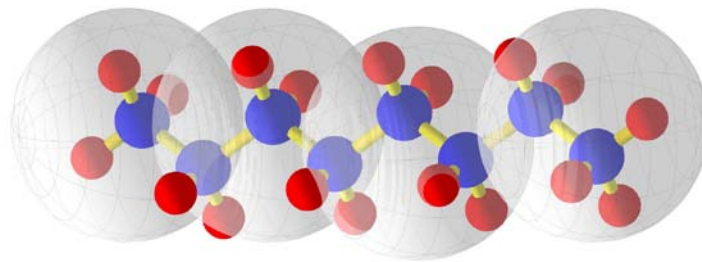


Figure 2.16. Schematic representation of a polymer chain, following the bead spring model. The real microstructure of the polymer can be seen as a chain composed of chemically bonded atoms of different nature (represented here by the red and blue spheres). In the bead spring model, the polymer is seen as a chain of sub-units, each representing groups of atoms or monomers (each sub-unit is represented here by the large transparent grey spheres).

2.3.3. Modeling the effects of the solvent

The process of cross-linking takes place with the polymer chains being held in solution. It is therefore important to introduce into the model the effect of the molecules of solvent, much smaller than the polymer chains, which constantly collide with the macromolecule and influence in its dynamic behavior. Once more, it is not practical to include an individual description of the molecules of solvent, because they are present in a very large number, which makes the computational cost unaffordable.

An elegant and efficient way of including the effect of solvent is to replace the Newton's equations of motion by the Langevin equation:

$$m_i \frac{d^2 \bar{r}_i}{dt^2} = \bar{F}_i - \gamma_i \frac{d\bar{r}_i}{dt} + \bar{R}_i(t)$$

As it can be seen, this equation adds two terms to the Newtonian description. The term $-\gamma_i \frac{d\bar{r}_i}{dt}$ represents a frictional drag (which is proportional to the velocity of the particle)

caused by the presence of the solvent. The term $\bar{R}_i(t)$ represents a random force, obeying fluctuation-dissipation processes.

2.4. References

1. G. Odian, *Principles of Polymerization*, Wiley, John Wiley & Sons, **2004**.
2. W. A. Braunecker, K. Matyjaszewski, *Prog. Poly. Sci.* **2007**, *32*, 93.
3. J. Chiefari, Y. K. (Bill) Chong, F. Ercole, J. Krstina, J. Jeffery, T. P. T. Le, R. T. A. Mayadunne, G. F. Meijs, C. L. Moad, G. Moad, E. Rizzardo, S. H. Thang, *Macromolecules* **1998**, *31*, 5559.
4. G. Moad, E. Rizzardo, S. H. Thang, *Aust. J. Chem.* **2005**, *58*, 379.
5. A. Favier, M. T. Charreyre, *Macromol. Rapid Commun.* **2006**, *27*, 653.
6. E. Rizzardo, J. Chiefari, B. Y. K. Chong, F. Ercole, J. Krstina, J. Jeffery, T. P. T. Le, R. T. A. Mayadunne, G. F. Meijs, C. L. Moad, G. Moad, S. H. Thang, *Macromol. Symp.* **1999**, *143*, 291.
7. H. Zheng, W. Bai, K. Hu, R. Bai, C. Pan, *J. Polym. Sci., Part A: Polym. Chem.* **2008**, *46*, 2575.
8. Theato, P., Klok, H.-A.; History of Post-Polymerization Modification. Functional Polymers by Post-Polymerization Modification: Concepts, Guidelines, and applications, 1st ed.; Wiley-VCH Verlag GmbH & Co. KGaA: Weinheim, Germany, 2013; pp. 1–44.
9. W. A. Cunningham, *Sulfur. III. J. Chem. Educ.* **1935**, *12*, 120.
10. G. E. Serniuk, F. W. Banes, M. W. Swaney, *J. Am. Chem. Soc.* **1948**, *70*, 1804.
11. L. M. Campos, K. L. Killops, R. Sakai, J. M. J. Paulusse, D. Dameron, E. Drokenmuller, B. W. Messmore, C. J. Hawker, *Macromolecules* **2008**, *41*, 7063.
12. S. M. Henry, M. E. H. El-Sayked, C. M. Pirie, A. S. Hoffman, P. S. Stayton, *Biomacromolecules* **2006**, *7*, 2407.
13. J. B. Beck, K. L. Killops, T. Kang, K. Sivanandan, A. Bayles, M. E. Mackay, K. Wooley, C. J. Hawker, *Macromolecules* **2009**, *42*, 5629.
14. N. Cengiz, H. Kabadayiglu, R. Sanyal, *J. Polym. Sci., Part A: Polym. Chem.* **2010**, *48*, 4737.
15. L. Wang, J. Kristensen, D. E. Ruffner, *Bioconjugate Chem.* **1998**, *9*, 749.
16. J.-H. Ryu, R. T. Chacko, S. Jiwanich, S. Bickerton, R. P. Babu, S. Thayumanavan, *J. Am. Chem. Soc.* **2010**, *132*, 17227.
17. J. R. Jones, C. L. Liotta, D. M. Collard, D. A. Schiraldi, *Macromolecules* **1999**, *32*, 5786.
18. H. Laita, S. Boufi, A. Gandini, *Eur. Polym. J.* **1997**, *33*, 1203.
19. S. Ohsawa, K. Morino, A. Sudo, T. Endo, *Macromolecules* **2011**, *44*, 1814.

20. J. Rieger, K. Van Butsele, P. Lecomte, C. Detrembleur, R. Jérôme, C. Jérôme, *Chem. Commun.* **2005**, 274.
21. A. Ruiz de Luzuriaga, N. Ormategui, H. J. Grande, I. Odriozola, J. A. Pomposo, I. Loinaz, *Macromol. Rapid Commun.* **2008**, 29, 1156.
22. L. Oria, R. Aguado, J. A. Pomposo, J. Colmenero, *Adv. Mater.* **2010**, 22, 3038.
23. I. Perez-Baena, I. Loinaz, D. Padro, I. Garcia, H. J. Grande, I. Odriozola, *J. Mater. Res.* **2010**, 20, 6916.
24. D. A. Fulton, *Org. Lett.* **2008**, 10, 3291.
25. D. Mecerreyes, V. Lee, C. J. Hawker, J. L. Hedrick, A. Wursch, W. Volksen, T. Magbitang, E. Huang, R. D. Miller, *Adv. Mater.* **2001**, 13, 204.
26. J. Jiang, S. Thayumanavan, *Macromolecules.* **2005**, 38, 5886.
27. 47. K. S. Park, D. Y. Kim, S. K. Choi, D. H. Suh, *Jpn. J. Appl. Phys.* **2003**, 42, 3877.
28. 11. E. Hart, B. Van Horn, V. Y. Lee, D. S. Germack, C. P. Gonzales, R. D. Miller, C. J. Hawker, *J. Amer. Chem. Soc.* **2002**, 124, 8653.
29. J. N. Dobish, S. K. Hamilton, E. Harth, *Polym. Chem.* **2012**, 3, 857.
30. T. A. Croce, S. K. Hamilton, M. L. Chen, H. Muchalski, E. Harth, *Macromolecules* **2007**, 40, 6028.
31. C. T. Adkins, H. Muchalski, E. Harth, *Macromolecules* **2009**, 42, 5786.
32. N. Ormategui, I. García, D. Padro, G. Cabañero, H. J. Grande, I. Loinaz, *Soft Matter* **2012**, 8, 734.
33. J. E. F. Radu, L. Novak, J. F. Hartmann, N. Beheshti, A.-L. Kjoniksen, B. Nyström, J. Borbély, *Colloid. Polym. Sci.* **2008**, 286, 365.
34. B. Zhu, G. Qian, Y. Xiao, S. Deng, M. Wang, A. Hu, *J. Mat. Chem.* **2011**, 21, 2679.
35. B. Zhu, S. Sun, Y. Wang, S. Deng, G. Qian, M. Wang, A. Hu, *J. Mater. Chem. C.* **2013**, 1, 580.
36. B. Zhu, G. Qian, Y. Xiao, S. Deng, M. Wang, A. Hu, *J. Polym. Sci. Part A: Pol. Chem.* **2011**, 49, 5330.
37. G. Qian, B. Zhu, Y. Wang, S. Deng, A. Hu, *Macromol. Rapid Commun.* **2012**, 33, 1393.
38. X. Jiang, H. Pu, P. Wang, *Polymer* **2011**, 52, 3597.
39. P. Wang, H. Pu, M. Jin, *J. Polym. Sci. Part A: Pol. Chem.* **2011**, 49, 5133.

40. A. Sanchez-Sanchez, I. Asenjo-Sanz, L. Buruaga, J. A. Pomposo, *Macromol. Rapid Commun.* **2012**, *33*, 1262.
41. M. Seo, B. J. Beck, J. M. Paulusse, C. J. Hawker, S. Y. Kim, *Macromolecules* **2008**, *41*, 6413.
42. E. J. Foster, E. B. Berda, E. W. Meijer, *J. Am. Chem. Soc.* **2009**, *131*, 6964.
43. J. He, L. Tremblay, S. Lacelle, Y. Zhao, *Soft Matter* **2011**, *7*, 2380.
44. B. S. Murray, D. A. Fulton, *Macromolecules* **2011**, *44*, 7242.
45. L. Buruaga, J. A. Pomposo, *Polymers* **2011**, *3*, 1673.
46. E. A. Appel, J. del Barrio, J. Dyson, L. Isaacs, O. A. Sherman, *Chem. Sci.* **2012**, *3*, 2278.
47. T. Akagi, P. Piyapakorn, M. Akashi, *Lagmuir* **2012**, *28*, 5249.
48. B. T. Tuten, D. Chao, C. K. Lyon, E. B. Berda, *Polym. Chem.* **2012**, *3*, 3068.

**Chapter 3. Scaling laws for
apparent molecular weight,
apparent polydispersity index,
hydrodynamic radius and
intrinsic viscosity in SCNPs**

3.1. Introduction and objectives

When adapting a synthesis process for a given application, it is important to have tools that help to adjust it, i.e. to define which precursor materials are needed, and what are the conditions of the process needed for obtaining a given result. In this context, simple theoretical descriptions, which do not require heavy computation, are very important.

The process studied here is the cross-linking reaction that transforms the polymer chain into the SCNP. When this collapse process occurs, many characteristics of the resulting SCNP are different from the linear precursor. In this chapter, the following four properties are analyzed: molecular weight, polydispersity index, hydrodynamic radius and intrinsic viscosity.

The chapter is divided in three main parts, each one addressing a different property (Figure 3.1):

- Derivation of the scaling law relating the apparent molecular weight of nanoparticles and their precursors, and the scaling law relating the polydispersity index of the SCNPs and that of their precursors. These relationships are important for justifying the apparent reduction in molecular weight and the polydispersity index narrowing observed in the SEC measurements when the chain collapse takes place. This part is focus strictly in the derivation of the scaling laws, and their validation through comparison with experimental data.
- Fitting of a scaling law relating the hydrodynamic radius of SCNPs to the molecular weight of precursors. This equation allows to understand how far SCNPs are from globular state when in solution.
- Fitting of a scaling law relating intrinsic viscosity to molecular weight. This relationship is applied to understand the effect of the nanoscopic architecture of the SCNP in the flow properties of the solution.

In order to validate the scaling laws as severely as possible, they were compared with large sets of data. These data have been obtained through an extensive bibliographic research from experiment works.

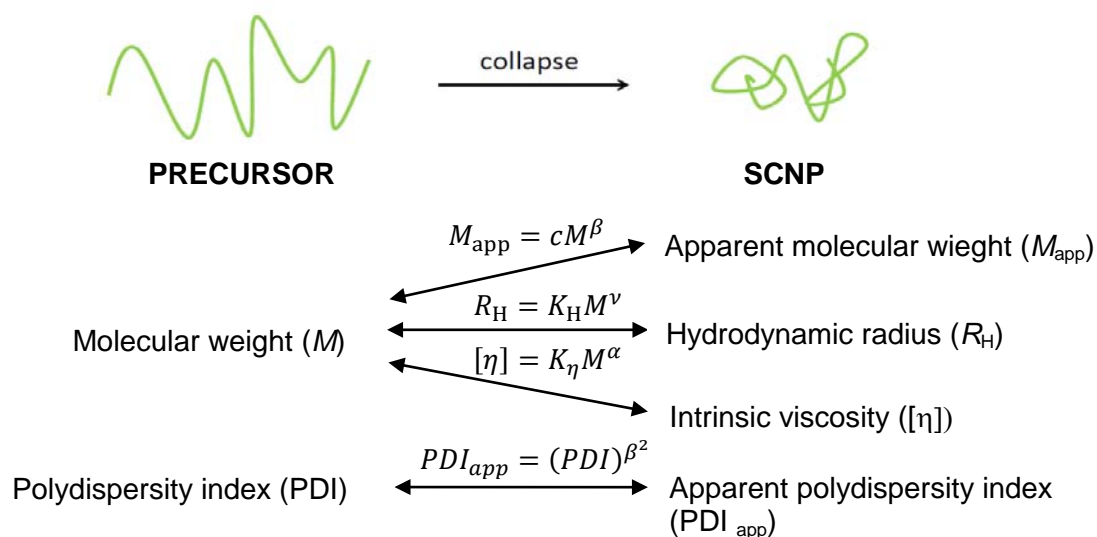


Figure 3.1. Scaling laws analyzed in this chapter.

3.2. Apparent molecular weight and polydispersity reduction upon intramolecular collapse of polydisperse chains to unimolecular nanoparticles

3.2.1. Introduction and objectives

SEC is used for determining the molecular weight averages and molecular weight distributions, although what it really measures is the hydrodynamic radius (R_H). Thus, this apparatus differentiate macromolecules according to their R_H .^[1] A theoretical framework describing several aspects of SEC was summarised in a previous work (Master Thesis) by the author of this Thesis, and can be found in Appendix I for consultation of the main concepts handled here.

Since intermolecular reactions give rise indefectibly to an increase in the molecular weight, a molecular weight reduction is a clear signature of intramolecular chain collapse (in the absence of secondary reactions during cross-linking like depolymerization, chain scission, etc.). As expected, when unimolecular particles of weight average molecular weight M_w are formed by intramolecular cross-linking of individual polymer chains, a significant reduction in R_H and, hence, apparent weight average molecular weight (M_w^{app}) is observed by SEC with traditional calibration.^[2-16] A concomitant reduction in polydispersity index (PDI) is often observed when intramolecular collapse occurs, resulting in an apparent polydispersity index (PDI_{app}) which often is lower than that of the polymer precursor. Henceforth, to simplify the nomenclature, weigh average molecular weight M_w , is going to be denoted as molecular weight M , and apparent weight average molecular weight M_w^{app} , is going to be denoted as apparent molecular weight M_{app} .

The main objective of this section is to obtain a general expression for the apparent SEC molecular weight (M_{app}) decrease and for the simultaneous apparent polydispersity index (PDI_{app}) narrowing observed upon collapse of polymer chains to unimolecular nanoparticles.

3.2.2. Apparent molecular weight decrease upon unimolecular nanoparticle formation

A. Theory

To obtain a general expression for the expected “apparent” SEC molecular weight (M_{app}), it was assumed that upon irreversible collapse of a polymer precursor of molecular weight M and density ρ , a fractal, soft nanoparticle was obtained. The hydrodynamic radius of such nano-object, R_H , could be defined as^[17,18]

$$R_H = K_H M^{\nu_F} = K_H M^{(1+\alpha_F)/3} \quad (3.1)$$

Where K_H is a constant and ν_F (or $\alpha_F = 3\nu - 1$) is a parameter related to the fractal nature of the nanoparticle which measures its deviation from the ideal “hard-sphere” state. Three cases of equation 3.1 are worth of mention:

Perfectly compact spheres (CS)

$$R_H = K_H^{CS} M^{(1+\alpha_F^{CS})/3} \quad (3.2)$$

$$\alpha_F = \alpha_F^{CS} = 0 \rightarrow \nu_F^{CS} = 1/3 \quad (3.3)$$

$$K_H = K_H^{CS} = \left[\frac{3}{4\pi N_A \rho} \right]^{1/3} \quad (3.4)$$

Where N_A is Avogadro’s number.

Nano-objects showing a fractal behavior very similar to that of linear polymer chains in a θ -solvent

$$R_H = K_H^\theta M^{(1+\alpha_F^\theta)/3} \quad (3.5)$$

$$\alpha_F = \alpha_F^\theta = \alpha_\theta \approx 0.5 \rightarrow \nu_\theta \approx 0.5 \quad (3.6)$$

$$K_H = K_H^\theta = K_\theta = \left[\frac{3K_\eta^\theta}{10\pi N_A} \right]^{1/3} \quad (3.7)$$

Where α_θ , and K_θ are constants of the precursor polymer in the Mark-Houwink-Sakurada equation: $[\eta] = K_\eta^\theta M^{\alpha_\theta}$

Nano-objects showing a fractal behavior very similar to that of linear polymer (LP) chains in good solvents

$$R_H = K_L M^{(1+\alpha_L)/3} \quad (3.8)$$

$$\alpha_F = \alpha_F^{LP} = \alpha_L \approx 0.76 \rightarrow \nu_L \approx 0.59 \quad (3.9)$$

$$K_H = K_H^{LP} = K_L = \left[\frac{3K_\eta^L}{10\pi N_A} \right]^{1/3} \quad (3.10)$$

Where α_L and K_L are constants of the precursor polymer in the Mark-Houwink-Sakurada equation: $[\eta] = K_\eta^L M^{\alpha_L}$

In general, for unimolecular fractal nanoparticles, $0 \leq \alpha_F \leq \alpha_L \approx 0.76$ (i.e., flexible chains, good solvent) is expected.

During SEC analysis with traditional calibration, the hydrodynamic radius of the collapsed nanoparticle is assimilated to that of an equivalent flexible chain of identical hydrodynamic radius, intrinsic viscosity $[\eta] = K_\eta^L M_{app}^{\alpha_L}$ and molecular weight M_{app} , according to:

$$R_H = K_L M_{app}^{(1+\alpha_L)/3} \quad (3.11)$$

Conceptually, the nanoparticle is hence “replaced” by an equivalent linear polymer chain of identical hydrodynamic radius and molecular weight M_{app} . By combining equations 3.1 and 3.11, the following equation is obtained:

$$M_{app} = c M^\beta \quad (3.12)$$

Where

$$c = \left(\frac{K_H}{K_L} \right)^{\frac{3}{1+\alpha_L}} \quad (3.13)$$

$$\beta = \frac{1 + \alpha_F}{1 + \alpha_L} \quad (3.14)$$

According to the above analysis, the lower value of β is estimated to be $\beta \approx 0.56$ ($\alpha_F = 0, \alpha_L \approx 0.76$) for compact, uniform particles and an upper value of $\beta \approx 1$ ($\alpha_F \approx 0.76, \alpha_L \approx 0.76$) for nano-objects showing a fractal behavior very similar to swollen flexible chains. So, in general, β should have a value between $0.56 \leq \beta \leq 1$.

B. Results

Figure 3.2 shows the experimental M_{app} versus M data obtained from the literature for intramolecular, irreversibly cross-linked polystyrene (PS) nanoparticles. These PS nanoparticles were synthesized using different chemical cross-linking groups, such as, vinyl,^[3,5] benzocyclobutene,^[2] *o*-quinodimethane^[8] and benzosulfone^[14] functional groups. Blue squares correspond to data in which the absolute molar by LS of the nanoparticles was reported and resulted to be in agreement, within experimental error, with the molar mass by SEC of the linear polymer precursor.^[2] These results cover a rather broad range in M corresponding to PS nanoparticles synthesized from precursor polymers containing around 20 mol% of cross-linking units and polydispersity (PDI) values less than 1.25. On the other hand, orange, purple, green and red symbols correspond to data in which the absolute molar mass by LS was not reported.^[3,5,8,14] Data from reference 14 referring to relatively high polydisperse ($\text{PDI}_{\text{app}} = 2$) PS nanoparticles containing an internal short fluorine rigid-rod core are distinguished by red diamonds. In general, the data for PS nanoparticles for which no absolute molar mass is available (orange, purple, green and red symbols) follow the same trend that the data corresponding to single-chain nanoparticles (blue squares).

In order to fit the data on Figure 3.2 (blue squares) by equation 3.12, it was considered that $M_{\text{app}} = M$ at the molecular weight of a monomer, $M_0 \approx 10^2$ Da. This seems to be reasonable assumption because polymer-like behavior cannot be expected at the monomer scale. With this constraint, a value of $\beta = 0.85$ is obtained from Figure 3.1 by data-fitting. Anyway, by changing this criterion to $M_{\text{app}} = M$ at $M \approx 500$ Da corresponding to a hypothetical precursor polymer with 20 mol% of cross-linking functional monomers and hence a single cross-linking monomer per chain (i.e., no self-cross-linked nanoparticles could be obtained from this precursor polymer) only a minor change in the β value is observed ($\beta = 0.83$). Consequently, the prior assumption can be retained of $M_{\text{app}} = M$ at $M_0 \approx 10^2$ Da, resulting in $\beta = 0.85$, with an estimated uncertainty of about 2%. This value of the power-law exponent is far from the value of perfectly compact, nonfractal nanoparticles ($\beta = 0.56$, dotted line in Figure 3.1) but also different from that expected for nano-objects with a fractal behavior similar to that of swollen polymer chains ($\beta = 1$, dashed line in Figure 3.2).

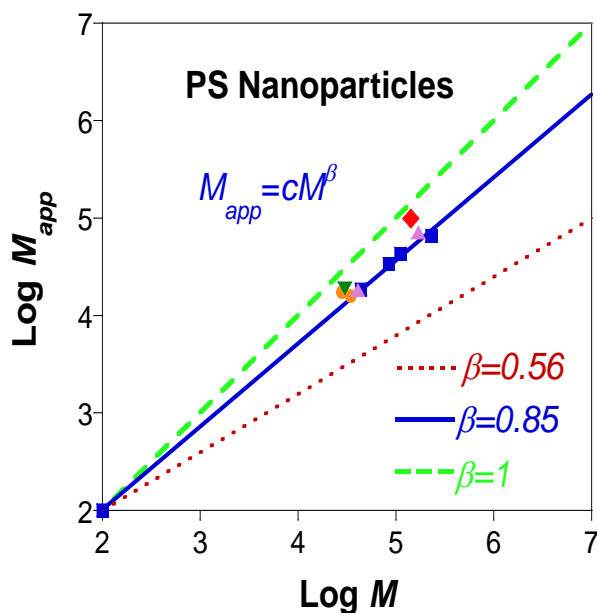


Figure 3.2. Apparent molecular weight (M_{app}) of PS nanoparticles vs. molecular weight (M) of the corresponding PS precursor. Squares, triangles, circles, inverted triangles and diamonds are experimental data from references 2,3,5,8 and 14, respectively. Dotted line corresponds to uniform, compact spheres ($\beta = 0.56$). Continuous line corresponds to fractal nanoparticles ($\beta = 0.85$) and dashed line corresponds to swollen polymer chains ($\beta = 1$).

From equation 3.14, a value of the fractal parameter $\alpha_F = 0.47$ is obtained by using $\beta = 0.85$ and $\alpha_L = 0.734$ for PS chains in tetrahydrofuran (THF).^[19] Such α_F value is close to that commonly found for linear polymer chains in θ -solvents ($\alpha_\theta \approx 0.5$).^[20,21] This suggests that intramolecular cross-linking in good solvent effectively screens the excluded volume interactions of the swollen precursor, leading to nearly Gaussian conformations for the resulting nanoparticles.^[20,21]

It is also interesting to compare experimental results for cyclic PS chains^[22,23] with the predictions about “equivalent” PS nanoparticles having a single intramolecular cross-linking point. By assuming 20 mol% of cross-linking functional monomers, PS nanoparticles with a single cross-linking point should be potentially obtained from oligomeric PS chains having 10 repeat units ($M \approx 10^3$ Da). On the basis of equation 3.12 ($\beta = 0.85$) we obtain $M_{app} \approx 710$ Da for hypothetical PS nanoparticles with a single cross-linking point arising from PS precursor chains of $M \approx 10^3$ Da.

$$\text{For } M = 10^2 \longrightarrow M = M_{app}$$

$$M_{app} = cM_{app}^\beta \longrightarrow 10^2 = c(10^2)^{0.85} \longrightarrow c = 1.995$$

$$M_{\text{app}} = 1.995(10^3)^{0.85} \longrightarrow M_{\text{app}} = 710 \text{ Da}$$

Experimentally, to calculate the apparent molecular weight, the intrinsic viscosity was used. The ratio of intrinsic viscosities of cyclic and linear PS chains was reported to be 0.71 in good solvent^[22,23] which translates to $M_{\text{app}} \approx 630$ Da for cyclic PS chains synthesized from linear PS chains of $M \approx 10^3$ Da.

$$\frac{[\eta]_{\text{C}}}{[\eta]_{\text{L}}} = 0.71 \longrightarrow \frac{[\eta]_{\text{C}}}{[\eta]_{\text{L}}} = \frac{KM_{\text{app}}^{\alpha_{\text{L}}}}{KM^{\alpha_{\text{L}}}} = 0.71 \longrightarrow M_{\text{app}} = M(0.71)^{1/\alpha_{\text{L}}}$$

$$M_{\text{app}} = 10^3(0.71)^{1/0.734} \longrightarrow M_{\text{app}} = 630 \text{ Da}$$

The main difference between both systems arises as a consequence of the random placement of the two cross-linking units in the case of PS nanoparticles when compared to the bonding between chain-ends in the case of cyclic PS chains. Giving the approximations involved, there is a good agreement between predictions for collapsed PS nanoparticles having a single intramolecular cross-linking point and experimental data for cyclic PS chains.

Figure 3.3 shows the experimental M_{app} versus M data obtained from the literature for intramolecular, irreversibly cross-linked poly(methyl methacrylate) (PMMA) nanoparticles. The data included for PMMA nanoparticles were obtained from different chemical cross-linking processes, like free-radical cross-linking of vinyl groups,^[3,4] thermal cross-linking of benzocyclobutene groups^[2] and alkyne-azide “click” chemistry.^[9] Unfortunately, data about absolute molar mass by LS for most of these PMMA nanoparticles was not available in the literature.

A data-fitting procedure similar to that performed in Figure 3.1 gave $\beta = 0.88$, which is very close to the value obtained for PS nanoparticles, although a larger data scatter is visible in Figure 3.3. For PMMA nanoparticles, the corresponding fractal parameter is estimated to be $\alpha_{\text{F}} = 0.52$ by using $\alpha_{\text{L}} = 0.731$ for PMMA in THF.^[24] Interestingly, the value of the fractal parameter for PMMA nanoparticles is also found to be similar to that of linear chains under θ -solvent conditions ($\alpha_{\theta} \approx 0.5$).^[20,21]

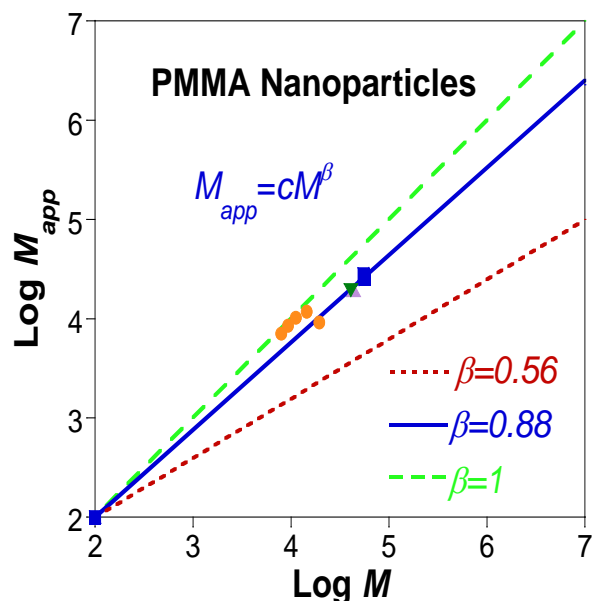


Figure 3.3. Apparent molecular weight (M_{app}) of PMMA nanoparticles vs. molecular weight (M) of the corresponding PMMA precursor. Squares, triangles, circles and inverted triangles are experimental data from references 2,3,4 and 9, respectively. Dotted line corresponds to uniform, compact spheres ($\beta = 0.56$). Continuous line corresponds to fractal nanoparticles ($\beta = 0.88$) and dashed line corresponds to nano-objects similar to swollen polymer chains ($\beta = 1$).

As it was done for PS, it is also interesting to compare the predictions about “equivalent” PMMA nanoparticles having a single intramolecular cross-linking point with experimental results for cyclic PMMA chains. From equation 3.12 ($\beta = 0.88$), a value of $M_{app} \approx 760$ Da is estimated for PMMA nanoparticles with a single cross-linking point arising potentially from linear PMMA chains of $M \approx 10^3$ Da.

$$\text{For } M = 10^2 \longrightarrow M = M_{app}$$

$$M_{app} = cM_{app}^\beta \longrightarrow 10^2 = c(10^2)^{0.88} \longrightarrow c = 1.738$$

$$M_{app} = 1.738(10^3)^{0.88} \longrightarrow M_{app} = 760$$

Experimentally, Glassner *et al.*^[25] have reported a ratio of the apparent molecular weight of cyclic PMMA chains to the molecular weight of the linear PMMA precursor chains of $M_{app}/M = 0.8$, providing $M_{app} = 800$ Da for cyclic PMMA chains obtained from linear PMMA chains of $M \approx 10^3$ Da.

Once again, a good agreement is observed between the predictions for collapsed nanoparticles having a single intramolecular cross-linking point and experimental data for cyclic chains, in spite of the presumably different topological structures involved.

Table 3.1 provides a comparison of M_{app} versus M data for other irreversibly collapsed nanoparticles of different chemical nature reported in the literature, including poly(ϵ -caprolactone) (PCL)-,^[3] poly(*n*-butyl acrylate) (PBA)-,^[2] poly(ethylene glycol/styrene) (PEGS)-,^[2] poly(carbonate) (PC)-^[7] and poly(benzyl acrylate) (PBzA)-based nanoparticles.^[9] For comparison, M_{app} data calculated from equation 3.12 were included, by assuming, to a first approximation, that $\alpha_F \approx 0.5$ and $\alpha_L \approx 0.7$ and $M_{app} = M$ at a molecular weight of $M_0 \approx 10^2$ Da for all the above systems. Given the assumptions involved, the agreement between experimental and calculated data is reasonably good, especially for nanoparticles synthesized from linear precursor polymers with high content of cross-linking units (> 15 mol%).

Table 3.1. Comparison of experimental and calculated M_{app} , for several intramolecular cross-linked nanoparticles reported in the literature.

System	Cross-linking (mol%) ^a	M (kDa)		M_{app} (kDa)
		exp ^b	exp ^c	calc ^d
PCL	15	20.5	15.7	11.0
PBA	20	73.0	27.8	33.6
PEGS	20	89.5	36.5	40.2
PC	38	64.9	37.5	30.3
PBzA	5	68.0	42.0	31.6

^a Content of cross-linking units in the linear precursor polymer.

^b Weight-average molecular weight of the linear precursors as determined by SEC with traditional calibration.

^c Weight-average molecular weight of the resulting intramolecular cross-linked nanoparticles as determined by SEC with traditional calibration.

^d Weight-average molecular weight values calculated from equation 3.12 by assuming $\alpha_F \approx 0.5$, $\alpha_L \approx 0.7$ and $M_{app} = M$ at a molecular weight of $M_0 \approx 10^2$ Da.

3.2.3. Apparent polydispersity narrowing upon unimolecular nanoparticle formation

A. Theory

As a direct consequence of the validity of equation 3.12 for quantifying the apparent molecular weight decrease upon intramolecular chain collapse, a reduction in apparent polydispersity index (PDI) is expected.

For the sake of simplicity, it will be assumed that the molecular weight distribution (*MWD*) function of the linear polymeric precursor follows a log-normal function^[26] such as

$$W(M) = \frac{1}{M\sigma_1\sqrt{2\pi}} \exp\left[-\frac{(\ln M - \mu_1)^2}{2\sigma_1^2}\right] \quad (3.15)$$

Where σ_1 and μ_1 are the parameters that control the *MWD* according to

$$\bar{M}_n = \exp\left[\mu_1 + \frac{1}{2}\sigma_1^2\right] \quad (3.16)$$

$$\bar{M}_w = \exp\left[\mu_1 + \frac{3}{2}\sigma_1^2\right] \quad (3.17)$$

$$PDI \equiv \frac{\bar{M}_w}{\bar{M}_n} = \exp[\sigma_1^2] \quad (3.18)$$

Upon intramolecular collapse of the linear precursor, a shift in the *MWD* is expected from $W(M)$ to $W(M_{app})$ according to the scaling law: $M_{app} = cM^\beta$ (equation 3.12). Hence, equation 3.15 becomes

$$W(M_{app}) = \frac{1}{M_{app}\sigma_2\sqrt{2\pi}} \exp\left[-\frac{(\ln M_{app} - \mu_2)^2}{2\sigma_2^2}\right] \quad (3.19)$$

where $\sigma_2 = \beta\sigma_1$ and $\mu_2 = \ln c' + \beta\mu_1$. Consequently:

$$PDI_{app} = (PDI)^\beta \quad (3.20)$$

Since $\beta < 1$, the apparent SEC polydispersity is expected to decrease upon unimolecular nanoparticle formation.

B. Results

Figure 3.4 shows two graphics of PDI_{app} of intramolecular cross-linked nanoparticles vs. PDI of the corresponding polymeric precursors for PS systems (top) and PMMA systems (bottom). The data are compared with theoretical values based on equation 3.20 using the values of β determined previously (Figure 3.2 and 3.3). It is worth mentioning two contributions to polydispersity which were not explicitly accounted for in equation 3.20, the first one is the inherent heterogeneous nature of the intramolecular cross-linking process and the second contribution is the potential presence of residual, minor amounts of intermolecular byproducts in some systems.

Hence, intramolecular cross-linking is a statistical process taking place inside each polymer chain in which formation of a given bond has a strong influence on the reactivity of its neighbors. Because of conformational fluctuations during chain collapse at constant temperature, certain differences in reactivity along the chain are expected even for chains having exactly the same length. Furthermore, the cross-linking process introduces severe topological constraints in orientation and distance between cross-linking groups along the chain that reduce subsequent intramolecular reactivity. This inhibition of the cross-linking process is more apparent at the late stages of the intramolecular chain collapse where often due to rigidity effects there is a fraction of cross-linking groups that are never able to find a partner.^[27] Consequently, topological “freezing” is expected to contribute to a relative increase in PDI when compared to theoretical predictions. The reason for this increase is that different nanoparticles will show different fractions of unreacted cross-linkers. Having noted this, it must be stressed that even for the ideal case in which all cross-linking groups have reacted and formed a permanent bond, the resulting nanoparticles will exhibit different topologies as a consequence of the stochastic character of the cross-linking process.

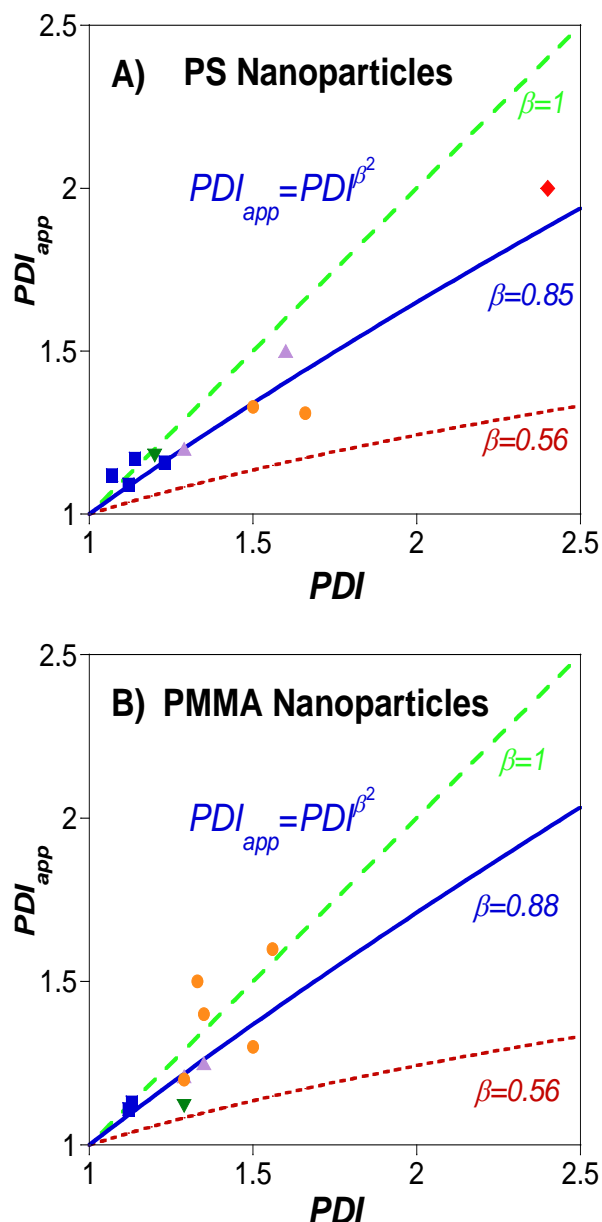


Figure 3.4. PDI_{app} of intramolecular cross-linked nanoparticles vs. PDI of the corresponding polymeric precursors for (A) PS nanoparticles and (B) for PMMA nanoparticles. Identical symbols to those used in Figure 3.1 and 3.2 are employed. Predictions from $PDI_{app} = (PDI)^{\beta^2}$ at different values of β are also drawn as dashed, continuous and dotted lines.

Moreover, PDI is a parameter very sensitive to the presence of high molecular weight tails arising from minor quantities of byproducts generated by intermolecular secondary reactions.^[2] In particular, the strong scatter of the experimental data observed in Figure 3.4b could be also tentatively attributed to the presence of residual, minor amounts of intermolecular byproducts.

Table 3.2 provides a comparison of PDI_{app} versus PDI data for other irreversibly collapsed nanoparticles of different chemical nature reported in the literature, such as,

PCL-,^[3] PBA-,^[2] PEGS-,^[2] PC-^[7] and PBzA-based nanoparticles^[8] as well as theoretical predictions from equation 3.20 by using to a first approximation, $\beta = 0.88$ (i.e., by using $\alpha_F = 0.5$ and $\alpha_F^{LP} \approx 0.7$). In general, equation 3.20 is able to reproduce the experimental trend rather well in spite of several approximations involved, though systematic deviations are found, with the experimental values of PDI_{app} being somewhat higher than the theoretical values. Thus, the aforementioned effects related to heterogeneity and/or intermolecular reactions might partially compensate the stronger reduction of PDI predicted by equation 3.20.

Table 3.2. Comparison of experimental and calculated PDI_{app} for several intramolecular cross-linked nanoparticles reported in the literature.

System	Cross-linking (mol%) ^a	PDI exp ^b	PDI_{app} exp ^c	PDI_{app} calc ^d
PCL	15	1.35	1.35	1.26
PBA	20	1.09	1.10	1.07
PEGS	20	1.11	1.09	1.08
PC	38	1.20	1.19	1.15
PBzA	5	1.28	1.26	1.21

^a Content of cross-linking units in the linear precursor polymer.

^b Polydispersity index values of the linear precursors as determined by SEC with traditional calibration.

^c Polydispersity index values of the resulting intramolecular cross-linked nanoparticles as determined by SEC with traditional calibration.

^d Polydispersity index values calculated from equation 3.20 by assuming $\alpha_F \approx 0.5$ and $\alpha_L \approx 0.7$.

3.2.4. Conclusions

Two general expressions have been obtained, one for the apparent molecular weight and the other for the apparent polydispersity, in order to quantify the reduction observed by SEC with traditional calibration when irreversible, intramolecular collapse of individual polymer chains occurs.

For the case of the apparent molecular weight, most of the available experimental data in the literature for intermolecular cross-linked nanoparticles covering different polymer chemistries follow a $M_{app} \propto M^\beta$ scaling law where $\beta = (1 + \alpha_F)/(1 + \alpha_L)$, α_F being a parameter related to the fractal and soft nature of the nanoparticle and α_L the Mark-Houwink-Sakurada exponent of the precursor polymer in good solvent. Experimental values of β are typically around 0.85-0.88, as illustrated in Figures 3.1 and 3.2 for PS

and PMMA nanoparticles, suggesting values of the fractal parameter α_F around 0.47-0.52 and hence pointing to a hydrodynamic behavior of the nanoparticles “equivalent” to that of linear polymer chains in θ -solvents. This behavior can be attributed to the partially collapsed nature of the soft nanoparticles since for totally compact, spherical particles a value of $\alpha_F = 0$ is expected.

The above $M_{app} \propto M^\beta$ power law has significant impact on the apparent polydispersity reduction of the unimolecular nanoparticles. Hence, for a precursor displaying a log-normal MWD function $PDI_{app} = (PDI)^\beta$ was obtained, where PDI and PDI_{app} are the polydispersity index of the precursor and the unimolecular nanoparticles, respectively. Experimental data are consistent with this scaling-law although due to the inherent heterogeneous nature of the intramolecular cross-linking process and/or the presence of intermolecular cross-linking reactions significant data scatter is observed for some systems.

3.3. How far are single-chain polymer nanoparticles in solution from the globular state?

3.3.1. Introduction and objectives

As previously mentioned, single-chain polymer nanoparticles are soft nano-objects obtained from a collapse of polymer precursors containing reactive functional groups placed randomly along the polymer chain.^[28,29] In many published works, it has been implicitly assumed that these nano-objects in good solvent show a globular conformation. However, very recent scattering experiments by SANS and SAXS,^[30-32] as well as complementary molecular dynamic (MD) simulations,^[33,34] point to a non-compact, non-globular morphology of SCNPs in solution.

Representative examples are illustrated in Figure 3.5a-e. Figure 3.5a shows the typical extended conformation of a linear precursor under good solvent conditions from MD simulations. Figure 3.5b shows the typical sparse morphology of SCNPs in solution revealed by MD simulations.^[33,34] Even by using the same precursor, cross-linking initiated from different (statistical) cross-linking configurations leads to highly polydisperse topologies of the resulting SCNPs.^[33,34] Such morphologies resemble those observed in intrinsically disordered proteins (IDPs) with locally compact portions of the peptide chain connected by flexible segments (Figure 3.5c). As illustrated in Figure 3.5d, the Kratky plot for the scattering form factor of PMMA-SCNPs (empty circles) is qualitatively similar to that of IDPs (solid lines) and rather different from that of compact globular proteins (dashed line).^[35] In this figure, $I(Q)$, Q and R_g are the scattered intensity, wavevector and radius of gyration, respectively. Figure 3.5e shows the elongated structure in water of non-covalent bonded SCNPs with pendant hydrogen bonding motifs as it has been recently deduced from SANS measurements.^[36]

All these evidences mentioned above against a compact, globular morphology of SCNPs in solution, suggest that this behavior could be a general trend. So, the objective of this part of the chapter is to obtain a clear idea of how far current SCNPs are from the globular state. For that, hydrodynamic radius (R_H) from a large number of SCNPs in solution were compiled and compared to the corresponding hydrodynamic radius for compact or partially swollen globules of the same nature and molar mass. In addition, using the hydrodynamic radius of SCNPs in the power-law relation of $R_H \propto M_w^\nu$, the value of the scaling exponent ν is obtained, allowing the quantification of how far current SCNPs in solution are from the globular state.

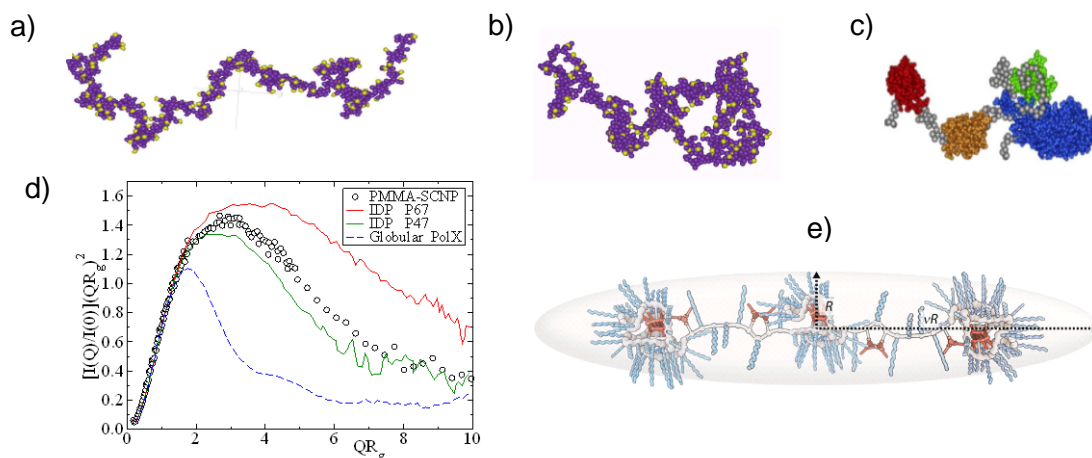


Figure 3.5. a) Typical conformation of a linear precursor under good solvent conditions from MD simulations. b) Typical conformation of a SCNP revealed by MD simulations. c) The SCNP morphology illustrated in b) resembles that adopted by intrinsically disordered proteins with locally compact portions of the peptide chain connected by flexible segments. d) Kratky plot for the form factors of PMMA-SCNPs (symbols), compared with that of IDPs (solid lines)^[35] and globular proteins.^[35] e) Elongated structure of SCNPs with pendant hydrogen bonding motifs deduced from recent SANS measurements.

A. Results

Table 3.3 summarizes the comparison between hydrodynamic size data for polystyrene single-chain polymer nanoparticles (PS-SCNPs) in solution and the predicted size data for compact and partially swollen PS globules of the same M_w . PS-SCNPs were synthesized from 30 different precursors and 11 different cross-linking chemistries, including covalent bonds (CBs),^[2,3,13,37-42] dynamic covalent bonds (DCBs)^[43] and non-covalent bonds (NCBs).^[44]

Hydrodynamic size of the PS precursor was calculated according to: $R_H^{SEC}(nm) = 1.44 \cdot 10^{-2} M^{0.561}$, which is the recommended expression^[19] for estimating the hydrodynamic radius of low-dispersity PS chains based on M_w data from SEC in THF calibrated with PS standards. The hydrodynamic radius of SCNPs was obtained as $R_H^{SEC}(nm) = 1.44 \cdot 10^{-2} M_{app}^{0.561}$ using the M_{app} data from SEC in THF.^[45] Hydrodynamic size data as determined from DLS measurements in THF (R_H^{DLS}) are also provide in Table 3.3, when available, for comparison. Data in which R_H^{DLS} (PS-SCNP) > R_H^{SEC} (PS-precursor) are indicated in parentheses. This inconsistency in some of the reported DLS values might be attributed to an underestimation of the value of R_H^{SEC} (PS-precursor) or to the presence of inter-chain aggregates in the samples leading to R_H^{DLS} (PS-SCNP) > R_H^{SEC} (PS-precursor). In general a good agreement is found between R_H^{SEC} and R_H^{DLS} data.

Last columns in Table 3.3 provide the hydrodynamic radii for compact and partially swollen PS globules with a M_w value identical to that of the SCNP precursor according to the expression:^[46] $R_H^\phi = [3M_w/(4\pi\phi\rho N_A)]^{1/3}$, where ϕ is the segment volume fraction in a spherical globule ($\phi = 1$ for solid-like globules; $\phi = 0.8$ for partially swollen globules with 20% solvent content), ρ is the density of PS (1.05 g/cm³) and N_A is Avogadro's number.

From the data of Table 3.3, it was observed that the hydrodynamic radius (R_H^{SEC} and R_H^{DLS}) of a PS-SCNP was, in general, larger than that of a compact or partially swollen PS globule of the same molecular weight, independently of the intrachain cross-linking chemistry used to synthesize the PS-SCNP.

Moreover, analyzing the PS-SCNP size data in terms of the power-law relation $R_H \propto M^\nu$, it is possible to quantify how far are current nanoparticles from the globular conformation. It is well-known that for linear polymers the specific value of ν depends on the particular state of the chain, with a value *ca.* $\nu_F = 0.59$ (Flory exponent) for the expanded coil state (i.e., chain in good solvent), 1/2 for the θ -state and 1/3 for the most compact globule state.^[47] In Figure 3.6 different graphics are shown. Figure 3.6a illustrated the $R_H^{\text{SEC}} = KM_w^\nu$ scaling law for PS-SCNPs synthesized from PS precursors containing 20 mol% of reactive functional groups (closed circles). Open circles are R_H data from DLS measurements (R_H^{DLS}). In general, a good agreement is observed between R_H^{SEC} and R_H^{DLS} data. Fitting the R_H^{SEC} data to $R_H^{\text{SEC}} = KM_w^\nu$, a value of $\nu = 0.48$ is obtained. The red line corresponds to the linear precursor, the solid green line corresponds to compact globules and the dashed green line corresponds to partially swollen globules.

As illustrated in Figure 3.6b, the value of the exponent ν in the $R_H^{\text{SEC}} = KM_w^\nu$ scaling law for the PS-SCNPs decreases progressively, upon increasing the amount of reactive cross-linker (X-linker) functional groups in the PS precursor, thus, for precursors with 5, 15 and 30 mol% of X-linker functional groups, values of 0.52, 0.49 and 0.47 are obtained, respectively. All these ν values are close to that of the θ -state and far from the value of 0.33 expected for compact globules. Following the trend, it is assumed the existence of a plateau above 30 mol% of X-linker in the precursor, which means that a further increase in X-linker content is not expected to be efficient for compaction. This feature is in agreement with MD simulations.^[33] The red line in Figure 3.6 corresponds to the value of the exponent ν for expanded coils ($\nu = 0.59$) and the green line corresponds to the value of the exponent ν for globule state ($\nu = 1/3$).

Figure 3.6c shows similar results to those of Figure 3.6a, for poly(methyl methacrylate) single-chain nanoparticles (PMMA-SCNPs) in solution synthesized from linear precursors containing 20 mol% of reactive functional groups (Table 3.4). A good agreement is again observed between R_H^{SEC} and R_H^{DLS} data. Fitting the data to $R_H^{\text{SEC}} = KM_w^\nu$, a value of $\nu = 0.51$ is obtained. For comparison, the values of ν reported for chemically denatured, intrinsically disordered and folded proteins are 0.57, 0.51 and 0.29, respectively.^[48,49] Thus, chemically denatured proteins behave as expanded coil in solution ($\nu \approx 0.59$), whereas folded proteins follow the scaling law expected for compact globules ($\nu \approx 0.33$). The values obtained in Figures 3.6a and 3.6c for the exponent ν for PS-SCNPs and PMMA-SCNPs are within statistics consistent with those of linear chains in the θ -state, or intrinsically disordered proteins in solution ($\nu \approx 0.5$).

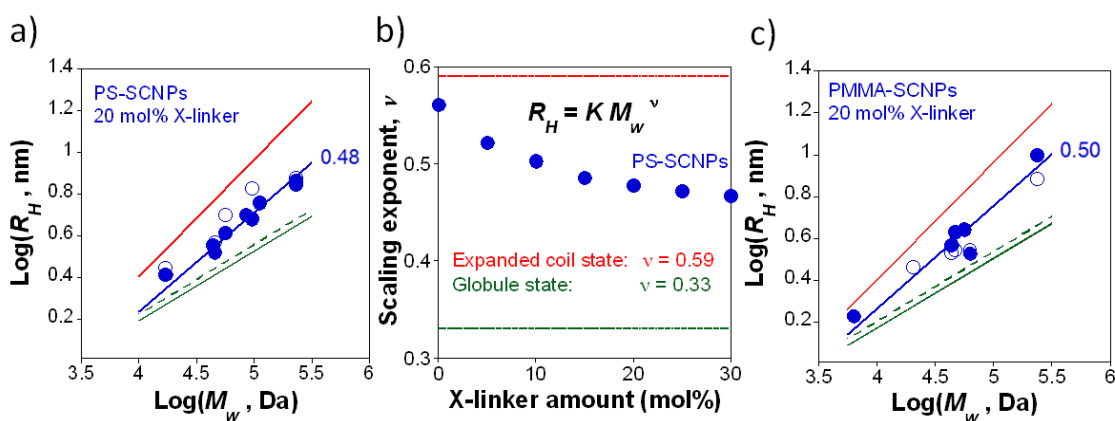


Figure 3.6. (a) Representation of $\log R_H$ vs. $\log M_w$ for PS-SCNPs synthesized from polymer precursors containing 20 mol% of cross-linking groups. (b) Representation of the exponent ν vs. the amount of reactive cross-linking groups in the polymer precursor. (c) The same graphic that (a) but for PMMA-SCNPs synthesized from polymer precursors containing 20 mol% of cross-linking groups.

Table 3.3. Size data for PS-SCNPs synthesized from different precursors and intrachain cross-linking chemistries compared to the predicted size data for compact and partially swollen PS globules.

	Precursors				SCNPs					Globules	
	x (mol %) ^a	M_w (kDa) ^b	PDI ^c	R_H^{SEC} (nm) ^d	Type ^e	Crosslinking Chemistry	M_{app} (kDa) ^f	R_H^{SEC} (nm) ^d	R_H^{DLS} (nm) ^g	$R_H^{\phi=1}$ (nm) ^h	$R_H^{\phi=0.8}$ (nm) ⁱ
1	10	172.8	1.60	12.5	CBs	Radical coupling ^[3]	70.5	7.6	9.2	4.0	4.3
2	16	41.3	1.29	5.6			18.0	3.5	5.4	2.5	2.7
3	10	112.0	1.10	9.8	CBs	Benzo-cyclobutene dimerization ^[2]	56.0	6.6	6.2	3.5	3.8
4	10	233.0	1.26	14.8			91.5	8.7	9.5	4.4	4.8
5	15	110.0	1.16	9.7			42.2	5.7	-	3.5	3.7
6	15	235.0	1.23	14.8			80.3	8.1	-	4.4	4.8
7	20	44.0	1.07	5.8			18.5	3.6	-	2.4	2.6
8	20	85.0	1.14	8.4			34.0	5.0	-	3.0	3.3
9	20	111.0	1.15	9.7			42.8	5.7	-	3.3	3.6
10	20	230.0	1.21	14.7			66.0	7.3	-	4.2	4.6
11	25	229.0	1.25	14.6			62.0	7.0	6.4	4.4	4.8
12	10	38.0	1.07	5.3			CBs	Isocyanate-amine coupling ^[13]	14.0	3.1	4.4 ^j
13	10	72.0	1.19	7.6	50.5	6.3			5.9 ^j	3.0	3.2
14	15	118.8	1.20	10.1	CBs	CuAAC ^k click chemistry ^[37]	76.5	7.9	5.0	3.3	3.6
15	15	46.9	1.54	6.0	CBs	Nitrene	24.9	4.2	(8.0)	2.6	2.8

Chapter 3. Scaling laws for apparent molecular weight, apparent polydispersity index, hydrodynamic radius and intrinsic viscosity in SCNPs

16	20	47.1	1.46	6.0		chemistry ^[38]	20.6	3.8	(7.5)	2.6	2.8
17	10	39.2	1.37	5.4	CBs	Benzoxazine chemistry ^[39]	24.8	4.2	(6.1)	2.5	2.6
18	10	147.9	1.62	11.4			67.0	7.3	10.6	3.8	4.1
19	15	42.8	1.33	5.7			22.7	4.0	5.7	2.5	2.7
20	15	79.1	1.31	8.1			29.5	4.6	7.1	3.1	3.3
21	20	56.2	1.46	6.7			23.5	4.1	5.1	2.8	3.3
22	20	95.6	1.48	9.0			31.5	4.8	6.8	3.3	3.6
23	19	57.1	1.18	6.7			CBs	Glaser-Hay coupling ^[40]	25.1	4.2	5.5
24	9	18.4	1.22	4.5 ^l	CBs	Diels/Alder ligation ^[41]	13.6	3.0	3.5	1.9	2.1
25	17	22.1	1.33	4.0 ^l			15.9	3.3	2.5	2.0	2.2
26	34	31.5	1.56	4.0 ^l			21.7	3.9	(0.8) ^m	2.3	2.5
27	20	45.8	1.83	5.9	CBs	Tetrazine-norbornene chemistry ^[42]	16.3	3.3	3.7	2.6	2.8
28	21	17.3	1.27	2.7 ^l	DCBs	Hydrazone chemistry ^[43]	10.7	2.6	(2.8)	1.9	2.0
29	9	27.6	1.17	4.8 ^l	NCBs	Ureido-pyrimidinone dimerization ^[44]	22.5	4.0	4.4	2.2	2.4
30	9	33.6	1.17	6.3 ^l			28.4	4.5	5.7	2.3	2.5

^a Relative amount of functional groups in the PS linear precursor. ^b Weight average molecular weight referred to PS standards. ^c Polydispersity index referred to PS standards. ^d For the PS polymer precursors: $R_H^{SEC}(nm) = 1.44 \cdot 10^{-2} (M_w)^{0.561}$,^[19] for the PS-SCNPs: $R_H^{SEC}(nm) = 1.44 \cdot 10^{-2} (M_{app})^{0.561}$.^[45] ^e CBs = Covalent bonds. DCBs = Dynamic covalent bonds. NCBs = Non-covalent bonds. ^f M_{app} of the SCNP referred to PS standards.^[45] ^g Data from DLS measurements. In parentheses: data in which $R_H^{DLS}(\text{SCNP}) > R_H^{SEC}(\text{precursor})$. ^h Compact PS globules: $R_H^{\phi=1} = [3M_w / (4\pi\phi\rho N_A)]^{1/3}$ with $\phi = 1$ and $\rho = 1.05 \text{ g/cm}^3$.^[46] ⁱ Partially swollen PS globules (solvent content: 20%): $R_H^{\phi=0.8} = [3M_w / (4\pi\phi\rho N_A)]^{1/3}$ with $\phi = 0.8$.^[46] ^j Chloroform as solvent. ^k CuAAC = Copper(I)-catalyzed azide alkyne cycloaddition. ^l Experimental value of the hydrodynamic radius from DLS experiments in THF. ^m Shown in parentheses because $R_H^{DLS}(\text{SCNP}) < R_H^{\phi=1}$.

SCNPs based on PMMA and PS precursors are the systems with the largest collection of data available in the literatures (Tables 3.3 and 3.4). Although many other SCNPs systems obtained from different polymer precursors have been characterized (Table 3.5), data sets for each individual system are limited in most cases, and fits of such sets to an scaling law $R_H \propto M_w^\nu$ are not reliable. However, using the whole set of data^[2,3,5,7-9,13,15,16,37-44,50-64] in Tables 3.3, 3.4 and 3.5, a qualitative universal trend of the scaling behavior of the SCNPs is obtained. Figure 3.7 shows all data for R_H reported in the literature for SCNPs vs. the data of the respective precursors. The polymer precursors must scale as $R_{H\text{ prec}} = b_{\text{prec}} M_w^{\nu_F}$ (ideal chains in good solvent, with $\nu_F = 0.59$) and the SCNPs as $R_{H\text{ nanop}} = b_{\text{nanop}} M_w^\nu$ (with some *a priori* unknown exponent ν). The length scale b is the size of the statistical segment.^[47] From the former equations the size of the SSCP and the precursor can be related as $R_{H\text{ nanop}} = a [R_{H\text{ prec}}]^{v/\nu_F}$, with the prefactor $a = b_{\text{nanop}} / (b_{\text{prec}}^{v/\nu_F})$. Because of the same chemistry of SSCP and precursor, b_{nanop} and b_{prec} are essentially identical. Moreover, b is generally of the order of 1-2 nm^[65] for common polymers as those of Tables 3.3, 3.4 and 3.5. Therefore, in the units of Figure 3.7, the prefactor a is of the order of 1, which is irrelevant within the statistic of the data. The dashed black line in graphic (a) is the best fit for all data of $R_{H\text{ prec}}^{\text{SEC}}$ for $R_{H\text{ nanop}}^{\text{SEC}} = a [R_{H\text{ prec}}^{\text{SEC}}]^{v/\nu_F}$, giving a exponent $\nu = 0.48$, which is included in (b) for comparison. This value provides information about the average value of the scaling exponent ν and it is consistent with the values obtained from the specific analysis of PS-SCNPs and PMMA-SCNPs with 20% of X-linkers (Figures 3.6a and 3.6c). For comparison, two limiting cases were included, the dashed green line that corresponds to $\nu = \nu_F = 0.59$ and $a = 1$, which indicates the case of no reduction of the nanoparticle size respect to the precursor ($R_{H\text{ nanop}} = R_{H\text{ prec}}$), and the dashed blue line that corresponds to compact globular SCNPs, $\nu = 1/3$ with $\phi = 1$.

Analyzing the data in Figure 3.7, it was observed that SCNPs in solution do not display a compact, globular morphology. Instead, they showed within statistics the behavior expected for chain in θ -solvent or for intrinsically disordered proteins, confirming the physical picture proposed by recent scattering experiments and MD simulations.^[30-34] The simulation revealed that, because of the intrinsically self-avoiding character of the polymer precursors in good solvent, reaction between X-linkers separated by long contour distances (creating long-range loops) is severely restricted. As a consequence, most of the cross-linking events are actually inefficient for global compactation, since they involve X-linkers that are separated by short contour distances. Indeed for this reason, increasing the amount of X-linkers in the precursor does not significantly

improve the efficiency of folding into compact structures (Figure 3.6b). This mostly leads to an increase of the short-range cross-linking events, which just produce *local* globulation (resembling the behavior of chains in θ -solvent or IDPs), but at large scales SCNPs are open, sparse objects showing just a few amount of long-range loops (Figure 3.5b).

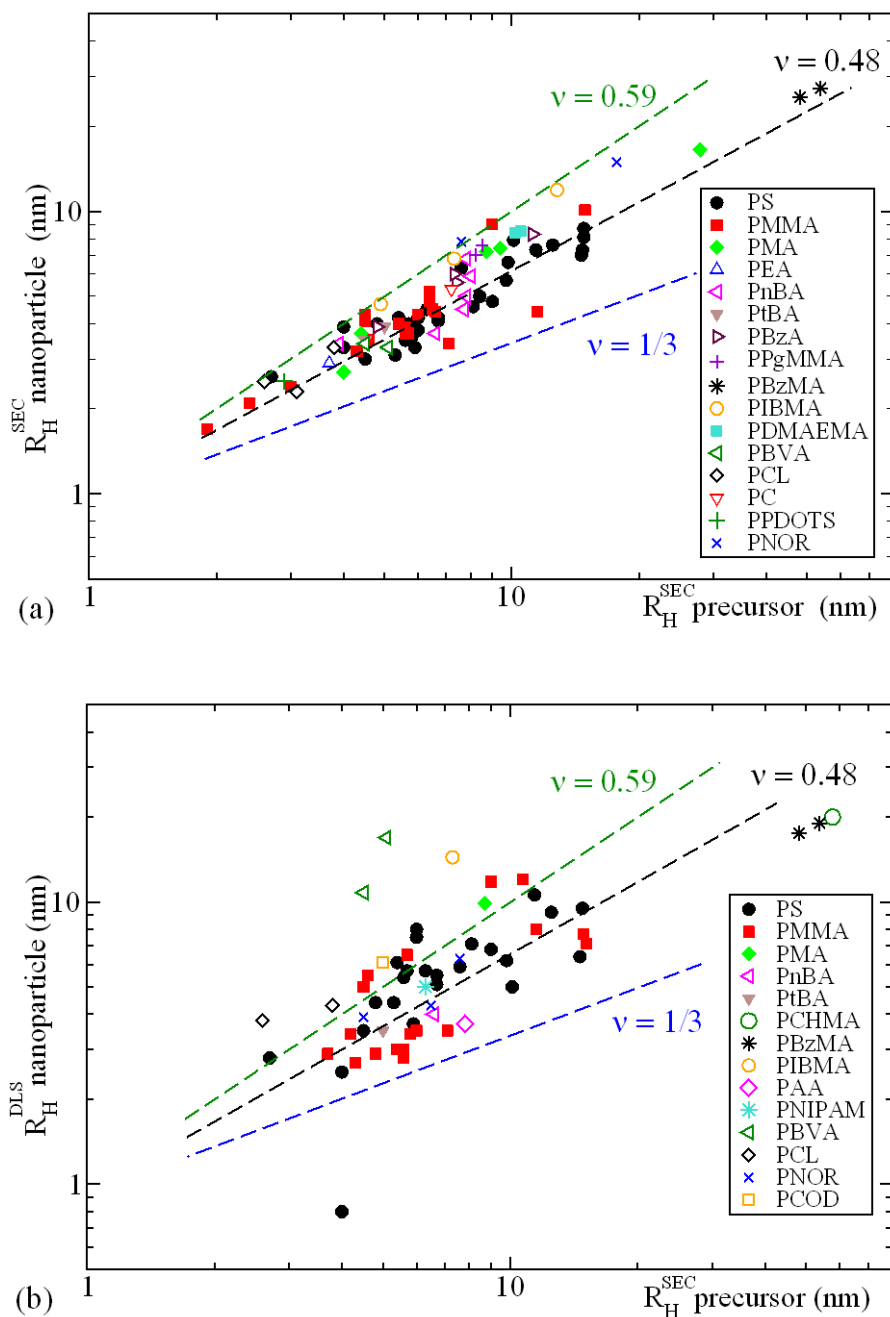


Figure 3.7. Illustration of the hydrodynamic radii reported in the literature^[2,3,5,7-9,13,15,16,37-44,50-64] for SCNPs and their precursors. All the values are given in Tables 3.3, 3.4 and 3.5. In both graphics abscissas are the values obtained for the precursors by SEC. Ordinates are the respective values for the nanoparticles obtained by SEC (a) and DLS (b). Data for different systems are represented with different symbols (see legends).

Table 3.4. Size data for PMMA-SCNPs synthesized from different precursors and cross-linking chemistries compared to predicted size data for compact and partially swollen PMMA globules.

	Precursors				SCNPs						Globules	
	x (mol%) ^a	M_w (kDa) ^b	PDI ^c	R_H^{SEC} (nm) ^d	Type ^e	Crosslinking Chemistry	M_{app} (kDa) ^f	R_H^{SEC} (nm) ^d	R_H^{DLS} (nm) ^g	$R^{TEM/AFM}$ (nm) ^h	$R_H^{\phi=1}$ (nm) ⁱ	$R_H^{\phi=0.8}$ (nm) ^j
1	8	29.0	1.32	4.6	CBs	Radical coupling ^[3]	17.5	3.5	(5.5)	-	2.1	2.3
2	23	43.2	1.35	5.7			19.5	3.7	(6.5)	3.6 ^k	2.4	2.6
3	10	52.5	1.14	6.4	CBs	Benzo- cyclobutene dimerization ^[3]	36.5	5.2	-	-	2.6	2.8
4	15	54.5	1.12	6.5			28.0	4.5	-	-	2.6	2.8
5	20	56.0	1.13	6.6			26.9	4.4	-	-	2.6	2.8
6	15	149.0	1.23	11.5	CBs	Isocyanate- amine coupling ^[13]	26.6	4.4	8.0	-	3.7	3.9
7	4	38.9	1.27	5.4	CBs	CuAAC ^l click chemistry ^[9,37]	22.3	4.0	3.0	-	2.3	2.5
8	7	41.7	1.22	5.6			21.6	3.9	3.0	-	2.4	2.6
9	10	41.0	1.29	5.6			19.4	3.7	2.8	3.3 [*]	2.4	2.6
10	20	62.4	1.30	7.1			16.9	3.4	3.5	-	2.7	3.0
11	4	52.3	1.44	6.4	CBs	Bergman cyclization ^[50]	31.5	4.8	-	6.4 ^{**}	2.6	2.8
12	4.4	13.4	1.49	3.0			9.3	2.4	-	-	1.6	1.8
13	20	6.3	1.29	1.9			5.0	1.7	-	-	1.3	1.4
14	5	9.1	1.43	2.4	CBs	Nitrene chemistry ^[38]	7.4	2.1	-	-	1.4	1.6
15	10	25.5	1.41	4.3			15.6	3.2	-	-	2.0	2.2
16	20	47.0 ^m	1.28	6.0	CBs	Glaser-Hay coupling ^[51]	26.1 ^m	4.3	3.5	-	2.5	2.7

Chapter 3. Scaling laws for apparent molecular weight, apparent polydispersity index, hydrodynamic radius and intrinsic viscosity in SCNPs

17	25	236.5 ^m	1.37	14.9	CBs	Michael addition ^[32]	117.5 ^m	10.1	7.7	11.5 [*]	4.3	4.6
18	10	24.6 ^m	1.17	4.2	DCBs	Anthracene dimerization ^[52]	-	-	3.4	7.5-10 × 3.5-5 [*]	2.0	2.2
19	20	20.2 ^m	1.14	3.7			-	-	2.9	-	1.9	2.0
20	31	25.4 ^m	1.05	4.3	DCBs	Enamine chemistry ^[53]	-	-	2.7	-	2.0	2.2
21	30	31.1 ^m	1.06	4.8			-	-	2.9	-	2.2	2.3
22	26	43.4 ^m	1.05	5.8			-	-	3.4	-	2.4	2.6
23	30	242.2 ^m	1.30	15.1			-	-	7.1	-	4.3	4.6
24	6	131.0	1.25	10.7	NCBs	Benzamide dimerization ^[54]	-	-	(12.0)	20-90 ^{**}	3.5	3.9
25	11	27.9	1.12	4.5	NCBs	Ureido-pyrimidinone dimerization ^[44]	23.8	4.1	(5.0)	-	2.1	2.3
26	17	97.1	1.43	9.0			87.7	9.0	(11.8)	-	3.2	3.4
27	17	28.0	1.16	4.5			25.6	4.3	-	12.5-15 ^{**}	2.1	2.3

^a Relative amount of functional groups in the PMMA linear precursor. ^b Weight average molecular weight referred to PS standards. ^c Polydispersity index referred to PS standards. ^d For the precursors: $R_H^{SEC}(nm) = 1.44 \cdot 10^{-2} M_w^{0.561}$,^[19] for the PS-SCNPs: $R_H^{SEC}(nm) = 1.44 \cdot 10^{-2} (M_{app})^{0.561}$.^[45] ^e CBs = Covalent bonds. DCBs = Dynamic covalent bonds. NCBs = Non-covalent bonds. ^f M_{app} of the SCNPs referred to PS standards.^[45] ^g Data from DLS measurements. In parentheses: data in which $R_H^{DLS}(SCNP) > R_H^{SEC}(\text{precursor})$. ^h Data of average SCNP radius as determined from TEM (*) or AFM (**). ⁱ Compact PMMA globules: $R_H^{\phi=1} = [3M_w / (4\pi\phi\rho N_A)]^{1/3}$ with $\phi = 1$ and $\rho = 1.2 \text{ g/cm}^3$.^[46] ^j Partially swollen PMMA globules (solvent content: 20%): $R_H^{\phi=0.8} = [3M_w / (4\pi\phi\rho N_A)]^{1/3}$ with $\phi = 0.8$.^[46] ^k As determined from small angle X-ray scattering measurements. ^l CuAAC = Copper(I)-catalyzed azide alkyne cycloaddition. ^m Estimated from $M_w^{PS} = M_w^{PMMA} [\eta]^{PMMA} / [\eta]^{PS}$ with $[\eta]^{PMMA} = 10.4 \cdot 10^{-3} (M_w^{PMMA})^{0.697}$ and $[\eta]^{PS} = 9.96 \cdot 10^{-3} (M_w^{PS})^{0.734}$.

Table 3.5. Comparison of the size (R_H^{SEC} , R_H^{DLS} , $R_H^{TEM/AFM}$) of SCNPs of different chemical structure with the size of compact ($R_H^{\phi=1}$) and swollen ($R_H^{\phi=0.8}$) globules.

Precursors						SCNPs				Globules	
Type	x (mol %) ^a	M_w^b (kDa)	PDI ^c	R_H^{SEC} (nm) ^d	Type ^e / Crosslinking Chemistry	M_{app} (kDa) ^f	R_H^{SEC} (nm) ^d	R_H^{DLS} (nm) ^g	$R_H^{TEM/AFM}$ (nm) ^h	$R_H^{\phi=1}$ (nm) ⁱ	$R_H^{\phi=0.8}$ (nm) ^j
Poly(methyl acrylate), PMA	15	26.8	1.27	4.4	CBs / Photo-Bergman cyclization ^[55]	20.1	3.7	-	-	2.2	2.3
	10	725.0	1.34	27.9	CBs / Bergman cyclization ^[56]	282.3	16.5	-	-	6.5	7.0
	10	104.2	1.41	9.4		68.5	7.4	-	-	3.4	3.7
	27	23.1	1.25	4.0		11.1	2.7	-	-	2.1	2.2
	15	90.0	1.84	8.7	NCBs / UPy dimerization ^[44]	64.5	7.2	(9.9)	-	3.2	3.5
Poly(ethyl acrylate), PEA	20	19.8	1.26	3.7	CBs / Photo-Bergman cyclization ^[55]	13.0	2.9	-	-	2.0	2.1
Poly(<i>n</i> -butyl acrylate), PnBA	20	21.7	1.23	3.9	CBs / Photo-Bergman cyclization ^[55]	17.1	3.4	-	5**	2.0	2.2
	5	74.5	1.10	7.8	CBs / Benzocyclobutane dimerization ^[2]	58.1	6.8	-	-	3.0	3.3
	10	77.5	1.12	8.0		45.7	5.9	-	-	3.1	3.3
	15	75.0	1.09	7.8		33.5	5.0	-	-	3.0	3.3
	20	73.0	1.09	7.7		27.8	4.5	-	-	3.0	3.2
	21	55.0	1.3	6.6	CBs / CuAAC click chemistry ^{k[37]}	19.5	3.7	4.0	-	2.7	3.0
Poly(<i>t</i> -butyl acrylate), PtBA	17	27.9	1.20	4.5	CBs / Photo-Bergman cyclization ^[55]	18.0	3.5	-	-	2.2	2.4
	21	34.0	1.17	5.0	CBs / CuAAC click chemistry ^{k[37]}	21.6	3.9	3.5	1.8**	2.3	2.5

Chapter 3. Scaling laws for apparent molecular weight, apparent polydispersity index, hydrodynamic radius and intrinsic viscosity in SCNPs

Poly(benzyl acrylate), PBzA	5	68.0	1.28	7.4	CBs / <i>o</i> -Quinodimethane chemistry ^[8]	42.0	5.6	-	3.3*	2.9	3.2
	25	31.8	1.05	4.8	CBs / Bergman cyclization ^[57]	21.4	3.9	-	-	2.3	2.5
	10	67.0	1.07	7.3		46.4	6.0	-	-	2.9	3.2
	10	141.7	1.23	11.2		83.2	8.3	-	-	3.8	4.1
Poly(propargyl methacrylate / methyl methacrylate), PPgMMA	10	87.9	1.54	8.5	NCBs / UPy dimerization ^[16]	71.8	7.6	-	30-35**	3.2	3.5
	20	82.0	1.40	8.2		62.0	7.0	-	20-25**	3.1	3.4
Poly(cyclohexyl methacrylate), PCHMA	27	2 641.0	1.55	57.7	CBs / Ring opening polymerization ^[31]	1 304.0	38.8	20.0	-	9.9	10.8
Poly(benzyl methacrylate), PBzMA	35	1 912.0	1.39	48.1	CBs / Ring opening polymerization ^[31]	610.0	25.3	17.5	20* 18**	8.9	9.7
	31	2 330.0	1.68	53.8		690.0	27.2	19.0		9.6	10.3
Poly(isobornyl methacrylate), PIBMA	8	32.6	1.16	4.9	NCBs / Orthogonal interactions ^[58]	30.7	4.7	-	-	2.3	2.5
	7	66.3	1.33	7.3		58.4	6.8	(14.4) ^m	-	2.9	3.2
	8	181.0	1.46	12.8		157.3	11.9	-	20-65**	4.1	4.4
Poly(<i>N,N</i> - dimethylaminoethyl methacrylate), PDMAEMA	7.5	127.0	1.15	10.5	CBs / Coumarin dimerization ^[59]	86.3	8.5	-	-	3.6	3.9
	13	120.0	1.15	10.2		85.1	8.4	-	THF: 15-30* H ₂ O: 5-10*	3.6	3.8
Poly(acrylic acid), PAA	5	75.0	1.21	7.8	CBs / Benzocyclobutane dimerization ^[60]	-	-	3.7	2.2*	3.0	3.3

Poly(<i>N</i> -isopropyl acrylamide), PNIPAM	10	50.7	1.30	6.3	CBs / CuAAC click chemistry ^{k[37]}	-	-	5.0	-	2.7	2.9
Poly(4- <i>N</i> -Boc-vinylaniline), PBVA	33	28.5	1.50	4.5	CBs / Radical coupling ^[5]	17.3	3.4	(10.8)	-	2.2	2.4
	50	34.9	1.66	5.1		15.7	3.3	(16.9)	-	2.4	2.5
Poly(ϵ -caprolactone), PCL	7	10.7	1.08	2.6	CBs / Radical coupling ^[3]	9.9	2.5	(3.8)	-	1.6	1.7
	15	20.5	1.35	3.8		15.7	3.3	(4.3)	-	2.0	2.1
	12	14.8	1.25	3.1	CBs / Bergman cyclization ^[50]	8.5	2.3	-	-	1.8	1.9
Poly(carbonate), PC	38	64.9	1.20	7.2	CBs / Vinyl cross-metathesis ^[7]	37.5	5.3	-	6-12 ^{**}	2.9	3.1
Poly(3,4-propylenedioxythiophene bearing styrene), PPDOTS	100	12.7	1.11	2.9	CBs / oxidative polymerization ^[61]	9.9	2.5	-	8-9 [*]	1.7	1.8
Poly(norbornene), PNOR	14	72.0	1.26	7.6	CBs / Orthogonal chemistries ^[44,62]	74.6	7.8	6.3	-	3.0	3.2
	20	54.0 ^l	1.19	6.5 ^l		-	-	4.3	-	2.7	2.9
	10	320.9	1.55	17.7	NCBs / UPy dimerization ^[15]	235.6	14.9	-	10 ^{**}	4.9	5.3
	30	28.0 ^l	1.22	4.5 ^l	DCBs / Disulphide formation ^[63]	-	-	3.9	6-11 [*]	2.2	2.4
Poly(1,5-cyclooctadiene), PCOD	10	33.5	1.34	5.0	NCBs / Metallation ^[64]	-	-	(6.1)	10 [*]	2.3	2.5

^a Relative amount of functional groups in the precursor. ^b Weight average molecular weight referred to PS standards. ^c Polydispersity index referred to PS standards. ^d For the polymer precursors: $R_H^{SEC}(\text{nm}) = 1.44 \cdot 10^{-2} M_w^{0.561, [19]}$ for the SCNPs: $R_H^{SEC}(\text{nm}) = 1.44 \cdot 10^{-2} (M_{app})^{0.561}$. ^e CBs = Covalent bonds. DCBs = Dynamic covalent bonds. NCBs = Non-covalent bonds. ^f M_{app} of the SCNP referred to PS standards. ^g Data from DLS measurements. In parentheses: data showing $R_H^{DLS}(\text{SCNP}) > R_H^{SEC}(\text{precursor})$. ^h Data of average SCNP radius as determined from TEM (*) or AFM (**). ⁱ Compact globules: $R_H^{\phi=1} = [3M_w / (4\pi\phi\rho N_A)]^{1/3}$ with $\phi = 1$ and $\rho = 1.05 \text{ g/cm}^3$. ^j Partially swollen globules (solvent content: 20%): $R_H^{\phi=0.8} = [3M_w / (4\pi\phi\rho N_A)]^{1/3}$ with $\phi = 0.8$ and $\rho = 1.05 \text{ g/cm}^3$. ^k CuAAC = Copper(I)-catalyzed azide alkyne cycloaddition. ^l Equivalent PS M_w giving the experimental R_H^{SEC} values. ^m Experimental value of radius of gyration, R_g^{SAXS} , as determined by small angle X-ray scattering.

3.3.2. Conclusions

This second part of the chapter has analyzed the hydrodynamic radii for different SCNPs systems, providing an overall view of the morphology of current SCNPs produced by methods described in the literature.

In general, the hydrodynamic radius (R_H) of SCNPs in solution was larger than for compact ($R_H^{\phi=1}$) or partially swollen globules ($R_H^{\phi=0.8}$) of the same nature and molar mass, revealing the sparse morphology of the nanoparticles. In order to quantify how far SCNPs are from the globular state, the scaling exponent ν was analyzed through $R_H \propto M_w^\nu$ scaling law. This scaling exponent ν showed some dependence on the chemical nature of the linear polymer employed for the synthesis of SCNPs and also on the amount of reactive cross-linker (X-linker) in the polymer precursor. Concerning the amount of cross-linker, a plateau was assumed above 30 mol% of cross-linker, which means that an increase in the cross-linker amount is not efficient for obtaining more compact morphologies.

Although there was some changes in ν depending on the chemical nature of the nanoparticles and the amount of cross-linker, the values obtained were close to $\nu \approx 0.5$. These results are consistent with those obtained in the first part of the chapter, where the values obtained for $\alpha = 3\nu - 1$ for SCNPs of different chemical natures, were around 0.5. This agreement corroborates that the techniques used in the literature produce SCNPs with morphologies resembling those of chain in θ -solvent or intrinsically disordered proteins ($\nu \approx 0.5$, $\alpha \approx 0.5$), and that are far from the globular state ($\nu = 0.33$, $\alpha = 0$). Therefore, new synthesis routes need to be developed in order to produce SCNPs with well-defined compact morphologies.

3.4. SCNPs vs. star, hyperbranched and dendrimeric polymers: Effect of nanoscopic architecture on the flow properties of diluted solutions

3.4.1. Introduction and objectives

The intrinsic viscosity, $[\eta]$, a measure of a polymer's ability to increase the viscosity of a solvent,^[47,66] is one of the most fundamental properties of polymers in dilute solution. It is defined as the limit of the reduced viscosity as the polymer concentration approaches to zero: $[\eta] = \lim_{c \rightarrow 0} (\eta_{sp}/c)$.

The flow properties of dilute solutions of polymers of different architectures, such as linear, star, hyperbranched, dendrimeric polymers, etc., have been the subject of numerous studies. However, no systematic analysis has been carried out for the case of single-chain polymer nanoparticles (SCNPs).

The relation between intrinsic viscosity and molecular weight is different depending on the architecture of the polymer. In the case of linear polymers, as was said in the first part of the chapter, they follow Mark-Houwink-Sakurada's (MHS) equation: $[\eta] = K_{\eta} M^{\alpha}$, where K_{η} and $\alpha = 3\nu - 1$ are constants for a given polymer-solvent pair.^[47] The exponent α is a constant whose value depends on the macromolecular architecture and the solvent quality. Linear polymers in θ -solvent have a value of $\nu = 0.5$, and therefore $\alpha = 0.5$, whereas in ideal good solvent conditions^[47,66] $\nu_F \approx 0.59$ and therefore $\alpha \approx 0.76$.

Star polymers with different arm number also follow the MHS equation. For this particular polymer architecture, the value of the exponent α in the MHS equation is very similar to that displayed by linear chains of the same chemical nature,^[67-69] and must be identical in the limit of large molecular weight.^[47] However, for a fixed value of M , the value of $[\eta]$ decreases upon increasing the arm number f , because of the inverse dependence of the star size on f . This behavior has been observed for star polymers both in θ -solvent^[70,71] and good solvent conditions.^[70,72]

Hyperbranched polymers with long spacer length also follow the MHS equation^[73] indicating that these chains with such particular topology are fractal objects.^[47,73] For these systems, the exponent α in the MHS equation takes values below 0.5 (e.g., 0.39 for hyperbranched PS chains with long spacers) and vary with the molecular weight of the spacer.^[73] For fixed M , $[\eta]$ increases on increasing the spacer length. For

comparison, hyperbranched polymers with short spacer length show values of the exponent α in the range of 0.3 – 0.5.^[74]

Dendrimeric polymers, on the contrary, do not follow the MHS equation.^[75,76] In fact, dendrimeric polymers usually show a maximum (i.e., bell-shaped curve) in the classical $[\eta]$ vs. generation number (G) plot. This behavior has been explained on the basis of the Einstein's result^[77] for hard spheres, $[\eta] \propto V_H/M$, where V_H is the hydrodynamic volume. The molecular weight M , in dendrimeric polymers with a branch multiplicity B increases exponentially with G according to $M \propto B^G$, whereas the hydrodynamic volume V_H , grows with G as $V_H \propto G^3$. Therefore, the intrinsic viscosity scales as $[\eta] \propto G^3/B^G$ and shows a maximum at $G = 3/\ln(B)$.^[78, 79]

SCNPs in solution, according to recent SANS and SAXS experiments as well as complementary MD simulations, behave as fractal objects^[80], so they also follow Mark-Houwink-Sakurada equation.

So, this part of the chapter has different objectives. First, to obtain a simple scaling power-law between intrinsic viscosity $[\eta]$ of SCNPs and molecular weight M as a function of the amount of cross-linker groups in the polymer precursor. Second, to compare the values of $[\eta]$ derived from this expression to experimental data available for SCNPs of different chemical nature. Finally, a comparison is performed between $[\eta]$ values of SCNPs and low-functionality star, hyperbranched and dendrimeric polymers of the same chemical nature and molecular weight in order to unravel the effect of the nanoscopic architecture on the flow properties of diluted solutions of polymers with different architectures.

3.4.2. Obtaining of a scaling power-law between $[\eta]$ and M

As mentioned in the second part of this chapter, MD simulations^[33,34] and scattering experiments^[30-34,80] revealed that SCNPs in solution adopt open, sparse morphologies resembling those of intrinsically disordered proteins with locally compact portions connected by flexible segments. This tendency has been confirmed in the previous part by compiling literature data for hydrodynamic radii of SCNPs,^[80] which are consistent with scaling exponents $\nu \sim 1/2$, similar to those of chains in θ -solvent or intrinsically disordered proteins, and rather different from those of globular proteins, $\nu \sim 1/3$. The value of the exponent ν , shows some dependence on the amount of reactive X-linker functional groups in the polymer precursor. This behavior is better observed in Figure 3.8, which shows the ratio of the value of the exponent ν for PMMA-SCNPs and PS-SCNPs to that of the corresponding precursor, as a function of the X-linker amount in

polymer precursor. The exponents have been obtained by fitting SEC results to a power-law $R_H = K_H M^\nu$ (previous part). This tendency was corroborated by MD simulations from which scaling law of $\langle R_g^2 \rangle^{1/2} \propto M^\nu$ have been observed,^[33,34] by assuming that the dependences of $\langle R_g^2 \rangle^{1/2}$ and R_H on M are similar. A good agreement is observed between experimental and MD simulation data, supporting that the behavior illustrated in Figure 3.8 is a general behavior for SCNPs.

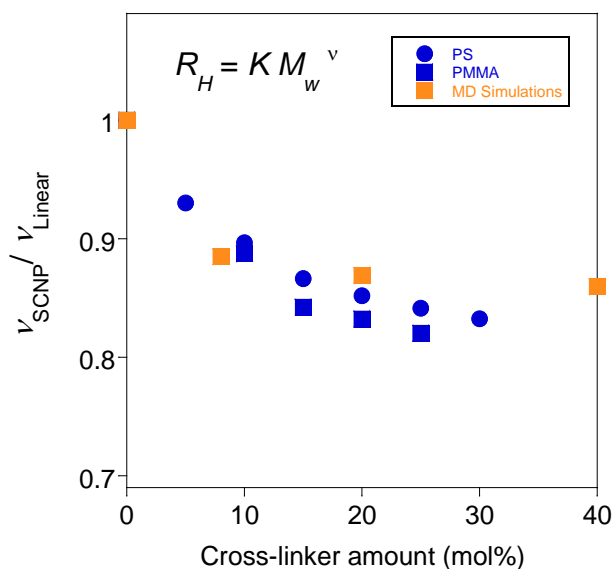


Figure 3.8. Evolution of the ratio of the exponent ν in the power-law $R_H = K_H M^\nu$ of SCNPs to the corresponding value of the precursor, as a function of the X-linker amount in the precursors for PS-SCNPs (blue circles) and PMMA-SCNPs (blue squares). Data from MD simulations^[33] are obtained from $\langle R_g^2 \rangle^{1/2} \propto M^\nu$ fits, and are also shown for comparison (orange squares).

In the previous part, in Figures 3.6a and 3.6c, the analysis data for the SCNPs provided the values of K_H and ν in the scaling law $R_H = K_H M^\nu$. Using these experimental values of K_H and ν , it is possible to obtain the parameters of K_η and α , which relate the molecular weight M with intrinsic viscosity $[\eta]$ through MHS equation $[\eta] = K_\eta M^\alpha$. For that, and knowing that $K_H = (3K_\eta/10\pi N_A)^{1/3}$ from the first part of the chapter, the value of K_η is obtained. On the other hand, taking into account that $\alpha = 3\nu - 1$, replacing these values in the MHS equation, the following expression is obtained:

$$[\eta] = \left(\frac{10\pi}{3}\right) N_A K_H^3 M^{3\nu-1}$$

Where $K_\eta = (10\pi/3)N_A K_H^3$ and $\alpha = 3\nu - 1$. The predicted values of K_η and α for PMMA-SCNPs and PS-SCNPs as a function of the amount of reactive cross-linker in the precursor, are summarized in Table 3.6. In what follows, the values of the intrinsic viscosity calculated by this simple approach are going to be denoted as $[\eta]_{\text{calc}}$, to distinguish them from the experimental data directly measured by viscosimetry, $[\eta]_{\text{exp}}$.

Table 3.6. Values of R_H and $[\eta]_{\text{calc}}$ scaling power-laws for PMMA-SCNPs and PS-SCNPs as a function of the X-linker amount in the polymer precursor.^a

Entry	SCNP type	X-linker amount (mol%)	$R_H = K_H M^\nu$		$[\eta]_{\text{calc}} = K_\eta M^\alpha$	
			K_H	ν	K_η	α
1	PMMA	10	$1.67 \cdot 10^{-2}$	0.52	$2.94 \cdot 10^{-2}$	0.56
2		15	$1.93 \cdot 10^{-2}$	0.50	$4.53 \cdot 10^{-2}$	0.50
3		20	$1.94 \cdot 10^{-2}$	0.50	$4.61 \cdot 10^{-2}$	0.50
4		25	$2.01 \cdot 10^{-2}$	0.49	$5.12 \cdot 10^{-2}$	0.47
5	PS	10	$1.92 \cdot 10^{-2}$	0.51	$4.46 \cdot 10^{-2}$	0.53
6		15	$2.04 \cdot 10^{-2}$	0.49	$5.35 \cdot 10^{-2}$	0.47
7		20	$2.12 \cdot 10^{-2}$	0.48	$6.01 \cdot 10^{-2}$	0.44
8		25	$2.18 \cdot 10^{-2}$	0.47	$6.53 \cdot 10^{-2}$	0.41

^a R_H and M data obtained from SEC measurements (previous part).

3.4.3. Comparison between $[\eta]_{\text{calc}}$ and $[\eta]_{\text{exp}}$ for SCNPs of different chemical nature

Figure 3.9 shows a comparison between theoretical, $[\eta]_{\text{calc}}$, and experimental data,^[13,52,63] $[\eta]_{\text{exp}}$, of several SCNPs of different chemical nature. There is a reasonable agreement between $[\eta]_{\text{exp}}$ and $[\eta]_{\text{calc}}$ data with an average standard deviation between both data sets of 12 %.

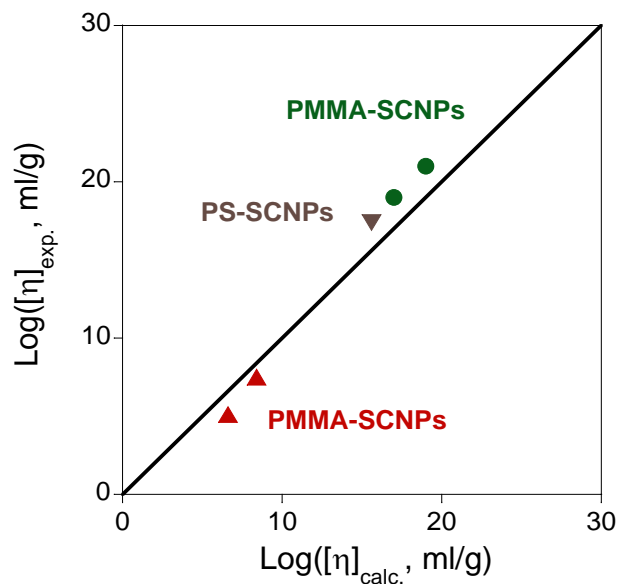


Figure 3.9. Comparison of $[\eta]_{exp}^{[13,52,63]}$ vs. $[\eta]_{calc}$ for SCNPs of different chemical nature and molecular weight (see Table 3.6). The line corresponds to the case $[\eta]_{exp} = [\eta]_{calc}$.

The agreement between $[\eta]_{exp}$ and $[\eta]_{calc}$ is expected to be improved significantly by using more elaborated theoretical approaches, such as the recently developed partially permeable sphere model.^[81,82] However, the use of this simple model treating SCNPs in solution as spheres of effective hydrodynamic radius R_H , provides clear explanation to the observation by Beck *et al.*^[13] In that work, for linear copolymers of 100 kDa and 150 kDa, a higher value of $[\eta]$ was observed for the polymer of 150 kDa. In direct contrast, the corresponding nanoparticles not only displayed much lower $[\eta]$, but there was no significant difference between the two samples even though the molecular weight differ by 50% (Figure 3.10).

The experimental intrinsic viscosity was determined as the values of the reduced viscosity in the limit of zero concentration, $c = 0$, by fitting the data to the Huggins equation^[50,66] $\eta_{red} = [\eta]_{exp} + k([\eta]_{exp})^2 c$. It was observed that $[\eta]_{calc}$ follows the same trend (solid lines). For the case of SCNPs, applying the simple scaling-law $[\eta]_{calc} = K_\eta M^\alpha$ in the Huggins equation $\eta_{red} = [\eta]_{calc} + k([\eta]_{calc})^2 c$, with a typical factor^[83] $k = 1$, a similar trend is observed (orange lines). The values of K_η and α are taken from entry 2 of Table 3.6. For the case of polymer precursors, $[\eta]_{calc} = 10.4 \cdot 10^{-3} M^{0.697}$ equation^[19] was used (blue lines).

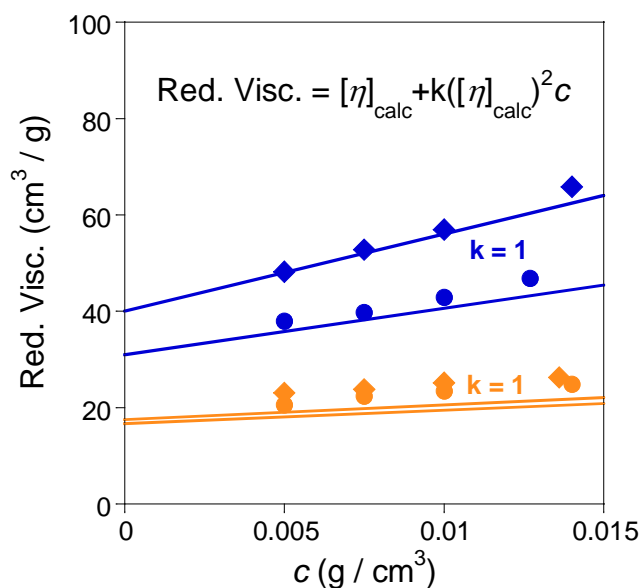


Figure 3.10. Reduced viscosity as a function of the concentration for PMMA precursors with the same X-linker fraction but different molecular weights (150 kDa, blue diamonds; 100 kDa, blue circles) and the corresponding SCNPs (150 KDa, orange diamonds; 100 kDa, orange circles). The experimental viscosimetry data were obtained from Figure 4 of reference 13. Orange lines correspond to $\eta_{red} = [\eta]_{calc} + k([\eta]_{calc})^2c$, where $[\eta]_{calc} = K_{\eta}M^{\alpha}$, and $k = 1^{[83]}$. K_{η} and α are from entry 2 of Table 3.6. Blue lines correspond to $[\eta]_{calc} = 10.4 \cdot 10^{-3} M^{0.697}$.^[19]

3.4.4. Comparison of the intrinsic viscosity of SCNPs vs. star, hyperbranched and dendrimeric polymers

It is very interesting to compare the $[\eta]$ values of SCNPs with the $[\eta]$ values of star, hyperbranched and dendrimeric polymers of exactly the same nature and molecular weight. This comparison helps to clarify the effect of the complex topology of SCNPs on the flow properties of their dilute solutions.

The different plots in Figure 3.11 compare experimental results for $[\eta]$ of SCNPs (blue symbols) and low-functionality stars, hyperbranched and dendrimers (orange symbols) with the same chemical structure. Top plots (a, c and e) show results for PMMA-based systems. Bottom plots (b, d and f) show results for PS-based systems. Blue symbols in all plots correspond to the SCNPs. Orange symbols correspond to star (plots a and b), hyperbranched (plots c and d) and dendrimeric (plots e and f) polymers. The blue lines represent the theoretical intrinsic viscosities $[\eta]_{calc}$ for SCNPs, by using values of K_{η} and α from Table 3.6. Specifically, for the PMMA-SCNPs (top graphs) entries 1 (solid), 2 (dashed) and 4 (dotted) of Table 3.6 were used, whereas for PS-SCNPs (bottom)

entries 5 (solid) and 7 (dashed). The green lines are the experimental power-laws for intrinsic viscosities obtained from viscosimetry measurements of the corresponding linear polymers. So, the green lines in top graphs correspond to linear PMMA chains in THF: $[\eta]_{\text{exp}} = 10.4 \cdot 10^{-3} M^{0.697}$,^[19] while the green lines in bottom images correspond to the linear PS chains in THF: $[\eta]_{\text{exp}} = 9.96 \cdot 10^{-3} M^{0.734}$.^[84] Orange lines in all plots are linear fits (for stars and hyperbranched) or parabolic fits (for dendrimers) of the orange symbols, and are included for comparison with the theoretical curves of the SCNPs (blue lines).

Figure 3.11a provides a comparison of the $[\eta]$ vs. M behavior of PMMA-SCNPs^[13,52] and 6-arm PMMA stars.^[85] It was observed that at any given value of M the SCNPs display significantly lower values of $[\eta]$ when compared to 6-arm PMMA stars of the same mass (e.g., $M \approx 100$ kDa: $[\eta]_{\text{exp}}(\text{PMMA-SCNPs}) \approx 18$ mL/g^[13] vs. $[\eta]_{\text{exp}}(\text{6-arm PMMA stars}) \approx 32$ mL/g^[85]). Upon increasing the amount of X-linker in the SCNP precursor from 10 mol% (solid blue line) to 15 mol% (blue dashed line) and to 25 mol% (blue dotted line), a progressive decrease in the value of $[\eta]$ is predicted. A similar behavior is expected for PS-SCNPs when compared to 6-arm PS stars,^[71] as illustrated in Figure 3.11b. Once again, a significant reduction in $[\eta]$ is predicted upon increasing the amount of X-linker in the polymer precursor from 10 mol% (solid line) to 20 mol% (dashed line) although, to the best of our knowledge, no experimental data are available to validate this trend.

Figure 3.11c compares the $[\eta]$ vs. M behavior of PMMA-SCNPs and hyperbranched PMMA chains.^[86] At low molecular weight SCNPs have lower values of $[\eta]$ when compared to those of PMMA hyperbranched chains of equivalent M (e.g., for $M = 25$ kDa, $[\eta]_{\text{exp}}(\text{PMMA-SCNPs}) \approx 8$ mL/g^[52] vs. $[\eta]_{\text{exp}}(\text{hyperbranched PMMA chains}) \approx 12$ mL/g^[86]). Conversely, even if the value of the α exponent is lower in the MHS equation for hyperbranched PMMA chains when compared to SCNPs, due to the higher value of K_{η} , the opposite behavior is expected at very high values of M . Once again, a similar behavior is predicted for PS-SCNPs although in this case the molecular weight at which the MHS equations of hyperbranched PS chains^[73] and SCNPs (10 mol% X-linker in the polymer precursor) cross each other is $> 10^6$ Da (Figure 3.11d).

The behavior of dendrimeric polymers in dilute solution is peculiar since a maximum in the $[\eta]$ vs. M plot is observed for these nano-objects (Figure 3.11e and 3.11f).^[87,88] As a consequence, even if SCNPs of relatively low molecular weight have values of $[\eta]$ similar or even lower than those of dendrimeric polymers of equivalent M , upon increasing the molecular weight this trend is clearly reversed, as illustrated in Figure

3.11e and 3.11f. In particular, the specific value of M at which the $[\eta]$ -curve of the dendrimeric polymer crosses the line of the SCNP strongly depends (varying even an order of magnitude) on the amount of X-linker in the SCNP precursor.

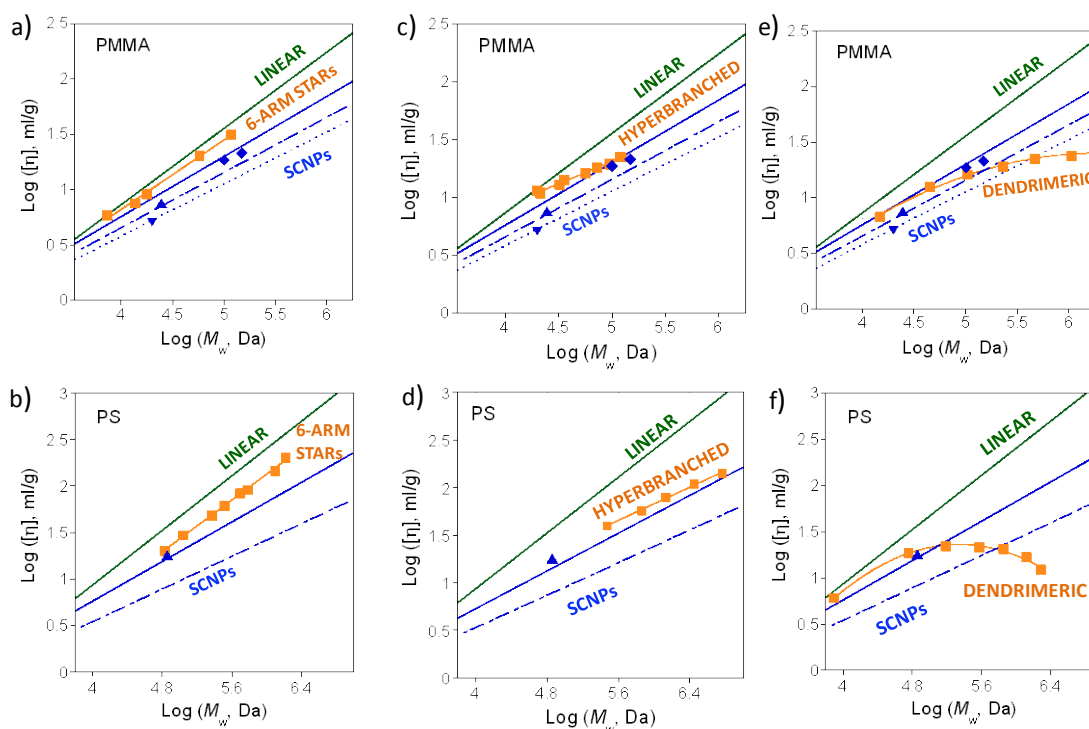


Figure 3.11. $[\eta]$ vs. M behavior of SCNPs, star, hyperbranched and dendrimeric polymers of the same chemical nature. Top plots (a, c and e) are for PMMA-based systems. Bottom plots (b, d and f) are for PS-based systems. Symbols in all plots are experimental data obtained from the following references: i) PMMA-SCNPs (diamonds; 15 mol% cross-linker,^[13] triangles; 10 mol% cross-linker^[52] and inverted triangles; 20 mol% cross-linker^[53]). ii) PS-SCNPs, 10 mol% cross-linker.^[71] iii) PMMA stars and hyperbranched.^[85] iv) PMMA dendrimers.^[86] v) PS stars.^[71] vi) PS hyperbranched.^[73] vii) PS dendrimeric.^[87] The blue lines represent the $[\eta]_{calc}$ for SCNPs, by using values of K_η and α from Table 3.6. Specifically, for the PMMA-SCNPs entries 1 (solid), 2 (dashed) and 4 (dotted) were used, whereas for PS-SCNPs entries 5 (solid) and 7 (dashed). Green lines in top plots correspond to linear PMMA chains in THF: $[\eta]_{exp} = 10.4 \cdot 10^{-3} M^{0.697}$.^[19] Green lines in bottom plots correspond to linear PS chains in THF: $[\eta]_{exp} = 9.96 \cdot 10^{-3} M^{0.734}$.^[84] Orange lines in all plots are linear fits (for stars and hyperbranched) or parabolic fits (for dendrimers) of the orange symbols.

3.4.5. Conclusions

In this part of the chapter, a simple scaling power-law between the intrinsic viscosity $[\eta]$ and molecular weight M has been derived for SCNPs as a function of the amount of reactive cross-linker (X-linker) functional groups in the polymer precursor. The reasonable agreement found between $[\eta]_{exp}$ and $[\eta]_{calc}$ data supports this simple model.

The underlying microscopic dynamics, as for other polymer architectures, is no more than Zimm-like dynamics. The observed differences between $[\eta]$ in the SCNPs and other architectures have a *static* origin: the specific dependence of the molecular size on the molecular weight, through scaling exponents that depend on the molecular architecture and/or fraction of X-linkers.

As a consequence of their complex nanoscopic architecture, the intrinsic viscosities of SCNPs are systematically smaller than those of linear chains and low-functionality stars. However, when compared with hyperbranched and dendrimeric polymers, a complex behavior is found, being highly dependent on the molecular weight and amount of X-linker of the SCNP.

3.5. References

1. S. Mori, H. G. Barth, *Size Exclusion Chromatography*, Springer: Berlin, 1999.
2. E. Harth, B. V. Horn, V. Y. Lee, D. S. Germack, C. P. Gonzales, R. D. Miller, C. J. Hawker, *J. Am. Chem. Soc.* **2002**, *124*, 8653.
3. D. Mecerreyes, V. Lee, C. J. Hawker, J. L. Hedrick, A. Wursch, W. Volksen, T. Magbitang, E. Huang, R. D. Miller, *Adv. Mater.* **2001**, *13*, 204.
4. K. S. Park, D. Y. Kim, S. K. Choi, D. H. Suh, *Jpn. J. Appl. Phys.* **2003**, *42*, 3877.
5. J. Jiang, S. Thayumanavan, *Macromolecules* **2005**, *38*, 5886.
6. P. Taranekar, J. Y. Park, D. Patton, T. Fulghum, G. J. Ramon, R. Asvincula, *Adv. Mater.* **2006**, *18*, 2461.
7. A. E. Cherian, F. C. Sun, S. S. Sheiko, G. W. Coates, *J. Am. Chem. Soc.* **2007**, *129*, 11350.
8. T. A. Croce, S. K. Hamilton, M. L. Chen, H. Muchalski, E. Harth, *Macromolecules* **2007**, *40*, 6028.
9. A. Ruiz de Luzuriaga, N. Ormategui, H. J. Grande, I. Odriozola, J. A. Pomposo, I. Loinaz, *Macromol. Rapid Commun.* **2008**, *29*, 1156.
10. G. Njikang, G. Liu, S. A. Curda, *Macromolecules* **2008**, *41*, 5697.
11. J. E. F. Radu, L. Novak, J. F. Hartmann, N. Beheshti, A.-L. Kjoniksen, B. Nystrom, J. Borbely, *Colloid Polym. Sci.* **2008**, *286*, 365.
12. L. Cheng, G. Hou, J. Miao, D. Chen, M. Jiang, L. Zhu, *Macromolecules* **2008**, *41*, 8159.
13. J. B. Beck, K. L. Killops, T. Kang, K. Sivanandan, A. Bayles, M. E. Mackay, K. Wooley, C. J. Hawker, *Macromolecules* **2009**, *42*, 5629.
14. C. T. Adkins, H. Muchalski, E. Harth, *Macromolecules* **2009**, *42*, 5786.
15. E. J. Foster, E. B. Berda, E. W. Meijer, *J. Am. Chem. Soc.* **2009**, *131*, 6964.
16. E. B. Berda, E. J. Foster, E. W. Meijer, *Macromolecules* **2010**, *43*, 1430.
17. I. N. Serdyuk, N. R. Zaccai, J. Zaccai, *Methods in Molecular Biophysics: Structure, Dynamics, Function*; Cambridge University Press: New York, **2007**.
18. J. E. Mark, *Physical Properties of Polymers Handbook*; Springer: Berlin, **2007**.
19. L. J. Fetters, N. Hadjichristidis, J. S. Linder, J. W. Mays, *J. Phys. Chem. Ref. Data* **1994**, *23*, 619.
20. P. J. Flory, *Principles of Polymer Chemistry*; Cornell University Press: Ithaca, New York, **1953**.

21. J. Brandrup, E. H. Immergut, *Polymer Handbook*, 3rd ed.; Wiley: New York, **1989**.
22. G. Hild, C. Strazielle, P. Rempp, *Eur. Polym. J.* **1983**, *19*, 721.
23. S. S. Jang, T. Cagin, W. A. Goddard, *J. Chem. Phys.* **2003**, *119*, 1843.
24. Y. J. Chen, J. Li, N. Hadjichristidis, J. M. Mays, *Polym. Bull.* **1993**, *30*, 575.
25. M. Glassner, J. P. Blinco, C. Barner-Kowollik, *Macromol. Rapid Commun.* **2011**, *32*, 724.
26. J. Aitchison, J. A. C. Brown, *The Log-normal Distribution*; Cambridge University Press: New York, **1957**.
27. J. W. Liu, M. E. Mackay, P. M. Duxbury, *Macromolecules* **2009**, *42*, 8534.
28. A. Sanchez-Sanchez, J. A. Pomposo, *Part. Part. Syst. Charact.* **2014**, *31*, 11.
29. A. Sanchez-Sanchez, I. Perez-Baena, J. A. Pomposo, *Molecules* **2013**, *18*, 3339.
30. A. Sanchez-Sanchez, S. Akbari, A. Etxeberria, A. Arbe, A. J. Moreno, J. Colmenero, J. A. Pomposo, *ACS Macro Lett.* **2013**, *2*, 491.
31. I. Perez-Baena, F. Barroso-Bujans, U. Gasser, A. Arbe, A. J. Moreno, J. Colmenero, J. A. Pomposo, *ACS Macro Lett.* **2013**, *2*, 775.
32. A. Sanchez-Sanchez, S. Akbari, A. J. Moreno, F. Lo Verso, A. Arbe, J. Colmenero, J. A. Pomposo, *Macromol. Rapid Commun.* **2013**, *34*, 1681.
33. A. J. Moreno, F. Lo Verso, A. Sanchez-Sanchez, A. Arbe, J. Colmenero, J. A. Pomposo, *Macromolecules* **2013**, *46*, 9748.
34. F. Lo Verso, J. A. Pomposo, J. Colmenero, A. J. Moreno, *Soft Matter* **2014**, *10*, 4813.
35. V. Receveur-Bréchet, D. Durand, *Curr. Protein Pept. Sci.* **2012**, *13*, 55.
36. P. J. M. Stals, M. A. J. Gillissen, T.F. E. Paffen, T. F. A. de Greef, P. Lindner, E. W. Meijer, A. R. A. Palmans, I. K. Voets, *Macromolecules* **2014**, *47*, 2947.
37. A. Ruiz de Luzuriaga, I. Perez-Baena, S. Montes, I. Loinaz, I. Odriozola, I. García, J. A. Pomposo, *Macromol. Symp.* **2010**, *296*, 303.
38. X. Jiang, H. Pu, P. Wang, *Polymer* **2011**, *52*, 3597.
39. P. Wang, H. Pu, M. Jin, *J. Polym. Sci., Pol. Chem.* **2011**, *49*, 5133.
40. P. Khanjani, I. Perez-Baena, L. Buruaga, J. A. Pomposo, *Macromol. Symp.* **2012**, *321-322*, 145.
41. O. Altintas, J. Willenbacher, K. N. R. Wuest, K. K. Oehlenschlaeger, P. Krolla-Sidenstein, H. Gliemann, C. Barner-Kowollik, *Macromolecules* **2013**, *46*, 8092.

42. C. F. Hansell, A. Lu, J. P. Patterson, R. K. O'Reilly, *Nanoscale* **2014**, *6*, 4102.
43. B. S. Murray, D. A. Fulton, *Macromolecules* **2011**, *44*, 7242.
44. P. J. M. Stals, M. A. J. Gillissen, R. Nicolaÿ, A. R. A. Palmans, E. W. Meijer, *Polym. Chem.* **2013**, *4*, 2584.
45. J. A. Pomposo, I. Perez-Baena, L. Buruaga, A. Alegría, A. J. Moreno, J. , *Macromolecules* **2011**, *44*, 8644.
46. E. E. Gürel, N. Kayaman, B. M. Baysal, F. E. Karasz, *J. Polym. Sci., Pol. Phys.* **1999**, *37*, 2253.
47. M. Rubinstein, R. H. Colby, *Polymer Physics*; Oxford University Press, Inc.: New York, **2003**.
48. D. K. Wilkins, S. B. Grimshaw, V. Receveur, C. M. Dobson, J. A. Jones, L. J. Smith, *Biochemistry* **1999**, *38*, 16424.
49. J. A. Marsh, J. D. Forman-Kay, *Biophys. J.* **2010**, *98*, 2383.
50. B. Zhu, J. Ma, Z. Li, J. Hou, X. Cheng, G. Qian, P. Liu, A. Hu, *J. Mater. Chem.* **2011**, *21*, 2679.
51. A. Sanchez-Sanchez, I. Asenjo-Sanz, L. Buruaga, J. A. Pomposo, *Macromol. Rapid Commun.* **2012**, *33*, 1262.
52. P. G. Frank, B. T. Tuten, A. Prasher, D. Chao, E. B. Berda, *Macromol. Rapid Commun.* **2014**, *35*, 249.
53. A. Sanchez-Sanchez, D. A. Fulton, J. A. Pomposo, *Chem. Commun.* **2014**, *50*, 1871.
54. M. Seo, B. J. Beck, J. M. J. Paulusse, C. J. Hawker, S. Y. Kim, *Macromolecules* **2008**, *41*, 6413.
55. B. Zhu, G. Qian, Y. Xiao, S. Deng, M. Wang, A. Hu, *J. Polym. Sci., Pol. Chem.* **2011**, *49*, 5330.
56. B. Zhu, S. Sun, Y. Wang, S. Deng, G. Qian, M. Wang, A. Hu, *J. Mater. Chem. C* **2013**, *1*, 580.
57. G. Qian, B. Zhu, Y. Wang, S. Deng, A. Hu, *Macromol. Rapid Commun.* **2012**, *33*, 1393.
58. N. Hosono, M. A. Gillisen, Y. Li, S. S. Sheiko, A. R. A. Palmans, E. W. Meijer, *J. Am. Chem. Soc.* **2012**, *135*, 501.
59. J. He, L. Tremblay, S. Lacelle, Y. Zhao, *Soft Matter* **2011**, *7*, 2380.
60. J. N. Dobish, S. K. Hamilton, E. Harth, *Polym. Chem.* **2012**, *3*, 857.
61. P. T. Dirlam, H. J. Kim, K. J. Arrington, W. J. Chung, R. Sahoo, L. J. Hill, P. J. Costanzo, P. Theato, K. Char, J. Pyun, *Polym. Chem.* **2013**, *4*, 3765.

62. D. Chao, X. Jia, B. Tuten, C. Wang, E. B. Berda, *Chem. Commun.* **2013**, 49, 4178.
63. B. T. Tuten, D. Chao, C. K. Lyon, E. B. Berda, *Polym. Chem.* **2012**, 3, 3068.
64. S. Mavila, C. E. Diesendruck, S. Linde, S. Amir, R. Shikler, N. G. Lemcoff, *Angew. Chem. Int. Ed.* **2013**, 52, 5767.
65. L. J. Fetters, D. J. Lohse, R. H. Colby, *Physical Properties of Polymer Handbook*, ed. E. J. Mark, Springer **2007**.
66. M. Doi, S. F. Edwards, *The Theory of Polymer Dynamics*; Oxford University Press: Oxford, UK, **1986**.
67. B. H. Zimm, W. H. Stockmayer, *J. Chem. Phys.* **1949**, 17, 1301.
68. B. H. Zimm, R. W. Kilb, *J. Polym. Sci.* **1959**, 37, 19.
69. W. H. Stockmayer, M. Fixman, *Ann. N.Y. Acad. Sci.* **1953**, 57, 334.
70. N. Khasat, R. W. Pennisi, N. Hadjichristidis, L. J. Fetters, *Macromolecules* **1988**, 21, 1100.
71. L. A. Utracki, J. E. L. Roovers, *Macromolecules* **1973**, 6, 366.
72. J. E. L. Roovers, S. Bywater, *Macromolecules* **1974**, 7, 443.
73. L. Li, Y. Lu, L. An, C. Wu, *J. Chem. Phys.* **2013**, 138, 114908.
74. J. M. J. Fréchet and D. A. Tomalia, *Dendrimers and Other Dendritic Polymers*, Ch. 14, Wiley, UK, **2001**.
75. T. H. Mourey, S. R. Turner, M. Rubinstein, J. M. J. Fréchet, C. J. Hawker, K. L. Wooley, *Macromolecules* **1992**, 25, 2401.
76. A. M. Naylor, W. A. Goddard III, G. Keifer, D. A. Tomalia, *J. Am. Chem. Soc.* **1989**, 111, 2339.
77. A. Einstein, *Ann. Phys.* **1911**, 339, 591.
78. J. M. J. Fréchet, *Science* **1994**, 263, 1710.
79. M. Jeong, M. E. Mackay, R. Vestberg, C. J. Hawker, *Macromolecules* **2001**, 34, 4927.
80. J. A. Pomposo, I. Perez-Baena, F. Lo Verso, A. J. Moreno, A. Arbe, J. Colmenero, *ACS Macro Lett.* **2014**, 3, 767.
81. Y. Y. Yu, T. F. Shi, L. J. An, Z.-G. Wang, *EPL*, **2012**, 97, 64003(1-6).
82. Y. Lu, L. An, Z.-G. Wang, *Macromolecules* **2013**, 46, 5731.
83. R. Pamies, J. G. Hernández-Cifre, M. C. López-Martínez, J. G. García de la Torre, *Colloid. Polym. Sci.*, **2008**, 286, 1223.

84. H. L. Wagner, *J. Phys. Chem. Ref. Data* **1987**, *16*, 165.
85. Y. Chen, K. Fuchise, A. Narumi, S. Kawaguchi, T. Satoh, T. Kakuchi, *Macromolecules* **2011**, *44*, 9091.
86. P.F. W. Simon, A. H. E. Müller, T. Pakula, *Macromolecules* **2001**, *34*, 1677.
87. A. Hirao, H.-S. Yoo, *Polym. J.*, **2011**, *43*, 2.
88. R. Matmour, Y. Gnanou, *J. Am. Chem. Soc.* **2008**, *130*, 1350.

**Chapter 4. Endowing SCNPs
With Enzyme-Mimetic Activity**

4.1. Introduction, objectives and methodology

In nature there are perfectly ordered proteins, who have the ability to adopt a stable and well-defined three-dimensional structure, which is directly related to the function of a protein.^[1-3] Although the functions of many proteins are directly related to their perfectly ordered structures, numerous proteins that lack intrinsic globular structure, known as intrinsically disordered proteins (IDPs),^[4-8] also play significant roles in protein functions. IDPs display a highly flexible, random-coil-like conformation under physiological conditions, and in some way, the conformation of SCNPs is similar to them although in a very primitive manner. So, inspired by the disordered structure of IDPs and taking into account that catalysis is a very important process of proteins, a new catalytic system based on single-chain nanoparticles was studied.

Catalysis is a really sophisticated process that has inspired the construction of artificial catalytic nano-objects based on a variety of molecular structures like macrocyclic compounds,^[9] star^[10] and helical polymers,^[11] dendrimers^[12] and micelles.^[13] However, there are not many catalytic systems based on SCNPs. In 2006, Wulff *et al.*, reported for the first time a procedure to obtain molecularly imprinted single molecule nanogels that mimicked the active site of enzymes.^[14] The catalytic sites were imprinted during the polymerization and cross-linking of the nanogel via a diphenyl phosphate template that was then removed from each unimolecular particle. The resulting nano-objects showed Michaelis-Menten kinetics for carbonate hydrolysis, in close analogy to natural enzymes. One of the criteria used for analyzing the efficiency of a catalyst is the turnover frequency (TOF), defined as the number of moles of substrate that a mole of catalyst can convert per unit time.^[15] In this case, the value was very low (TOF = $4.4 \times 10^{-3} \text{ h}^{-1}$).

In 2011, Terashima *et al.* have reported the synthesis of individual amphiphilic polymer nanoparticles in which the apolar core is created around a ruthenium-based catalyst.^[16] The catalyst emerged from the sequential ruthenium-catalyzed living radical polymerization of the different monomers. Due to the presence of ruthenium, the nanoparticles showed transfer hydrogenation in water for hydrophobic reagents, more specifically, the reduction of cyclohexanone to cyclohexanol with a TOF of 11 h^{-1} . More recently, this “hydrophobic cavity” approach was further used with success by Huerta *et al.* for performing L-proline catalyzed aldol reactions (TOF = 2 h^{-1}).^[17]

Considering that there are few catalyst SCNPs, the objective of this chapter is to study the catalytic activity of a new SCNPs system (Figure 4.1). The following issues have been analyzed:

- Use of nanoparticles as catalyst in a reduction reaction. The aim was to compare the TOF with that of other SCNPs catalytic systems previously mentioned.
- Characterization of the polymerase-like catalytic behavior of the SCNPs. The polymerase-like behavior refers to the capacity to polymerize tetrahydrofuran (THF), avoiding confusion with the precise activity of polymerase enzymes to polymerize nucleic acids.^[18]

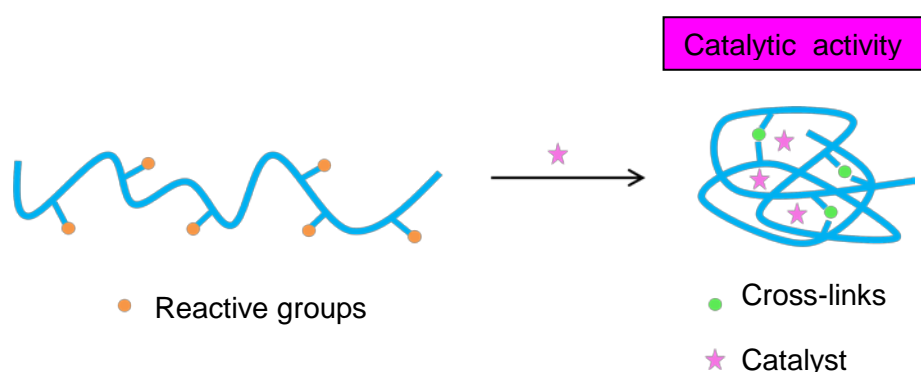


Figure 4.1. Schematic illustration of the synthesis of a catalytic system based on single-chain polymer nanoparticles.

4.2. Experimental part

4.2.1. Reagents

Tris(pentafluorophenyl) borane ($B(C_6F_5)_3$, 95%), benzyl methacrylate (BZMA, 96%), cyclohexyl methacrylate (CHMA, $\geq 97\%$), glycidyl phenyl ether (GPE, 99%), 4,4'-azobis(4-cyanovaleric acid) (ACVA, $\geq 98\%$), 2-cyano-2-propyl benzodithioate (CPBD, $> 97\%$), diphenylethanedione (98%), dimethylphenylsilane ($\geq 98\%$), dichloromethane (CH_2Cl_2 , $\geq 99.5\%$), chloroform ($CHCl_3$, $\geq 99\%$), hexane (95%), dioxane ($\geq 99.8\%$), deuterated chloroform ($CDCl_3$, 99.96 atom% D, containing 0.03 % (v/v) tetramethylsilane, TMS), and deuterated dimethyl sulfoxide ($DMSO-d_6$, 99.96 atom% D) were purchased from Aldrich and used, unless specified, as received. Glycidyl methacrylate (GMA, 97%) was purchased from Acros Organics. Methanol (MeOH, synthesis grade) and tetrahydrofuran (THF, HPLC grade) were purchased from

Scharlab. GMA was purified by distillation before use. BZMA and CHMA were purified by eluting through neutral alumina. GPE was distilled from CaH₂.

4.2.2. Synthesis of high molecular weight P(BzMA-co-GMA) (P1) and P(CHMA-co-GMA) (P3) precursors ($M_w > 1000$ kDa)

P1: For the synthesis of P(BzMA-co-GMA) copolymer, BzMA (1.8 mL, 10.6 mmol), GMA (0.6 mL, 4.4 mmol) and ACVA (473 μ L of a solution 0.67 mg/mL in dioxane) were placed in a dry glass tube with a septum cap, purged by bubbling argon through the reaction mixture for 15 min and then placed in a bath at 80 °C under magnetic stirring. After 40 min of reaction, the resulting copolymer was diluted with 3 mL of THF, recovered by precipitation with MeOH and dried under vacuum. Yield: 0.42 g, 17%. ¹H NMR (500 MHz, CDCl₃): δ (ppm) 7.29 (5H, Ph), 4.93 (2H, -CH₂Ph), 4.19, 3.75 (2H, -OCH₂CH), 3.10 (1H, -OCH₂CH), 2.75, 2.55 (2H, -CHOCH₂), 2.15-1.65 (4H, -CH₂CH(CH₃)), 1.25-0.70 (6H, -CH₂CH(CH₃)). GMA content (¹H NMR): 35 mol%. Weight average molecular weight, M_w (SEC/MALS, dn/dc = 0.136): 1912 kDa. Molecular weight dispersity, PDI: 1.39. R_H (DLS): 20 nm.

P3: For the synthesis of P(CHMA-co-GMA) copolymer, CHMA (1.85 mL, 10.6 mmol), GMA (0.6 mL, 4.4 mmol) and ACVA (473 μ L of a solution 0.67 mg/mL in dioxane) were placed in a dry glass tube with a septum cap, purged by bubbling argon through the reaction mixture for 15 min and then placed in a bath at 80 °C under magnetic stirring. After 40 min of reaction, the resulting copolymer was diluted with 3 mL of THF, recovered by precipitation with MeOH and dried under vacuum. Yield: 0.36 g, 15%. ¹H NMR (500 MHz, CDCl₃): δ (ppm) 4.65 (1H, -OCH), 4.24, 3.84 (2H, -OCH₂CH), 3.20 (1H, -OCH₂CH), 2.83, 2.63 (2H, -CHOCH₂), 2.10-1.65 (4H, -CH₂CH(CH₃)), 1.15-0.85 (6H, -CH₂CH(CH₃)). GMA content (¹H NMR): 27 mol%. Weight average molecular weight, M_w (SEC/MALS, dn/dc = 0.097): 2641 kDa. Molecular weight dispersity, PDI: 1.55. R_H (DLS): 24 nm.

4.2.3. Synthesis of low molecular weight P(BzMA-co-GMA) (P2) and P(CHMA-co-GMA) (P4) precursors ($M_w < 100$ kDa)

P2: For the synthesis of P(BzMA-co-GMA) copolymer, BzMA (1 mL, 5.9 mmol), GMA (334 μ L, 2.4 mmol), ACVA (630 μ L of a solution 2 mg/mL in dioxane) and CPBD (6.2 mg, 0.028 mmol) were placed in a dry glass tube with a septum cap, purged by bubbling argon through the reaction mixture for 15 min and then placed in a bath at 80°C under magnetic stirring. After 2 h of reaction, the resulting copolymer was diluted with 2 mL of THF, recovered by precipitation with MeOH and dried under vacuum.

Yield: 1.12 g, 81%. ^1H NMR (500 MHz, CDCl_3): δ (ppm) 7.30 (5H, Ph), 4.93 (2H, $-\text{CH}_2\text{Ph}$), 4.19, 3.75 (2H, $-\text{OCH}_2\text{CH}$), 3.11 (1H, $-\text{OCH}_2\text{CH}$), 2.75, 2.55 (2H, $-\text{CHOCH}_2$), 2.15-1.65 (4H, $-\text{CH}_2\text{CH}(\text{CH}_3)$), 1.25-0.70 (6H, $-\text{CH}_2\text{CH}(\text{CH}_3)$). GMA content (^1H NMR): 31 mol%. Weight average molecular weight, M_w (SEC/MALS, $\text{dn}/\text{dc} = 0.136$): 48.1 kDa. Molecular weight dispersity, PDI: 1.05. R_H (DLS): 3 nm.

P4: For the synthesis of P(CHMA-co-GMA) copolymer, CHMA (1 mL, 5.7 mmol), GMA (325 μL , 2.4 mmol), ACVA (610 μL of a solution 2 mg/mL in dioxane) and CPBD (6.0 mg, 0.027 mmol) were placed in a dry glass tube with a septum cap, purged by bubbling argon through the reaction mixture for 15 min and then placed in a bath at 80 $^\circ\text{C}$ under magnetic stirring. After 2 h of reaction, the resulting copolymer was diluted with 2 mL of THF, recovered by precipitation with MeOH and dried under vacuum. Yield: 1.21 g, 93%. ^1H NMR (500MHz, CDCl_3): δ (ppm) 4.65 (1H, $-\text{OCH}$), 4.27, 3.84 (2H, $-\text{OCH}_2\text{CH}$), 3.21 (1H, $-\text{OCH}_2\text{CH}$), 2.83, 2.63 (2H, $-\text{CHOCH}_2$), 2.10-1.65 (4H, $-\text{CH}_2\text{CH}(\text{CH}_3)$), 1.15-0.85 (6H, $-\text{CH}_2\text{CH}(\text{CH}_3)$). GMA content (^1H NMR): 30 mol%. Weight average molecular weight, M_w (SEC/MALS, $\text{dn}/\text{dc} = 0.097$): 46.0 kDa. Molecular weight dispersity, PDI: 1.06. R_H (DLS): 3 nm.

4.2.4. Synthesis of SCNPs from polymer precursors

In a typical procedure, to a solution of the precursor (**P1**, 30 mg, 0.064 mmol GMA) in CH_2Cl_2 , the catalyst ($\text{B}(\text{C}_6\text{F}_5)_3$, 1.6 mg, 3.1×10^{-3} mmol) was added at r.t. under stirring. After 24 h of reaction under nitrogen atmosphere, the resulting solution was filtered, concentrated, recovered by precipitation with hexane and dried under vacuum at 60 $^\circ\text{C}$ for 24 h.

The dilution conditions were not the same depending on the molecular weight of the polymer precursor. In order to guarantee the intramolecular chain collapse, for polymers showing $M_w > 1000$ kDa, the concentration of the polymer in CH_2Cl_2 was 0.3 mg/mL and for polymers showing $M_w < 100$ kDa, the concentration was 1mg/mL.

N1: High molecular weight P(BzMA-co-GMA) SCNPs; yield: 23 mg, 77%. ^1H NMR (500 MHz, CDCl_3): δ (ppm) 7.29 (5H, Ph), 4.91 (2H, $-\text{CH}_2\text{Ph}$), 4.69 (1H- $\text{CH}_2\text{CHOCH}_2$), 3.75 (4H, $-\text{CH}_2\text{CHOCH}_2$), 2.50-1.50 (4H, $-\text{CH}_2\text{CH}(\text{CH}_3)$), 1.25-0.50 (6H, $-\text{CH}_2\text{CH}(\text{CH}_3)$). ^{19}F NMR (400 MHz, CDCl_3): δ (ppm) -135.1 (2F, *ortho*), -155.1 (1F, *para*), -164.4 (2F, *meta*). Degree of ROP by ^1H NMR: > 99%. Apparent M_w (SEC, THF): 610 kDa. Actual M_w (SEC/MALS, $\text{dn}/\text{dc} = 0.136$): 2010 kDa. Molecular weight dispersity, PDI: 1.2. Average hydrodynamic diameter, R_H (DLS, CHCl_3): 17 nm. $\text{B}(\text{C}_6\text{F}_5)_3$ content (TGA): 4.4 wt%.

N2: Low molecular weight P(BzMA-co-GMA) SCNPs; yield: 25 mg, 83%. ^1H NMR (500 MHz, CDCl_3): δ (ppm) 7.28 (5H, Ph), 4.91 (2H, $-\text{CH}_2\text{Ph}$), 4.69 (1H, $-\text{CH}_2\text{CHOCH}_2$), 3.76 (4H, $-\text{CH}_2\text{CHOCH}_2$), 2.50-1.50 (4H, $-\text{CH}_2\text{CH}(\text{CH}_3)$), 1.25-0.50 (6H, $-\text{CH}_2\text{CH}(\text{CH}_3)$). ^{19}F NMR (400 MHz, CDCl_3): δ (ppm) -135.1 (2F, *ortho*), -155.1 (1F, *para*), -164.4 (2F, *meta*). Degree of ROP by ^1H NMR: > 99%. M_{app} (SEC, THF): 37 kDa. Actual M_w (SEC/MALS, $\text{dn}/\text{dc} = 0.136$): 49.1 kDa. Molecular weight dispersity, PDI: 1.05. Average hydrodynamic diameter, R_H (DLS, CHCl_3): 2 nm. $\text{B}(\text{C}_6\text{F}_5)_3$ content (TGA): 5.1 wt%.

N3: High molecular weight P(CHMA-co-GMA) SCNPs; yield: 22 mg, 73%. ^1H NMR (500 MHz, CDCl_3): δ (ppm)) 4.78 (1H, $\text{CH}_2\text{CHOCH}_2$), 4.66 (1H, $-\text{OCH}$), 3.83 (4H, $\text{CH}_2\text{CHOCH}_2$), 2.40-1.60 (4H, $-\text{CH}_2\text{CH}(\text{CH}_3)$), 1.50-0.80 (6H, $-\text{CH}_2\text{CH}(\text{CH}_3)$). ^{19}F NMR (400 MHz, CDCl_3): δ (ppm) -135.1 (2F, *ortho*), -155.1 (1F, *para*), -164.4 (2F, *meta*). Degree of ROP by ^1H NMR: > 99%. Apparent M_w (SEC, THF): 1304 kDa. Actual M_w (SEC/MALS, $\text{dn}/\text{dc} = 0.097$): 2641 kDa. Molecular weight dispersity, PDI: 1.41. R_H (DLS): 20 nm. $\text{B}(\text{C}_6\text{F}_5)_3$ content (TGA): 4.5 wt%.

N4: Low molecular weight P(CHMA-co-GMA) SCNPs; yield: 23 mg, 77%. ^1H NMR (500 MHz, CDCl_3): δ (ppm) 4.77 (1H, $-\text{CH}_2\text{CHOCH}_2$), 4.64 (1H, $-\text{OCH}$), 3.83 (4H, $\text{CH}_2\text{CHOCH}_2$), 2.40-1.60 (4H, $-\text{CH}_2\text{CH}(\text{CH}_3)$), 1.50-0.80 (6H, $-\text{CH}_2\text{CH}(\text{CH}_3)$). ^{19}F NMR (400 MHz, CDCl_3): δ (ppm) -135.1 (2F, *ortho*), -155.1 (1F, *para*), -164.4 (2F, *meta*). Degree of ROP by ^1H NMR: > 99%. Apparent M_w (SEC, THF): 35 kDa. Actual M_w (SEC/MALS, $\text{dn}/\text{dc} = 0.097$): 46.9 kDa. Molecular weight dispersity, PDI: 1.05. R_H (DLS): 1.5 nm. $\text{B}(\text{C}_6\text{F}_5)_3$ content (TGA): 4.9 wt%.

4.2.5. Reductase properties of SCNPs

In a typical procedure, to a solution of the SCNP **N1**, 2 mg, (1.72×10^{-4} mmol $\text{B}(\text{C}_6\text{F}_5)_3$) in CH_2Cl_2 (0.6 mL), 22 μL (0.144 mmol) of dimethylphenylsilane and 15 mg (7.2×10^{-2} mmol) of diphenylethanedione were added at r.t. under stirring. The clear dark yellow solution was found to become clear and colorless in less than 15 min. The solution was precipitated into hexane to induce the precipitation of the nanoparticles, which were removed by centrifugation. The solvents of the solution, CH_2Cl_2 and hexane, were removed *via* rotavapor obtaining the crude product of the reaction, 2,7-dimethyl-2,4,5,7-tetraphenyl-3,6-dioxo-2,7-disilaoctane. Yield: 33.0 mg, 95%. ^1H NMR (500 MHz, CDCl_3): δ (ppm) 7.1-7.6 (20H, Ph), 4.84 (2H, *dl* (*syn*) $-\text{CHPh}$), 4.68 (2H, *meso* (*anti*) $-\text{CHPh}$), 0.27, 0.32 (12H, *dl* (*syn*) $-\text{SiCH}_3$), 0.07, 0.14 (12H, *meso* (*anti*) $-\text{SiCH}_3$). Turnover frequency, TOF:

$$\text{TOF} = \frac{0.95}{\left(\frac{1.72 \times 10^{-4} \text{ mmol}}{0.144 \text{ mmol}} \times \frac{15 \text{ min}}{60 \text{ min h}}\right)} = 3182 \text{ h}^{-1}$$

4.2.6. Polymerase-like properties of SCNPs: polymerization of THF

THF and GPE were distilled from CaH_2 in a vacuum line. SCNPs were dried at 60 °C in a vacuum oven overnight. All reagents were transferred in the vacuum line under argon atmosphere. SCNPs **N1-4** were first dispersed in THF and then GPE was added. After a required reaction time, a soluble poly(THF) and a gel, insoluble poly(THF) were obtained. For the separation of the soluble poly(THF) from the gel, THF was added to the reaction medium and after stirring, it was filtered. The washing procedure was repeated several times. Table 3.4 summarizes the polymerase-like properties of SCNPs **N1-4**. ^1H NMR (500 MHz, CDCl_3): δ (ppm) 7.4-6.8 (5H, Ph), 4.3-3.5 (5H, -OCH(CH_2) CH_2 OPh), 3.41(4H, -OCH $_2$ CH $_2$ CH $_2$ CH $_2$), 1.61 (4H, -OCH $_2$ CH $_2$ CH $_2$ CH $_2$).

4.2.7. Synthesis of poly(glycidyl phenyl ether) (poly(GPE))

GPE was distilled from CaH_2 in a vacuum line. $\text{B}(\text{C}_6\text{F}_5)_3$ was dried at 50 °C in a vacuum for 2 h. All reagents were transferred in the vacuum line under argon atmosphere. To a solution of GPE (3.4 mL, 25 mmol) in CH_2Cl_2 (10 mL), the catalyst ($\text{B}(\text{C}_6\text{F}_5)_3$, 13.3 mg, 0.026 mmol) was added at r.t. under stirring. After 4 h of reaction under nitrogen atmosphere, the resulting poly(GPE) was recovered by precipitation with hexane. Yield: 2.63 g, 70%. ^1H NMR (500 MHz, CDCl_3): δ (ppm) 7.4-6.7 (5H, Ph), 4.3-3.4 (5H, -OCH(CH_2) CH_2 OPh). Weight average molecular weight, M_w (SEC with PS standards): 7400 Da. Molecular weight dispersity, M_w/M_n : 2.1.

4.3. Results and discussion

4.3.1. Synthesis of linear polymer precursors

For preparing single-chain polymer nanoparticles, the first step was the synthesis of linear polymer precursors. Two different random copolymers were prepared, P(BzMA-co-GMA) and P(CHMA-co-GMA) (Figure 4.2). For both copolymers, high and low molecular polymer precursors were synthesized, having weight average molecular weight above 1000 kDa and below 100 kDa, respectively. For preparing low molecular weight polymers, $M_w < 100$ kDa, reversible addition-fragmentation chain transfer (RAFT) polymerization was used. For the case of high molecular weight polymers, M_w

> 1000 kDa, free radical polymerization under controlled synthesis conditions was used, at fractional conversion $c < 0.2$. In all the polymer precursors, the percentage of reactive functional groups was more or less similar, around 30 mol% of glycidyl moieties. The main characteristic of the precursors are reported in Table 4.1.

Table 4.1. Main characteristics of linear polymer precursors used for the synthesis of SCNPs.

Precursor	GMA (mol%) ^a	M_w (kDa) ^b	PDI	R_H (nm) ^c
P1	35	1912	1.39	20
P2	31	48.1	1.05	3
P3	27	2641	1.55	24
P4	30	46.0	1.06	3

^a Content of GMA in the precursor as determined by ¹H NMR spectroscopy.

^b Actual molecular weight as determined by combined SEC/MALS measurements.

^c Hydrodynamic radius as determined by DLS measurements.

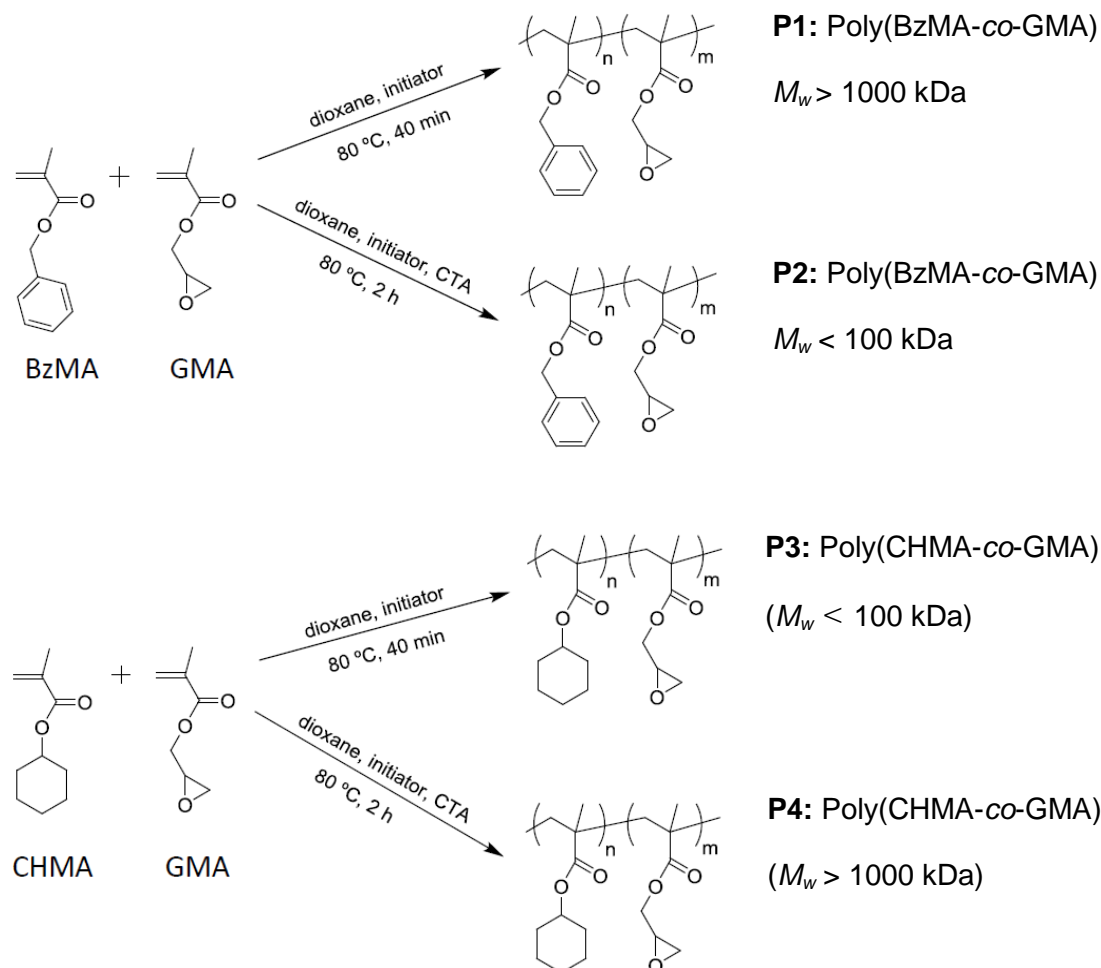


Figure 4.2. Schematic illustration of the synthesis of the copolymers poly(BzMA-co-GMA) and poly(CHMA-co-GMA) used in the synthesis of single-chain polymer nanoparticles.

4.3.2. Synthesis of SCNPs

Once the different polymer precursors were obtained, the corresponding SCNPs were synthesized. The synthesis of nanoparticles was performed in methylene chloride at room temperature under dilute conditions, in order to avoid intermolecular cross-linking reactions between different polymer chains and to guarantee intramolecular chain collapse. For the case of polymer precursors with $M_w > 1000$ kDa, the concentration of the linear precursor was 0.3 mg/mL, and for the case of polymer precursors with $M_w < 100$ kDa, the concentration was 1 mg/mL. Once the polymer was dissolved, a small amount of $B(C_6F_5)_3$ was added to the reaction as a catalyst for the ROP of the epoxide rings (Figure 4.3).

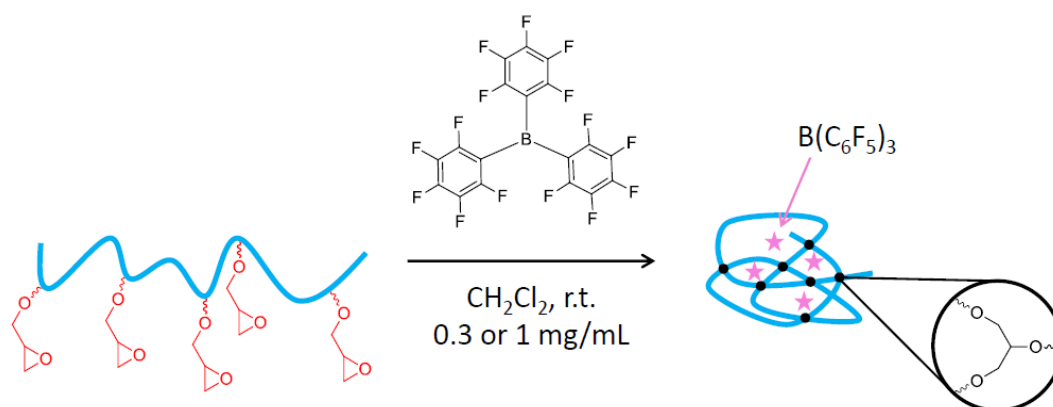


Figure 4.3. Schematic representation of the collapse process where $B(C_6F_5)_3$ catalyses the intramolecular ring-opening polymerization (ROP) of glycidyl groups.

It was found that $B(C_6F_5)_3$ catalyzed the intrachain-ring opening polymerization (ROP) of glycidyl moieties and it was simultaneously trapped inside the nanoparticles (Figure 4.3). This immobilization occurred through the binding of $B(C_6F_5)_3$ units to oxygen-containing functional groups (ether, carbonyl) of the cross-linked GMA moieties via $B \cdots O$ interactions.

4.3.3. Characterization of polymer precursors and SCNPs

Different techniques were used in order to confirm the formation of SCNPs. The intramolecular chain collapse was identified by size exclusion chromatography (SEC), due to the increase in retention time showed by the nanoparticle comparing to the corresponding polymer precursor. As an example, Figure 4.4 shows the SEC chromatogram of precursor **P1** and the corresponding SCNPs, **N1**. The retention time in SEC measurements is inversely proportional to the hydrodynamic size, and because the nanoparticle is formed from the collapse of the linear polymer, its hydrodynamic size is smaller and so it eluted later from the column, having a higher retention time

and lower value of “apparent” M_w . The main characteristic of the SCNPs **N1-4** are reported in Table 4.2.

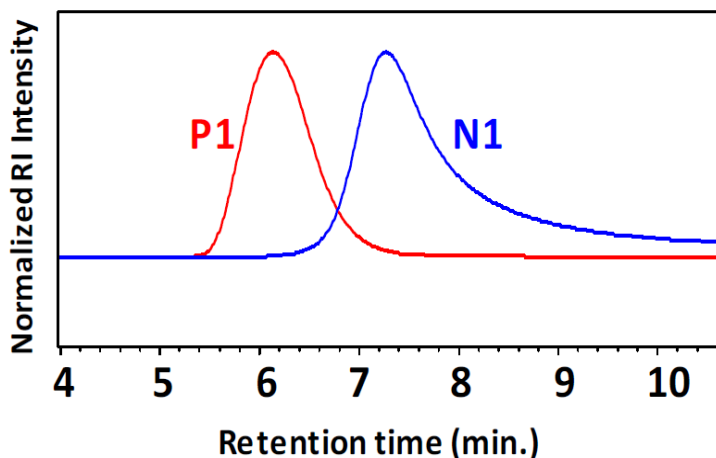


Figure 4.4. SEC chromatogram of precursor **P1** and the resulting single-chain nanoparticle, **N1**.

Table 4.2. Main characteristics of single-chain polymer nanoparticles **N1-4**.

SCNPs	B(C ₆ F ₅) ₃ content (wt%) ^a	M_{app} (kDa) ^b	M_w (kDa) ^c	PDI	R_H (nm) ^d
N1	4.4	610	2010	1.20	17
N2	5.1	37.2	49.1	1.05	2
N3	4.5	1304	2614	1.41	20
N4	4.9	35.1	46.9	1.05	1.5

^a B(C₆F₅)₃ content (wt%) in the SCNPs as determined by TGA measurements.

^b Apparent molecular weight as determined by conventional SEC measurements.

^c Actual molecular weight as determined by combined SEC/MALS measurements.

^d Hydrodynamic radius as determined by DLS measurements.

Transmission electron microscopy (TEM) and atomic force microscopy (AFM) were also used for the characterization of the synthesized single-chain polymer nanoparticles. These techniques permitted the identification of discrete nanoparticle species. The radii for **N1** were found to be 20 and 18 nm, measured by TEM and AFM, respectively (Figure 4.5). The presence of unimolecular nanoparticles was also confirmed by dynamic light scattering (DLS). The hydrodynamic radii measured using this technique for SCNPs **N1-4** are listed in Table 4.2. Figure 4.6 shows the DLS measurement for **N1** in CHCl₃ at 0.3 mg/mL, where an average hydrodynamic size radius $R_H = 17$ nm was found (see Table 4.3). In principle, SCNPs would be swelled on the DLS experiments and bigger particle sizes would be observed using this technique. However, the values were comparable to those observed by TEM and AFM, probably

due to the presence of residual solvent in the samples during TEM and AFM measurements.

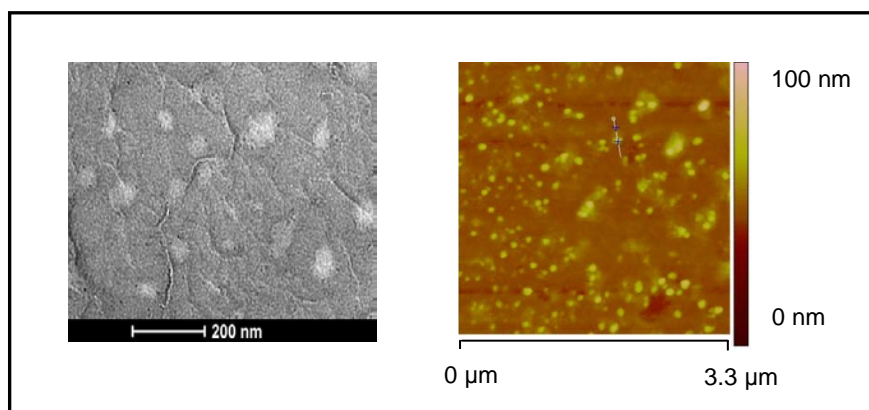


Figure 4.5. A) TEM image of **N1** showing a nanoparticle radius of 20 nm. B) AFM image of **N1**, giving a nanoparticle radius of 18 nm.

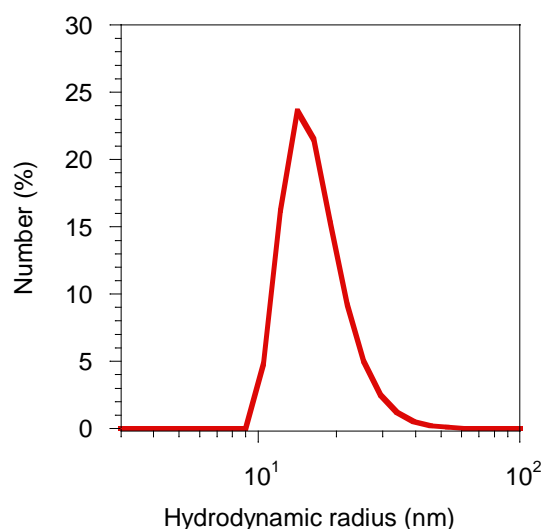


Figure 4.6. Size distribution by DLS of SCNP **N1**. Average nanoparticle radius: 17 nm.

¹H NMR was also used to confirm the formation of SCNPs. Figure 4.7 shows the spectra of the polymer precursor **P1** (top) and the corresponding SCNP **N1** (bottom). The spectrum of **P1** shows the signals corresponding to glycidyl protons at 4.19, 3.74, 3.10, 2.75 and 2.55 ppm. A complete disappearance of the signals was observed in the spectrum of **N1**, corroborating the ROP of the epoxy rings. Signal broadening was clearly observed in the spectrum of **N1**, as a consequence of the increased “solid-like” character caused by the intramolecular cross-linking reaction.

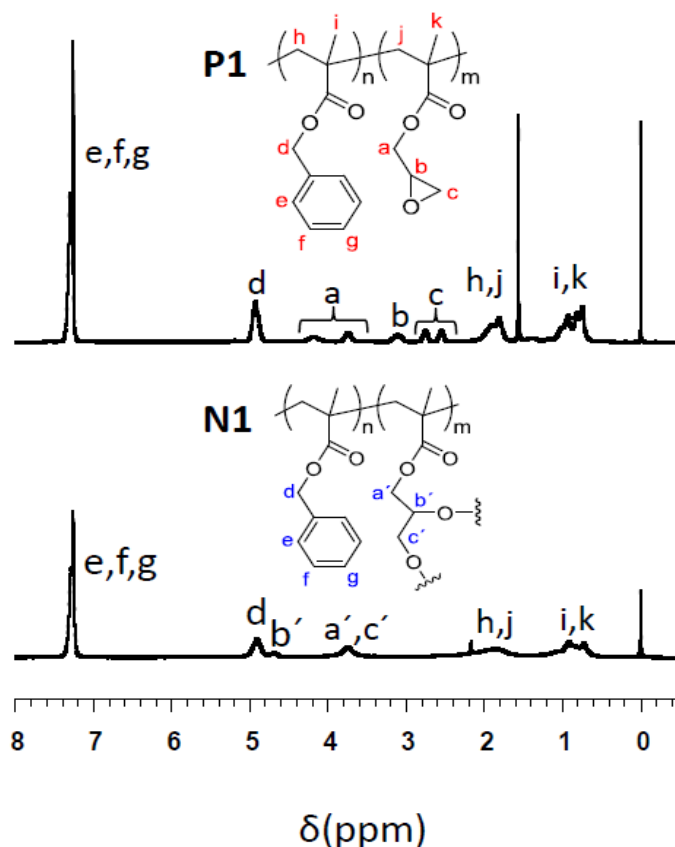


Figure 4.7. Fragments of ^1H NMR spectra of precursor **P1** (red) and SCPN **N1** (blue) in the region of the glycidyl proton bands.

The ^{19}F NMR spectrum of **N1** was also performed in order to confirm the presence of $\text{B}(\text{C}_6\text{F}_5)_3$ into the nanoparticles. In Figure 4.8 the ^{19}F NMR spectra of $\text{B}(\text{C}_6\text{F}_5)_3$, poly(glycidyl phenyl ether) (PGPE) synthesized *via* $\text{B}(\text{C}_6\text{F}_5)_3$ -catalyzed ROP and **N1** are compared. It was observed that $\text{B}(\text{C}_6\text{F}_5)_3$ showed well defined signals, at -135.1 ppm *o*-F, at -155.1 ppm *p*-F and at -164.4 ppm *m*-F atoms from the C_6F_5 rings. For the case of poly(glycidyl phenyl ether), slightly broader but clear *o*-F, *p*-F and *m*-F peaks were observed. On the contrary, for the case of SCPN **N1**, probably due to the efficient immobilization of $\text{B}(\text{C}_6\text{F}_5)_3$ moieties within the polymeric single-chain nanoparticles during the cross-linking process, only relatively broad and low intensity bands were seen, arising probably from F atoms of $\text{B}(\text{C}_6\text{F}_5)_3$ located at the external part of the nanoparticles. The efficient binding of $\text{B}(\text{C}_6\text{F}_5)_3$ within the nanoparticle during the cross-linking process *via* $\text{B}\cdots\text{O}$ interactions, induced the placement of F atoms in a relatively solid-like state and consequently they are expected to be undetectable by liquid-state ^{19}F NMR spectroscopy, being the reason of the reduction in signal intensity.

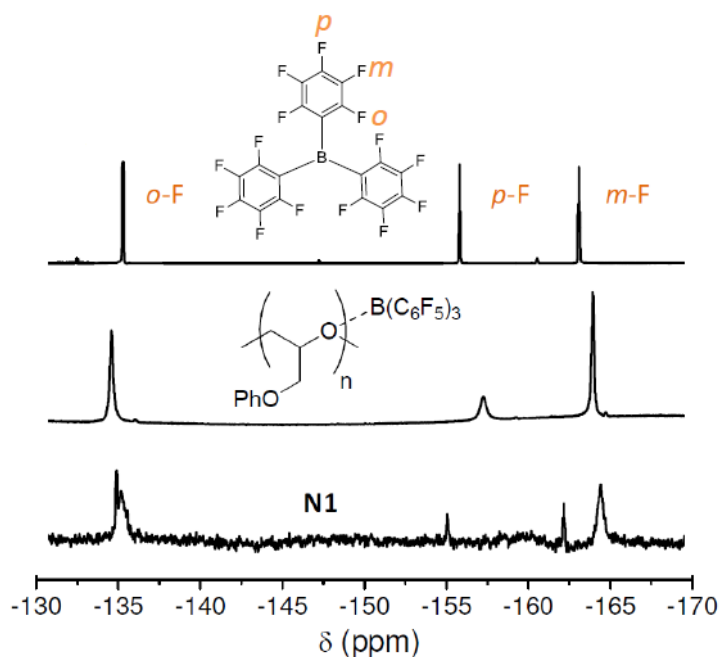


Figure 4.8. ^{19}F NMR spectra of $\text{B}(\text{C}_6\text{F}_5)_3$ (top), PGPE synthesized via $\text{B}(\text{C}_6\text{F}_5)_3$ -catalyzed ROP (middle) and **N1** (bottom).

The thermal stability of the polymer precursor **P1**, and the corresponding nanoparticle **N1** was analyzed through thermal gravimetric analysis (TGA) and it was found that the thermal stability of the nanoparticles was higher than that of the precursors (Figure 4.9). This phenomenon is probably due to the new chemical bonds that have been formed during the cross-linking process *via* ROP. There was also a weight-loss in the SCNPs of approximately 4.4 wt%, that can be reasonably attributed to the sublimation of $\text{B}(\text{C}_6\text{F}_5)_3$.

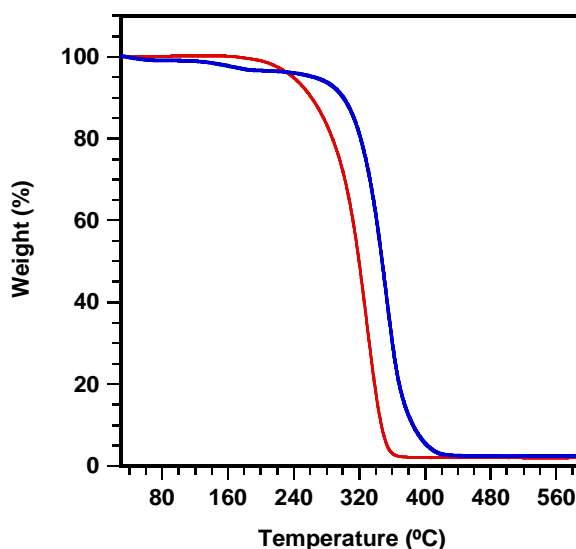


Figure 4.9. TGA curves for precursor **P1** (red) and **N1** (blue).

X-ray photoelectron spectroscopy (XPS) measurements were also performed to corroborate the presence of $B(C_6F_5)_3$ in the nanoparticles (Figure 4.10). Attempts to characterize the presence of boron atoms, which appear at 151 eV, failed due to the small amount of boron present in the nanoparticle surface. However, the peak of the F can be seen at 686 eV, because in the $B(C_6F_5)_3$, for each atom of B there are 15 atoms of F.

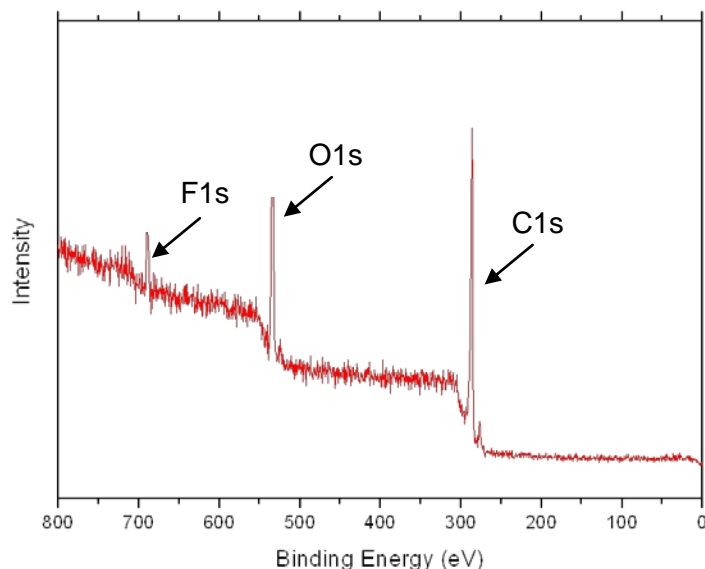


Figure 4.10. XPS spectra measurement for SCNP **N2** showed the peak of the F atom, although it was not possible to observe the peak of the B atom due to the small amount of catalyst present in the nanoparticles.

4.3.4. Molecular dynamics (MD) simulations and small angle neutron scattering (SANS) measurements

Molecular dynamics (MD) simulations were carried out in order to understand which is the morphology of the single-chain polymer nanoparticles.

MD simulations of the isolated polymer were performed by using the well-known bead spring model from Grest and Kremer.^[19] The precursor was modeled as a linear backbone with attached side groups. Inactive and active side groups contained one and three beads respectively. The cross-linkers were the end beads of the active groups. The evolution in time of the polymers was propagated by means of Langevin's dynamics,^[20] without explicit solvent and neglecting hydrodynamic effects (polymer-solvent interactions were simulated by drag and random forces obeying fluctuation-dissipation).^[20]

After equilibration of the conformations of the unlinked precursor chains, intrachain cross-linking was activated. Two linker beads formed a bond if their mutual distance was smaller than the “capture radius”. As usual in simulations of network formation,^[21] this was 30% larger than the bead size ($\approx 1\text{nm}$). In case of multiple options for bonding (several linkers within a same capture radius), the pairs to form bonds were randomly selected. Once the bond was formed between two given linkers, it remained permanent during the rest of the simulation, and bonding to other linkers was not permitted. Integration of the equations of motions was performed in the velocity-Verlet scheme, following the impulse approach.^[22]

MD runs were performed until cross-linking was totally completed, i.e, until all linkers formed mutual bonds. For a fixed molecular weight and cross-linker fraction, statistical average was performed over 200 polymers. The investigated molecular weights qualitatively corresponded to the experimental range of 10 kDa – 100 kDa. Likewise, relevant cross-linker fractions (in the range of 8 – 40%) were investigated.

The measurements by small angle neutron scattering (SANS) confirmed the unimolecular nature of the nanoparticles, since there is no evidence of multichain aggregates. Figure 4.11 provides a comparison of SANS results and MD simulations for the case of SCNP **N1**. The SCNP form factor, $S(Q)/S(0)$, was fitted using conventional Ornstein-Zernike formalism.^[23] SANS measurements give a value of the scaling exponent of $2\nu = 1.1$, which is close to that characterizing a random coil ($2\nu = 1.176$). For the case of MD simulations, the value obtained for the scaling exponent was $2\nu = 0.9$, which is close to the value of θ -coil ($2\nu = 1$). In both cases, the scaling exponent values are far from that expected for spherical objects ($2\nu = 0.667$). The good agreement between experimental and molecular dynamics simulations validated the quality of the simulation.

In all cases full cross-linking led to a reduction in the polymer size by 25-35%. This was deduced by analyzing radii of gyration. The radius \bar{R}_g is defined for each individual polymer as its time-averaged value of R_g , and accounts for the intrinsic size polydispersity originating from the nanoparticle morphologies. A representative case is given in Figure 4.12, where the backbone is 100 beads and the fraction of cross-linker is 20%. This figure shows, for the unlinked precursors and the fully cross-linked nanoparticles, the distribution of instantaneous radii of gyration R_g . The distribution of \bar{R}_g is also included.

MD simulations of the fully cross-linked nanoparticles revealed that in general they adopt relatively open morphologies (Figure 4.13), which is a very convenient feature for catalysis applications, although some relatively compact objects were also obtained.

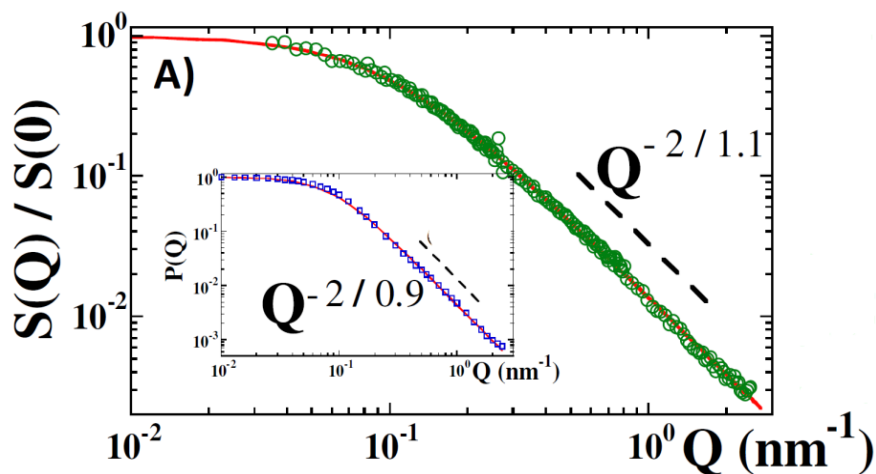


Figure 4.11. Form factor of **N1** obtained from SANS results (green circles) and from MD simulations (inset, blue squares). Solid lines are Ornstein-Zernike fits. Dashed lines represent the asymptotic regime $S(Q) \sim Q^{-2\nu}$.

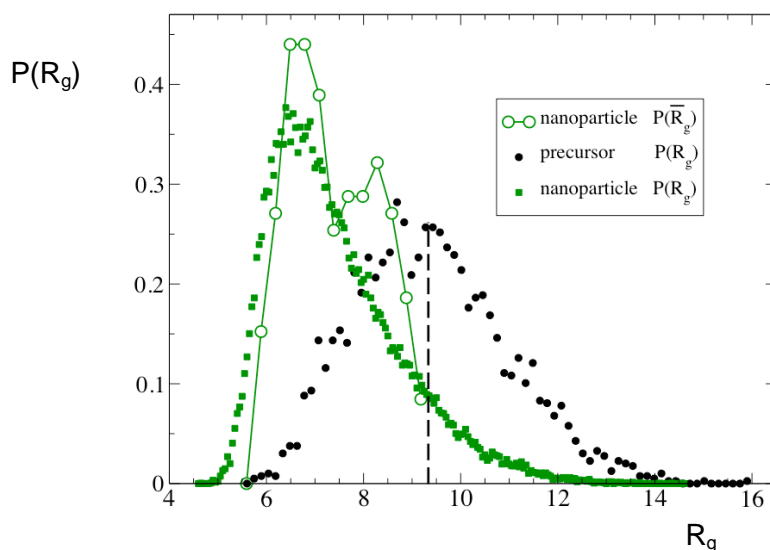


Figure 4.12. Distribution of instantaneous (R_g , filled symbols) and time-averaged (\bar{R}_g , empty symbols) radii of gyration for the simulated precursors and nanoparticles. Solid thin lines are guides for the eyes. The vertical dashed line indicates the value of \bar{R}_g for the precursors (a single value, since obviously the morphologies of the precursors are equivalent).

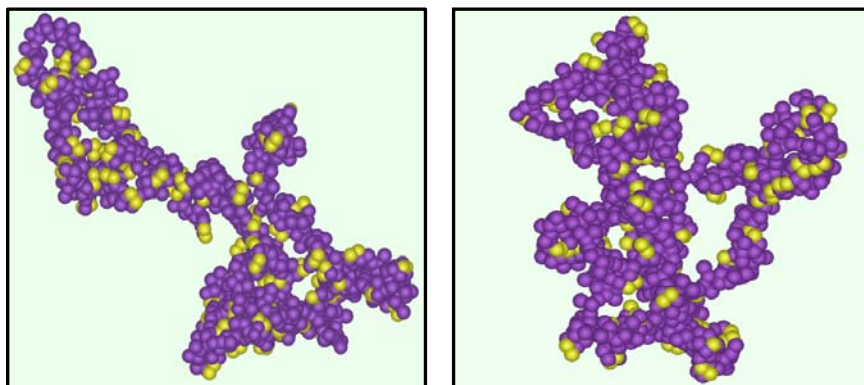


Figure 4.13. Two typical morphologies of fully cross-linked nanoparticles obtained by molecular dynamic simulations. The simulation was done using a polymer chain with a backbone of 400 beads and cross-linker fraction of 40% under good solvent conditions. The cross-linked units were represented as yellow beads.

4.3.5. Catalytic activity of SCNPs

As mentioned before, the boron compound used for the intrachain collapse process was trapped inside the nanoparticles and due to this immobilization, the nanoparticles showed catalytic activity. Specifically, they displayed reductase and polymerase enzyme-mimetic activity.

A) Reductase catalytic activity: Reduction of α -diketones to silyl-protected 1,2-diols

To evaluate the reductase catalytic activity, the SCNPs were used in the reduction of α -diketones to silyl-protected 1,2-diols. In particular, the bis-(hydrosilylation) of diphenylethanedione with dimethylphenylsilane in dichloromethane (Figure 4.14) was investigated as a function of nanoparticle loading (Table 4.3).

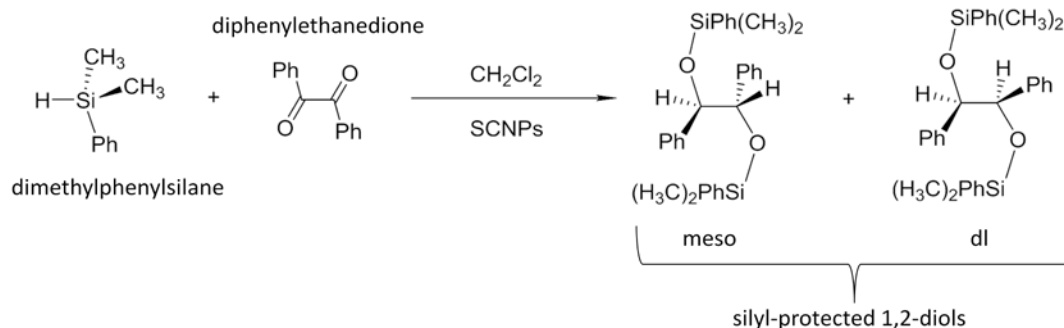


Figure 4.14. Schematic representation of the reduction of α -diketones to silyl-protected 1,2-diols.

In the last line of Table 4.3, previous results obtained from the literature are shown.^[24] The reported reaction was performed using directly the $B(C_6F_5)_3$ catalyst, 4 mol% of $B(C_6F_5)_3$, with respect to dimethylphenylsilane. What was done was to replace the $B(C_6F_5)_3$ compound by our single-chain nanoparticles that contained $B(C_6F_5)_3$. Using only 0.3 mol% of entrapped $B(C_6F_5)_3$ with respect to the amount of silane reagent, quantitative yield was obtained and practically the same meso/dl ratio, 80/20, as determined from 1H NMR (Figure 4.15). Very good yields were obtained even when the amount of catalyst was reduced until 0.12 mol%, retaining also the diastereoselectivity.

Concerning the values of the reaction time, it was observed that using SCNPs of $M_w > 1000$ kDa, the dark yellow reaction changed to colorless after 15 minutes, whereas for the case of SCNPs of $M_w < 100$ kDa, the reaction time was lower than the reaction time needed for high molecular weight nanoparticles, around 8 minutes. The longer reaction time for the case of high molecular weight nanoparticles could be attributed to a slower diffusion of the reagents to the active catalytic sites.

The turnover frequency (TOF) was found to be 3200 h^{-1} for high molecular weight nanoparticles and 5880 h^{-1} (the maximum TOF value) for low molecular weight nanoparticles.

Table 4.3. Results of the hydrosilation of diphenylethanedione using SCNPs N1-4.

SCNPS	SCNPs (mg)	$B(C_6F_5)_3$ (mol%) ^a	Reaction time	Yield (%)	Meso/dl (%) ^b	TOF (h^{-1})
N1	5	0.3 ^c	10	> 99	80/20	1989
N1	3	0.18 ^c	12	97	80/20	2707
N1	2	0.12 ^c	15	95	79/21	3182
N1	1	0.06 ^c	-	-	-	-
N2	2	0.14 ^c	7	96	79/21	5926
N2	1	0.07 ^c	-	-	-	-
N3	2	0.12 ^c	14	93	80/20	3261
N4	2	0.13 ^c	8	97	79/21	5483
-	-	4 ^d	1	> 99	79/21	1485

^a With respect to dimethylphenylsilane.

^b As determined by 1H NMR spectroscopy.

^c Entrapped in SCNPs as determined by TGA.

^d Data from reference 24.

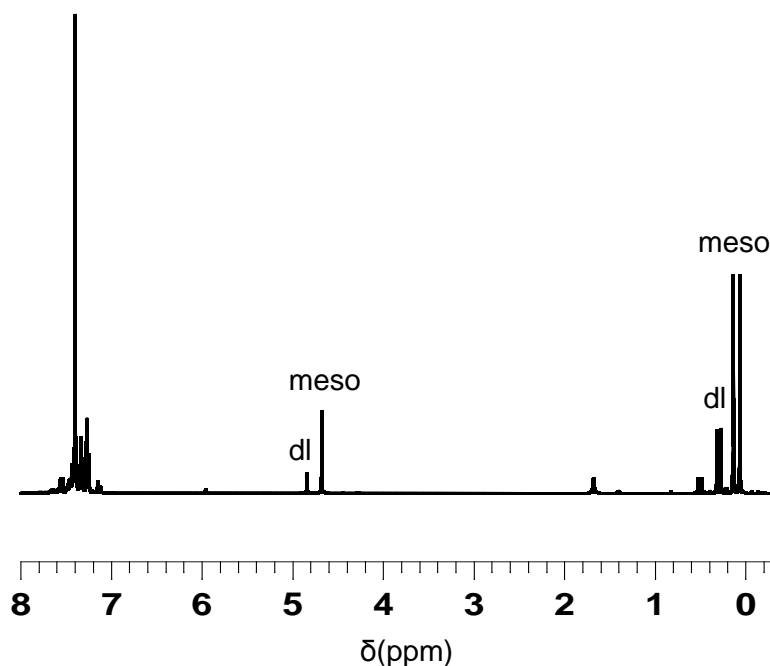


Figure 4.15. Typical ^1H NMR spectrum of showing the peaks corresponding to the diastereomers *meso* and *dl*.

B) Polymerase enzyme-mimetic activity: $\text{B}(\text{C}_6\text{F}_5)_3$ -catalyzed polymerization of tetrahydrofuran (THF) and glycidyl phenyl ether (GPE)

Here, the term “polymerase-like” refers to the ability of SCNPs **N1-4** for polymerizing tetrahydrofuran (THF) at room temperature in the presence of a small amount of GPE (Figure 4.16), to avoid confusion with the really precise activity of natural polymerase enzymes that synthesize perfectly defined biomacromolecules.^[18]

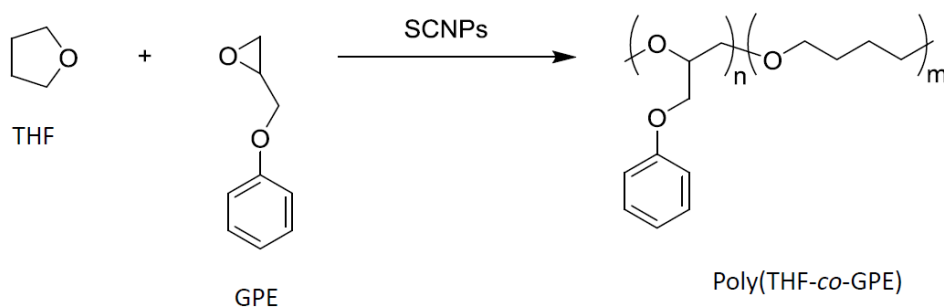


Figure 4.16. Schematic representation of the reaction of the polymerization of THF and GPE.

The polymerization of THF was analyzed in different reaction conditions, which are summarized in Table 4.4. From the data shown in Table 4.3 it was observed that the presence of GPE is critical since no poly(THF) was formed if GPE was absent. The explanation could be that GPE species presumably participates in the initial reaction steps allowing the stabilization of short cationic^[25] growing chains that later propagate

through ROP of THF units. In this sense, the use of some epoxides for initiating the cationic ROP of THF^[26] has previously been reported.

By working at low SCNP concentration (0.3-2 mg/mL) and low to moderate reaction times (6-48 h), polymers of M_w in the range of 55 to 150 kDa (SEC with PS standards) were obtained, although the conversion was really low, less than 2% and the PDI values were rather high, around 2.2 to 3.2.

By increasing the SCNP concentration to 4 mg/mL, the amount of soluble fraction increased, showing $M_w = 135$ kDa and PDI = 1.8, but a fraction of insoluble poly(THF) (Figure 4.17) was also formed after 24 h of reaction time. When working at higher SCNP concentration, around 5mg/mL, and longer reaction times, 60 h, the insoluble poly(THF) fraction increased substantially, around 50-60%. These insoluble poly(THF) gels showed a high degree of swelling in organic solvents (THF, chloroform). Finally, the results of using directly $B(C_6F_5)_3$ are shown in the last line of Table 4.4. The polymerization was carried out using 0.2 mg/mL of $B(C_6F_5)_3$ compound, and comparing with a nanoparticle concentration that contained approximately same amount of $B(C_6F_5)_3$ catalyst, a completely soluble poly(THF) was obtained. Gelation was not observed in this case, and the obtained molecular weight was much higher than when using nanoparticles.

Tabla 4.4. Results obtained for the polymerization of THF using SCNPs **N1-3** in different reaction conditions.

SCNPs	SCNP conc. (mg/mL)	$B(C_6F_5)_3$ (mg/mL)	THF (mL)	GPE (mL)	Reaction time (h)	Soluble fraction (wt%)	Gel fraction (wt%)	M_w (kDa) ^a	PDI ^a
N1	0.3	0.01	20	0.25	48	< 2	-	127	2.7
N1	0.3	0.01	20	-	48	-	-	-	-
N1	0.3	0.01	10	0.25	48	< 2	-	150	3.2
N1	2	0.09	10	0.25	6	< 2	-	55	2.2
N1	4	0.18	10	0.25	24	5.3	2.4	135	1.8
N1	5.2	0.23	10	-	60	-	-	-	-
N1	5.7	0.25	10	0.25	60	11	49	198	1.8
N2	5.3	0.27	10	0.25	60	13	61	231	2.1
N3	4	0.18	10	0.25	24	4.6	3.7	136	2.5
-	-	0.2	10	0.25	24	41	-	765	1.5

^a Data corresponding to the soluble fraction (SEC with PS standards).

^b Neat $B(C_6F_5)_3$.



Figure 4.17. Photograph of the insoluble poly(THF) gel.

Characterization of the soluble poly(THF) fraction obtained using the SCNPs by ^1H NMR spectroscopy revealed that a content of GPE was around 2 mol%, incorporated presumably at the early beginning of the ROP process (Figure 4.18).

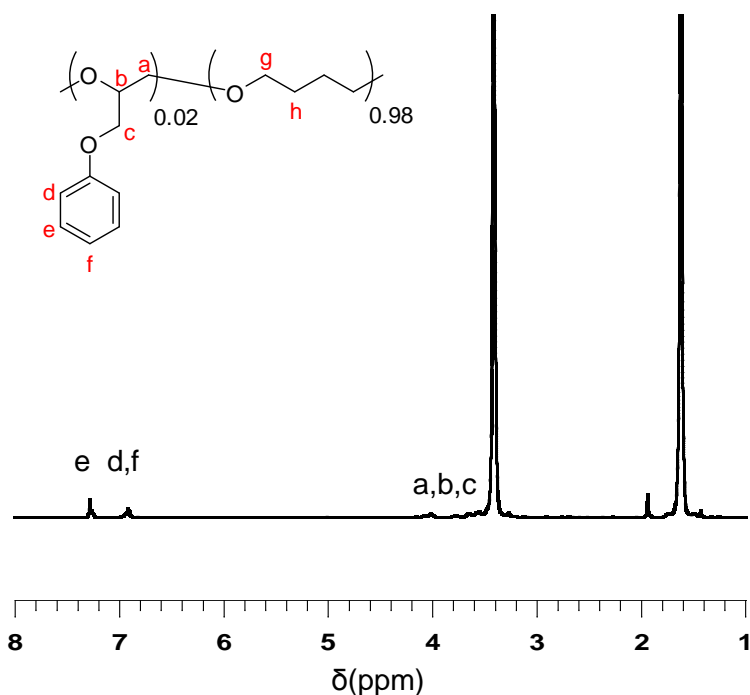


Figure 4.18. ^1H NMR spectrum of poly(THF) synthesized using SCNP N1 via GPE-triggered ROP.

In the absence of THF, GPE was polymerized using the SCNPs and the result was a low molecular weight poly(GPE) ($M_w = 6.5$ kDa and PDI = 2.2). In this case, gel formation was not observed even by working at high loading of SCNPs and up to high conversion. Several factors could contribute to the formation of the gel. First, the presumably depletion interactions between particles caused by the presence of high molecular weight polymers in the reaction medium could lead to significant interparticle attraction at high SCNPs concentration. Hence, the probability of a growing poly(THF) chain initiated in a given SCNP to connect with another SCNP will increase. Second, the probability of transfer events stopping chain growing will certainly increase with increasing SCNP concentration.

4.4. Conclusions

A new simple and efficient method for the synthesis of catalytic, enzyme-mimetic single-chain polymer nanoparticles has been developed. The cross-linking process was carried out through $B(C_6F_5)_3$ catalyzed intrachain ring opening polymerization of the glycidyl groups under dilute conditions. During this intramolecular collapse, the $B(C_6F_5)_3$ catalyst was trapped inside the nanoparticles, endowing the nanoparticles with enzyme-mimetic activity.

Combined SANS measurements and MD simulations showed a relatively open morphology of SCNPs under good solvent conditions, obtaining values of scaling exponent of $\nu = 0.55$ and $\nu = 0.45$, respectively, which seemed to be a favorable characteristic for catalysis by facilitating access of the reagents to the active catalytic sites.

For analyzing the catalytic activity of the nanoparticles, two different reactions were studied. The first reaction analyzed was the $B(C_6F_5)_3$ -catalyzed reduction of α -diketones to silyl-protected 1,2-diols with a maximum TOF of $5,880 \text{ h}^{-1}$ for low molecular weight nanoparticles. The second reaction was the pseudo-polymerase-like ROP synthesis of high molecular weight poly(THF).

This new strategy for obtaining SCNPs with enzyme-mimetic activity widens the previous "imprinted particle"^[14] and "hydrophobic cavity"^[16,17] routes, and constitutes an efficient way of producing polymer nanoparticles with good morphology for acting as catalyst.

4.5. References

1. K. A. Dill, J. L. MacCallum, *Science* **2012**, 338, 1042.
2. F. U. Hartl, M. Hayer-Hartl, *Science* **2002**, 295, 1852.
3. D. Baker, *Nature* **2000**, 405, 39.
4. V. N. Uversky, *BBA-Proteins Proteom.* **2013**, 1834, 932.
5. P. Tompa, *Trends Biochem. Sci.* **2002**, 27, 527.
6. A. K. Dunker, C. J. Brown, J. D. Lawson, L. M. Iakoucheva, Z. Obradovic, *Biochemistry* **2002**, 41, 6573.
7. P. E. Wright, H. J. Dyson, *J. Mol. Biol.* **1999**, 293, 321.
8. P. Tompa, K. H. Han, *Phys. Today* **2012**, 65, 64.
9. R. Breslow, S. D. Dong, *Chem. Rev.* **1998**, 98, 1997.
10. S. Rigaut, M-H. Delville, D. Astruc, *J. Am. Chem. Soc.* **1997**, 119, 11132.
11. T. Yamamoto, T. Yamada, Y. Nagata, M. Sugimoto, *J. Am. Chem. Soc.* **2010**, 132, 7899.
12. C. Liang, J. M. J. Fréchet, *Prog. Polym. Sci.* **2005**, 30, 385.
13. Y. Wang, H. Xu, N. Ma, Z. Wang, X. Zhang, J. Liu, J. Shen, *Langmuir* **2006**, 22, 5552.
14. G. Wulff, B-O. Chong, U. Kolb, *Angew. Chem. Int. Ed.* **2006**, 45, 2955.
15. S. Kozuch, J. M. L. Martin, *ACS Catal.* **2012**, 2, 2787.
16. T. Terashima, T. Mes, T. F. A. De Greef, M. A. J. Gillissen, P. Besenius, A. R. A. Palmas, E. W. Meijer, *J. Am. Chem. Soc.* **2011**, 133, 4742.
17. E. Huerta, P. J. M. Stals, E. W. Meijer, A. R. A. Palmans, *Angew. Chem. Int. Ed.* **2013**, 52, 2906.
18. J. M. Berg, J. L. Tymoczko, L. Stryer, *Biochemistry*, W. H. Freeman Publishers: New York, **2002**.
19. K. Kremer, G. S. Grest, *J. Chem. Phys.* **1990**, 92, 5057.
20. M. P. Allen, D. J. Tildesley, *Computer simulations of liquids*; Oxford University Press: Oxford (UK), **1989**.
21. D. R. Rottach, J. G. Curro, J. Budzien, G. S. Grest, C. Svaneborg, R. Everaers, *Macromolecules* **2006**, 39, 5521.
22. J. A. Izaguirre, D. P. Catarello, J. M. Wozniak, R. D. Skeel, *J. Chem. Phys.* **2001**, 114, 2090.

23. M. Rubinstein, R. H. Colby, *Polymer Physics*; Oxford University Press: New York, **2003**.
24. M. K. Skejel, A. Y. Houghton, A. E. Kirby, D. J. Harrison, R. McDonald, L. Rosenberg, *Org. Lett.* **2010**, *12*, 376.
25. Even if initially a cationic mechanism was assumed, further studies have shown that a zwitterionic mechanism is actually involved.
26. J. M. Hammond, J. F. Hooper, W. G. P. Robertson, J. *Polym. Sci., Part A-1: Polym. Chem.* **1971**, *9*, 265.

**Chapter 5. Photoactivated
Synthesis of Compact SCNPs via
Thiol-Yne Coupling Reaction**

5.1. Introduction, objectives and methodology

Photoactivated synthesis of nanomaterials offers significant advantages when compared to classical thermally activated routes, such as shorter reaction time, lower temperature and the possibility to control spatially and temporally the reaction through simple control over the light exposure.^[1,2]

The feasibility of photoactivated synthesis of SCNPs in dilute conditions have been recently demonstrated. Hence, in pioneering work of Meijer and coworkers,^[3] noncovalent bonded SCNPs were obtained through the collapse of photolabile protecting groups. After that, preparation of SCNPs *via* intramolecular photodimerization of coumarin- and anthracene-bearing polymers was reported by the groups of Zhao^[4] and Berda,^[5] respectively. Although different functional groups were used for the photoactivated synthesis of SCNPs, thiol-ene coupling (TEC) and thiol-yne coupling (TYC) reactions have not yet been systematically explored as an efficient approach for the facile and rapid synthesis of SCNPs under mild reaction conditions.

In recent years the photoactivated radical-mediated thiol-ene coupling (TEC)^[6] and thiol-yne coupling (TYC)^[7] reactions have emerged as powerful chemistry tools for many advanced materials, such as uniform cross-linked networks,^[8] highly porous polymeric materials,^[9] hyperbranched polymers,^[10] dendrimers,^[11] multifunctional polymer brush surfaces,^[12] stimuli-responsive star polymers,^[13] micropatterned biomaterials,^[14] functional lipid mimetics,^[15] clickable hydrogels^[16] and functionalized polypeptides.^[17] The mechanisms of both reactions are shown in Figure 5.1.

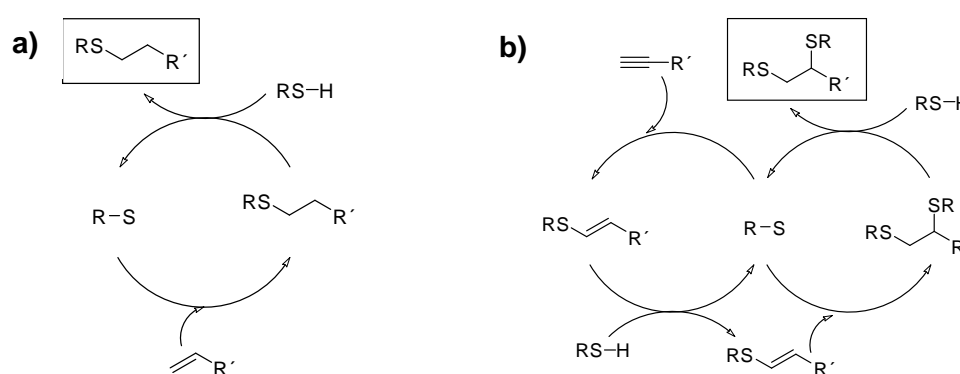


Figure 5.1. Mechanisms of a) TEC and b) TYC reactions. In the TEC mechanism, a thiyl radical undergoes the direct addition to the double bond, obtaining a thioether-vinyl radical, which undergoes chain transfer with an additional thiol molecule to yield the thiol-ene product and generating a thiyl radical that supports a new radical addition cycle. In the case of TYC mechanism, the most important feature compared to the TEC reaction is the double reactivity of the triple bond which allows constructing networks of higher cross-linking density.

Exploring the route of photoactivated TEC and TYC reactions brings some other interesting aspects, which is worth studying. In spite of the high versatility and potential of the TEC and TYC reactions,^[18-23] the difficulty to synthesize well-defined polymer precursors containing unprotected double or triple bonds along the chain has precluded the common use of these chemistries for the fast and efficient photoactivated synthesis of SCNPs. Sumerlin *et al.* showed that polymerization of unprotected propargyl methacrylate results in high polydispersity values and multimodal molecular weight distributions, as well as cross-linked networks at high conversions (> 80%).^[24] In order to avoid these branching/cross-linking secondary reactions generated due to the high temperatures needed for the adequate initiation decomposition rate, it is often necessary to protect the double and triple bonds.^[25]

In order to avoid the need for protecting the double and triple bonds, the possibility of using redox initiated RAFT polymerization has been explored in depth. This is a good solution when simple and controlled polymerization is desired because it allows the polymerization of unstable monomers at room temperature without the need to protect them.^[26]

In this chapter the following objectives are addressed:

- Study of controlled synthesis of polymer precursors bearing unprotected double and triple functional groups *via* redox initiated RAFT polymerization using commercially available monomers.
- Demonstration of the photoactivated synthesis of SCNPs through facile and rapid TEC/TYC reactions under mild conditions (r.t., air atmosphere) as an efficient route for obtaining SCNPs in a controlled way.
- Study in detail the morphology and microscopic features of the SCNPs obtained via TEC and TYC reactions. This is done with the help of molecular dynamic simulation, and seeks to provide a deeper understanding and complement the information obtained in the experimental works of the other two goals.

5.2. Experimental part

5.2.1. Reagents

Methyl methacrylate (MMA, 99%), allyl methacrylate (AMA, 98%), propargyl acrylate (PGA, 98%), 2-cyano-2-propyl benzodithioate (CPBD, > 97%), N,N-dimethylaniline (DMA, \geq 99.5%), benzoyl peroxide (BPO, 75% in water), 3,6-dioxa-1,8-octane-dithiol, (DODT, 95%), 2,2-dimethoxy-2-phenylacetophenone (DMPA, 99%), diethyl ether (99.8%) and deuterated chloroform (CDCl_3 , 99.96 atom% D, containing 0.03 % (v/v) tetramethylsilane, TMS) were purchased from Aldrich and used, unless specified, as received. Methanol (MeOH, synthesis grade) and tetrahydrofuran (THF, HPLC grade) were purchased from Scharlab. MMA, PGA and AMA were purified by eluting through neutral alumina. BPO was recrystallized from a chloroform/methanol mixture.

5.2.2. Synthesis of P(MMA-AMA) precursor (P5)

For the synthesis of **P5**, MMA (1 mL, 9.3 mmol), AMA (0.59 mL, 4.4 mmol), BPO (14.8 mg, 0.061 mmol), CPBD (4.1 mg, 0.019 mmol), DMA (7.4 μL , 0.058 mmol) and 1 mL of THF were placed in a dry glass tube with a septum cap, purged by bubbling argon through the reaction mixture for 15 min and then placed in a bath at 25 °C under magnetic stirring. After 17 h, the resulting copolymer **P5** was diluted in THF, recovered by precipitation in MeOH and dried under vacuum. Yield: 0.36 g, 24%. ^1H NMR (500MHz, CDCl_3): δ (ppm) 5.92 (2H, $-\text{CH}=\text{CH}_2$), 5.33 (2H, $-\text{CH}=\text{CH}_2$), 4.48 (2H, $-\text{CH}_2\text{CH}=\text{CH}_2$), 3.60 (3H, $-\text{OCH}_3$), 1.90-1.44 (4H, $-\text{CH}_2\text{C}(\text{CH}_3)$), 1.25-0.83 (6H, $-\text{CH}_2\text{C}(\text{CH}_3)$). AMA content (^1H NMR): 22 mol%. M_p (SEC/MALS): 127.2 kDa. PDI: M_w/M_n : 1.39.

5.2.3. Synthesis of P(MMA-PGA) precursor (P6)

For the synthesis of **P6**, MMA (1 mL, 9.3 mmol), PGA (0.44 mL, 4.5 mmol), BPO (14.9 mg, 0.062 mmol), CPBD (4.1 mg, 0.019 mmol), DMA (7.4 μL , 0.058 mmol) and 1 mL of THF were placed in a dry glass tube with a septum cap, purged by bubbling argon through the reaction mixture for 15 min and then placed in a bath at 25 °C under magnetic stirring. After 17 h, the resulting copolymer **P6** was diluted in THF, recovered by precipitation in MeOH and dried under vacuum. Yield: 0.37 g, 27%. ^1H NMR (500MHz, CDCl_3): δ (ppm) 4.60 (2H, $-\text{CH}_2\text{CH}\equiv\text{CH}$), 3.60 (3H, $-\text{OCH}_3$), 2.50 (1H, $-\text{C}\equiv\text{CH}$), 1.95-1.58 (5H, $-\text{CH}_2\text{C}(\text{CH}_3)\text{CH}_2\text{CH}$), 1.24-0.85 (3H, $-\text{CH}_2\text{C}(\text{CH}_3)$). PGA content (^1H NMR): 23 mol%. M_p (SEC/MALS): 124.4 kDa. PDI: M_w/M_n : 1.54.

5.2.4. Photoactivated synthesis of SCNPs through TEC/TYC reactions

In a typical procedure, to a solution of the precursor (**P5**: 30 mg, 0.062 mmol AMA; **P6**: 30 mg, 0.0065 mmol PGA) in THF (60 mL), DODT (**P5**: 5.1 μ L, 0.031 mmol); **P6**: 11 μ L, 0.065 mmol) and DMPA (3 mg, 0.012 mmol) were added. 12 mL of the solution were added to a 20 mL vial that was subject to UV light irradiation through an open area of 2 cm² in the 300-400 wavelength range (Figure 5.2a). After 90 min of reaction time, the resulting solution was concentrated, recovered by precipitation with diethyl ether and dried under vacuum at 60 °C for 24 h. Figure 5.2b shows the emission spectrum of the source (blue) and the transmission spectrum of the filter used in the synthesis reaction (red).

N5: Yield: 4.9 mg, 82%. ¹H NMR (500MHz, CDCl₃): δ (ppm) 4.05 (2H, -OCH₂CH₂CH₂S), 3.75 (2H, -SCH₂CH₂O-), 2.73 (4H, -CH₂SCH₂-), 1.43 (2H, -OCH₂CH₂CH₂S-). *M_w* (SEC/MALS) 127.1 kDa. PDI: 1.30.

N6: Yield: 4.9 mg, 82%. ¹H NMR (500MHz, CDCl₃): δ (ppm) 4.25 (2H, -(CO)OCH₂-), 3.93 (4H, -SCH₂CH₂O-), 3.55 (1H, -CH₂-CH(S)CH₂-), 2.79 (6H, -CH₂SCH₂-). *M_w* (SEC/MALS): 139.1 kDa. PDI: 1.41.

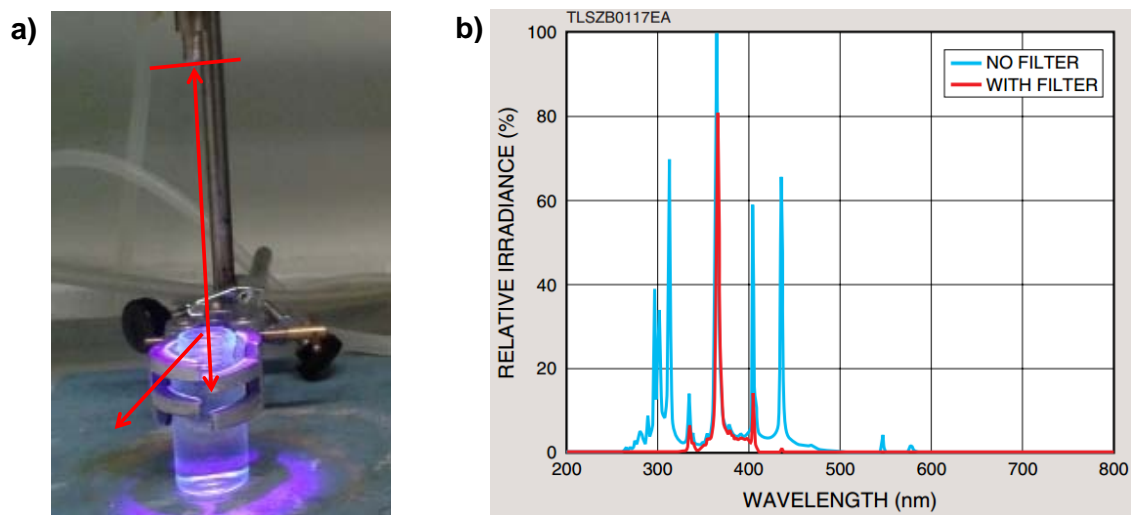


Figure 5.2. a) Illustration of the experimental set-up employed for photoactivated synthesis of SCNPs through TEC/TYC reactions. b) Spectral characteristics of the source (blue) and the filter (red).

5.3. Results and discussion

5.3.1 Synthesis of linear polymer precursors

The first step was the synthesis of polymer precursors. Two different copolymers were synthesized, PMMA-AMA copolymer (**P5**), containing pendant alkene groups, and PMMA-PGA copolymer (**P6**), containing pendant alkyne groups. For the polymerization of both copolymers, in order to avoid secondary branching/cross-linking reactions, room temperature redox-initiated RAFT polymerization was used, obtaining well-defined copolymers bearing naked alkene/alkyne functional groups (Figure 5.3).^[27]

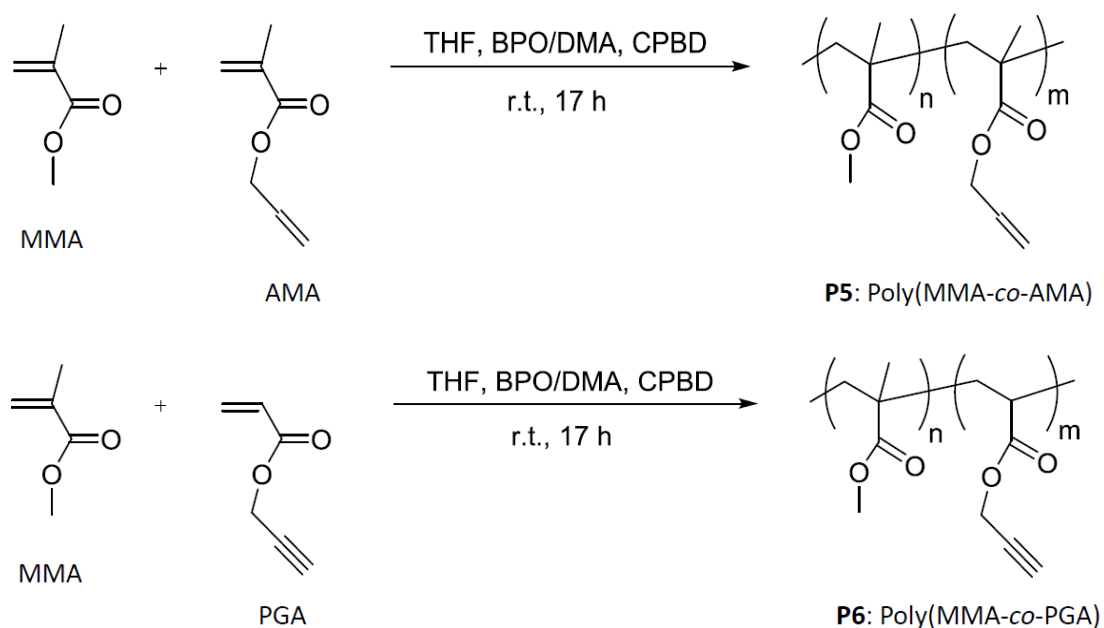


Figure 5.3. Schematic illustration of the synthesis of the copolymers poly(MMA-co-AMA) and poly(MMA-co-PGA) via redox-initiated RAFT polymerization used in the obtaining of SCNPs.

In order to compare the size and morphology of the resulting SCNPs **N5** and **N6** obtained by TEC and TYC reactions, respectively, the molar mass and the content of functional groups in both polymer precursors have to be as similar as possible. Table 5.1 summarized the main characteristics of the polymer precursors **P5** and **P6**. It is observed that the molar mass is very similar in both cases, 127.2 and 124.4 kDa, and that the percentage of functional groups is equivalent, 22 and 23%.

Table 5.1. Characteristics of precursor P5 and P6 bearing naked alkene and alkyne functional groups, respectively.

	Functional group (mol%) ^a	M_p (kDa) ^b	PDI	T_g (K) ^c	T_d (K) ^d
P5	22 mol% AMA	127.2	1.39	377	602
P6	23 mol% GMA	124.4	1.54	359	660

^a Content of functional groups in the precursor as determined by ¹H NMR spectroscopy.

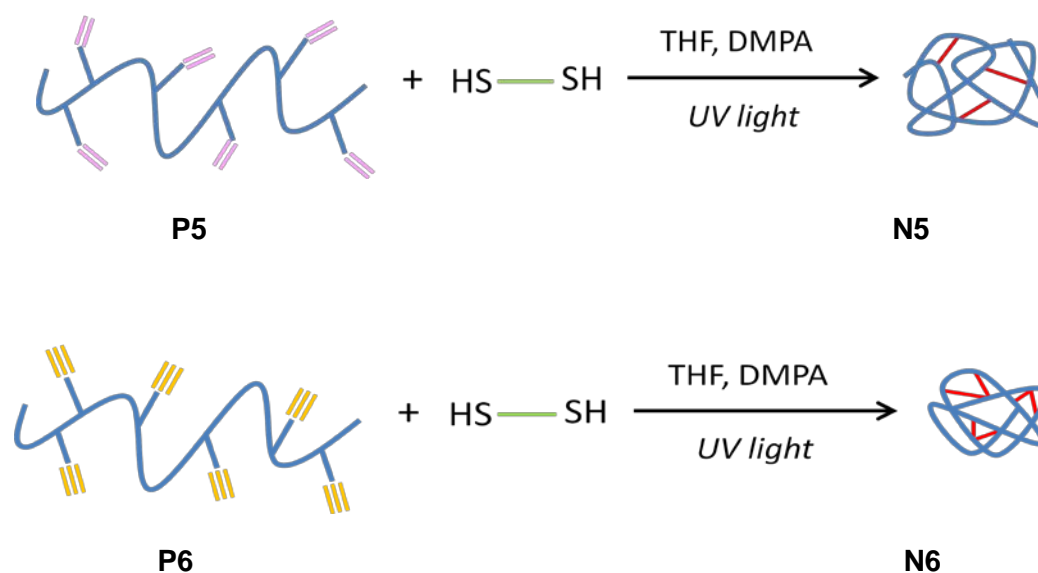
^b Absolute weight average molecular weight at the SEC peak maximum, as determined by combined SEC/MALS measurements.

^c Glass transition temperature, as determined by DSC.

^d Decomposition temperature, as determined by TGA.

5.3.2. Photoactivated synthesis of SCNPs

Once both precursors were obtained, the corresponding SCNPs were synthesized. The strategy for the preparation of SCNPs **N5** and **N6** from precursors **P5** and **P6** through photoactivated TEC and TYC reactions, respectively, is illustrated in Figure 5.4. The synthesis of nanoparticles was performed in THF at room temperature under dilute conditions (0.5 mg/mL) in order to avoid intermolecular cross-linking reactions between different polymer chains and to guarantee intramolecular chain collapse. Once the polymer was dissolved, a photoinitiator DMPA and the cross-linker DODT were added to the solution and placed under UV light at a wavelength of 300-400 nm.

**Figure 5.4.** Strategy for the preparation of SCNPs **N5** and **N6** from precursors **P5** and **P6** through photoactivated TEC and TYC reaction, respectively.

5.3.3. Characterization of polymer precursors and SCNPs

The resulting SCNPs were characterized using different techniques. The evolution of the SCNP formation process was followed by SEC/MALS, as illustrated in Figure 5.5a for the synthesis of **N5** through TEC reaction and Figure 5.5b for the synthesis of **N6** through TYC reaction. Due to the reduction in hydrodynamic size upon SCNP formation,^[28] a progressive shift of the initial SEC traces to longer retention times is clearly observed as a function of reaction time. The shift, and consequently the size reduction, is larger for the case of **N6** synthesized through TYC reaction, that could be attributed to the higher intrachain cross-linking degree in **N6** when compared to **N5**.

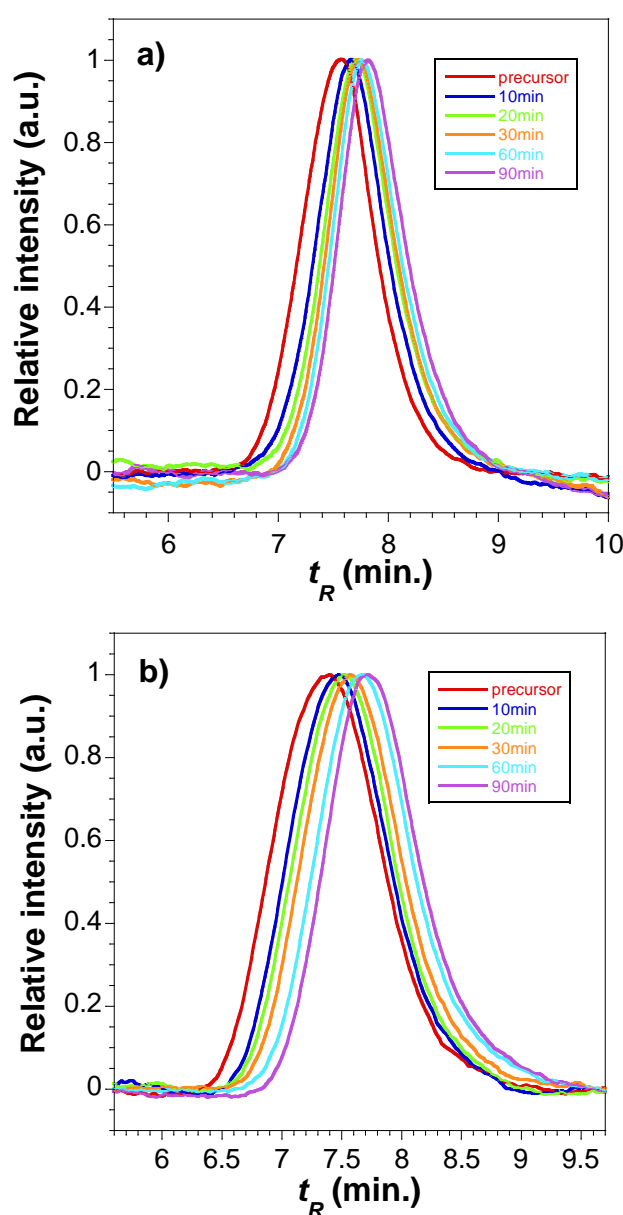


Figure 5.5. SEC/MALS traces as a function of reaction time for a) SCNP **N5** via photoactivated TEC reaction and b) SCNP **N6** via photoactivated TYC reaction.

According to control experiments, these shifts in SEC traces are not related to photodegradation of the precursor *via* chain scission. To demonstrate that the shifts in SEC traces are not related to photodegradation of the precursor, a solution of precursor **P6** (in absence of DODT and DMPA) was irradiated with UV light and it was observed that before and after UV irradiation there was no shift in the SEC retention time (Figure 5.6).

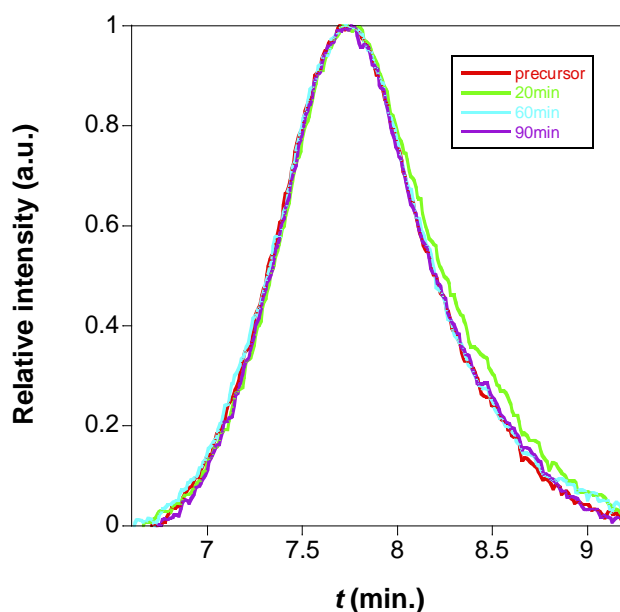


Figure 5.6. SEC/MALS traces as a function of reaction time for a solution of precursor **P6**, without DODT and DMPA.

Different concentrations were analyzed in order to investigate the effect of the precursor concentration on the actual molecular weight of the resulting SCNPs. Figure 5.7 shows a plot of M_p versus reaction time for different polymer concentrations for a) SCNPs synthesized through TEC reaction and b) SCNPs synthesized through TYC reaction. The different concentrations used for the synthesis of SCNPs are, $c = 0.5$ mg/mL (red squares), $c = 0.75$ mg/mL (blue circles) and $c = 1$ mg/mL (green triangles). Solid lines correspond to the average aggregation number (N_{agg}) defined as the ratio of the absolute weight average molecular weight of the SCNP (M_p^N), determined by SEC/MALS at the peak maximum, to the absolute weight average molecular weight of the precursor (M_p^P). For both cases, increasing the precursor concentration (c), an increase of the actual SCNP molecular weight (M_p) is observed. For the case of SCNPs synthesized through TEC reactions at the concentration of $c = 0.75$ mg/mL and $c = 1$ mg/mL, N_{agg} remains below 2. However, only nanoparticles prepared from precursor **P5** at $c \sim 0.5$ mg/mL could be considered as true SCNPs ($N_{agg} \approx 1$). For SCNP **N6**, the value of N_{agg} increases at long reaction time from 1.1 (single-chain nanoparticles) to 2.3

(double-chain nanoparticles) by increasing c from 0.5 to 0.75 mg/mL. By working at $c = 1$ mg/mL, the value of N_{agg} further increases at long reaction time to 3 (triple-chain nanoparticles). Hence, the tendency towards multi-chain aggregation on concentrating the system during SCNP synthesis was found to be higher for SCNP **N6** than for SCNP **N5**.

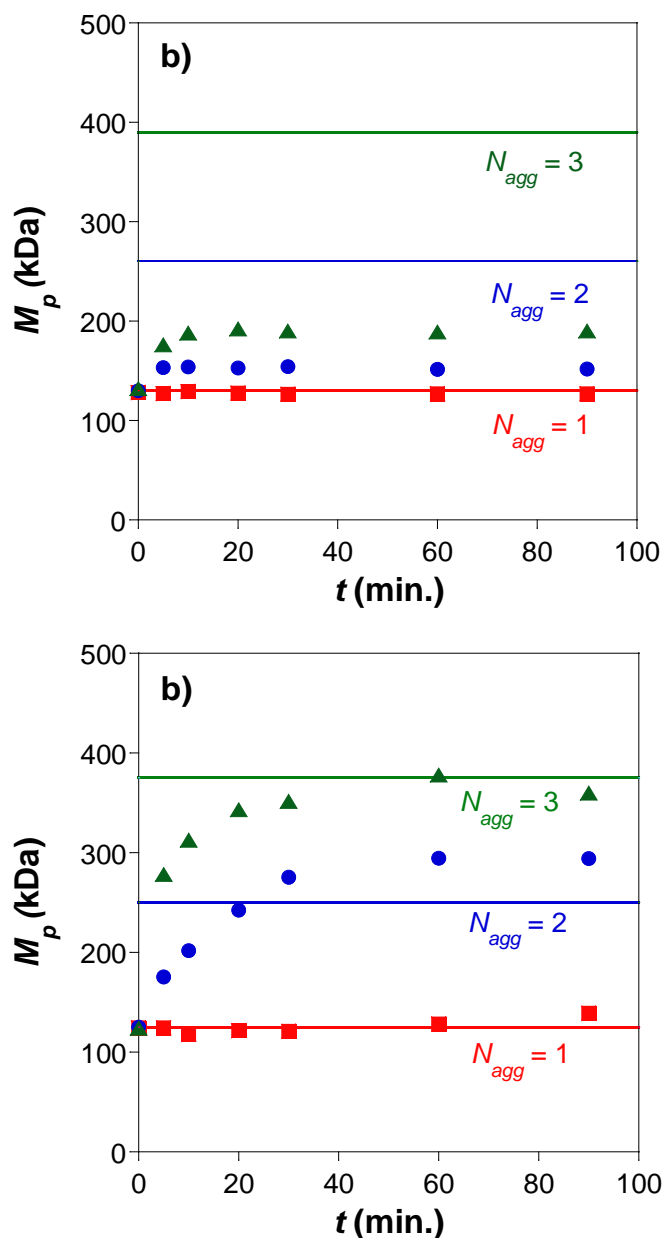


Figure 5.7. Influence of precursor concentration on the actual molecular weight (M_p) of SCNPs as a function of reaction time for a) SCNPs synthesized through TEC reactions and b) SCNPs synthesized through TYC reactions. The symbols in red, blue and green correspond to concentrations of 0.5, 0.75 and 1 mg/mL, respectively. The expected molecular weights for different values of the aggregation number (N_{agg}) are indicated as: $N_{agg} = 1$ (red line), $N_{agg} = 2$ (blue line) and $N_{agg} = 3$ (green line).

The main characteristic of SCNPs **N5** and **N6** synthesized at $c = 0.5$ mg/mL are shown in Table 5.2. Intrachain photoactivated cross-linking of precursor **P5** to SCNP **N5** produces almost no change in the glass transition temperature ($\Delta T_g = -1$ K), see Figure 5.9. In the case of **N6**, a substantial decrease in the glass transition is observed upon SCNP formation ($\Delta T_g = -13$ K), see Figure 5.9. The observed decrease in T_g of the SCNP respect to its precursor is somewhat surprising, since one might expect cross-linking to reduce the overall mobility, leading to an increase in T_g . This is indeed the case of , e.g., SCNPs synthesized with the shortest potential cross-linkers (i.e., *via* Glaser-Hay coupling^[27]) that show $T_g = 370$ K, which is 11 K above the glass transition temperature of precursor **P6**. A plausible explanation for the unconventional behavior observed in **N5** and **N6** is a combined effect of the strong intrinsic mobility and long character of the cross-linkers. These resemble poly(ethylene oxide) to some extent, which has a much stronger mobility than PMMA.^[29,30] In the common case of SCNP synthesis mediated by short cross-linkers, the latter occupy a small volume fraction of the total, and eventual differences in intrinsic mobility respect to the precursor are not able to compensate the reduction in the overall mobility induced by cross-linking. In the systems investigated in this chapter, cross-linkers are unusually long and occupy a large volume fraction of the total, in particular in the case of TYC reaction (twice than in the case of TEC reaction). This dynamic mixing of the PMMA-based precursor with the long PEO-resembling cross-linkers largely compensates the usual reduction of mobility induced by cross-linking and even enhances the overall mobility, leading to a strong reduction of T_g in **N6** respect to **P6**.

Regarding the decomposition temperature, a significant increase ($\Delta T_d = +22$ K in both **N5** and **N6**, see Figure 5.8) respect to the corresponding precursors is observed. Surprisingly, the higher intrachain cross-linking density in **N6** does not produce a larger ΔT_d when compared to that shown by **N5**. This might be due to the very high T_d of the precursor **P6** ($T_d = 660$ K) when compared to **P5** ($T_d = 602$ K).

Table 5.2. Characteristics of SCNPs **N5** and **N6** synthesized from precursors **P5** and **P6** via photoactivated TEC and TYC reactions, respectively.

	N_{agg}	M_p (kDa) ^a	PDI	T_g (K) ^b	T_d (K) ^c
N5	0.99	127.1	1.30	376	624
N6	1.12	139.1	1.45	346	682

^a Absolute weight average molecular weight at the SEC peak maximum, as determined by SEC/MALS.

^b Glass transition temperature, as determined by DSC.

^c Decomposition temperature, as determined by TGA.

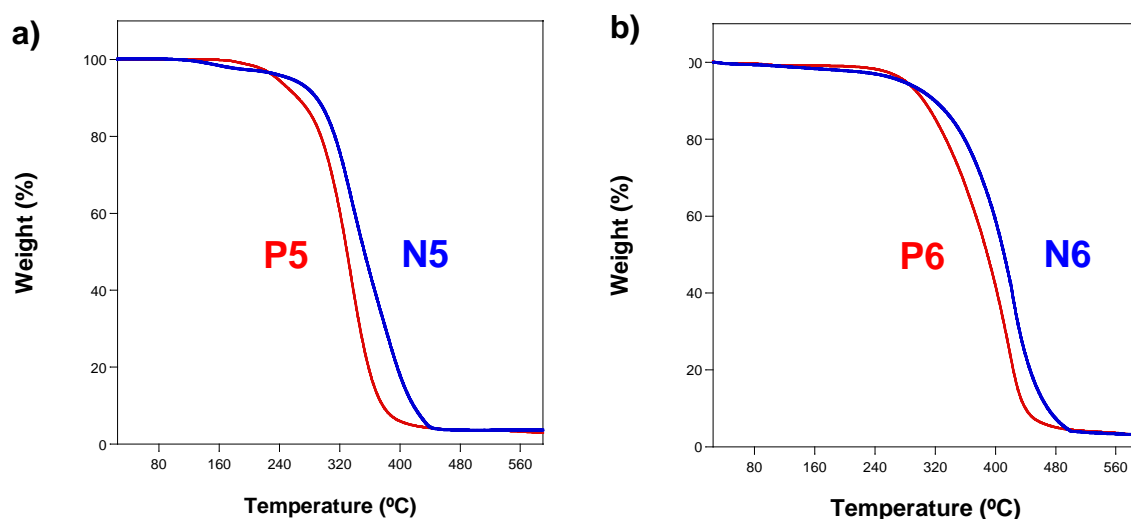


Figure 5.8. TGA curves for a) precursor **P5** and SCNP **N5** and b) precursor **P6** and SCNP **N6**.

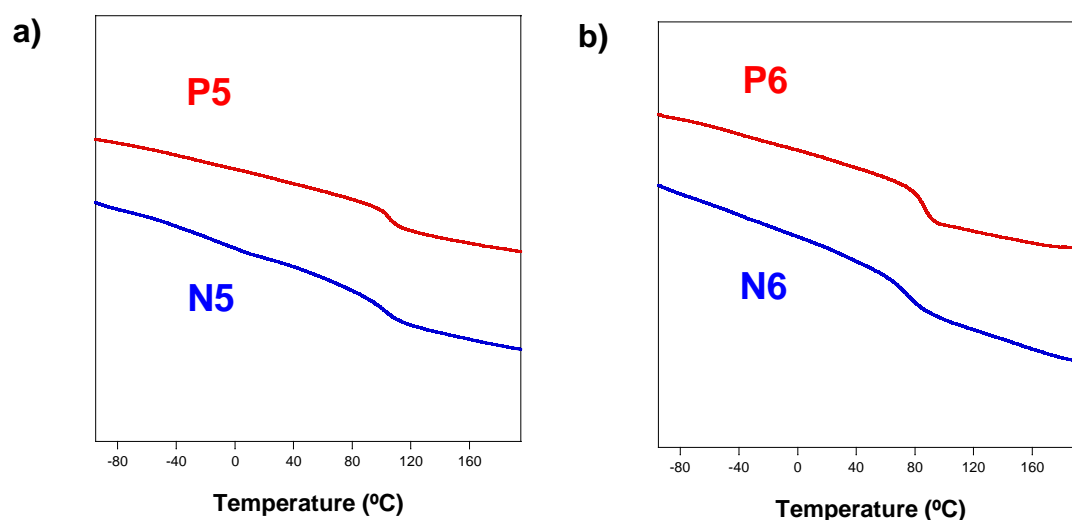


Figure 5.9. DSC traces for a) precursor **P5** and SCNP **N5** and b) precursor **P6** and SCNP **N6**.

The typical morphology of SCNPs **N5** and **N6** obtained by TEM is illustrated in Figure 5.10. The high contrast offered by the electron-rich sulfur atoms contained in **N5** and **N6** allow observing the quasi-spherical morphology of the individual SCNPs in the dry state without involving staining procedures. The diameter of the isolated SCNPs is around 10 nm (± 3 nm). The similar size observed for SCNPs **N5** and **N6** by TEM in the absence of solvent can be attributed to substrate-SCNP interactions leading to a certain spreading of the SCNP over the substrate. The nanoparticles were also measured by DLS (Figure 5.11), obtaining a smaller hydrodynamic radius (R_H) for **N5** ($R_H = 4.9 \pm 0.3$ nm) than for **N6** ($R_H = 3.6 \pm 0.2$ nm).

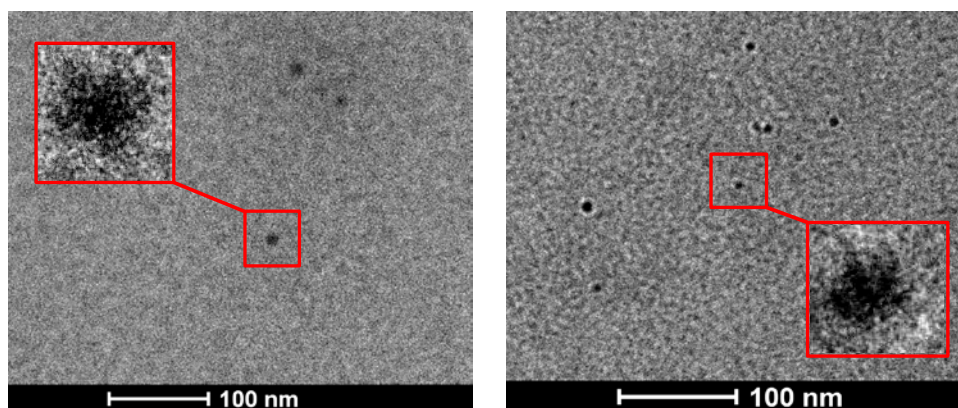


Figure 5.10. TEM images for of SCNP **N5** (left) and SCNP **N6** (right).

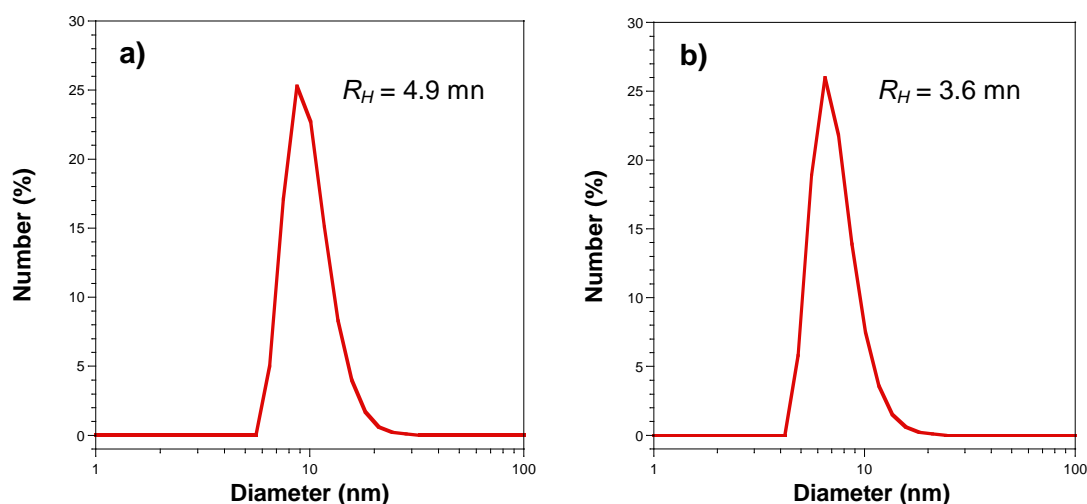


Figure 5.11. Size distribution by DLS of a) **N5** and b) **N6** in solution. Average hydrodynamic radius from 4 different measurements was found to be a) $R_H = 4.9 \pm 03$ nm and b) $R_H = 3.6 \pm 02$ nm.

^1H NMR was also used to characterize the formation of SCNPs. Figure 5.12 shows the comparison in ^1H NMR between the polymer precursor **P5** and the corresponding SCNP **N5** synthesized through TEC reaction. A large reduction in the intensity of the peaks corresponding to the allylic protons (e, f and g) was observed and new peaks (h-l) were clearly visible. The amount of double bonds consumed in the photoactivated TEC reaction was around 70%. Figure 5.13 shows the comparison between the polymer precursor **P6** and the corresponding SCNP **N6** synthesized through TYC reaction. A complete disappearance of the peaks corresponding to the protons of the propargylic groups (e and f) was observed and new peaks (h-l) were identified.

Consequently, within the limits of uncertainty of ^1H NMR spectroscopy, the amount of triple bonds consumed in photoactivated TYC reaction was almost complete.

FTIR spectroscopy measurements also supported the results obtained from ^1H NMR. For the case of **N5**, a partial disappearance of the vibration corresponding to $-\text{CH}=\text{CH}_2$ groups was observed and for the case of **N6**, the characteristic vibration bands associated to $-\text{C}\equiv\text{C}-\text{H}$ groups completely disappeared (Figure 5.14).

As a complementary technique, elemental analysis (EA) was used to determine the amount of DODT cross-linker incorporated into SCNPs **N5** and **N6**. A comparison of the theoretical composition by assuming a degree of thiol-ene/thiol-yne coupling of 100% and the corresponding experimental EA composition is shown in Table 5.3. From the ratio of the experimental to theoretical S content, a degree of thiol-ene coupling of 73% was estimated for **N5**, in good agreement with ^1H NMR data. For **N6**, a degree of thiol-yne coupling was found to be around 80%, which is lower than that estimated from ^1H NMR data (> 99%). This difference could be attributed to the lack of sensitivity of liquid-state ^1H NMR spectroscopy to protons placed in a highly cross-linked, solid-like environment. From the ratio of the experimental S contents, it is observed that **N6** contains about 92% more DODT cross-linker units than **N5** as a consequence of the higher cross-linking density due to the triple bond groups.

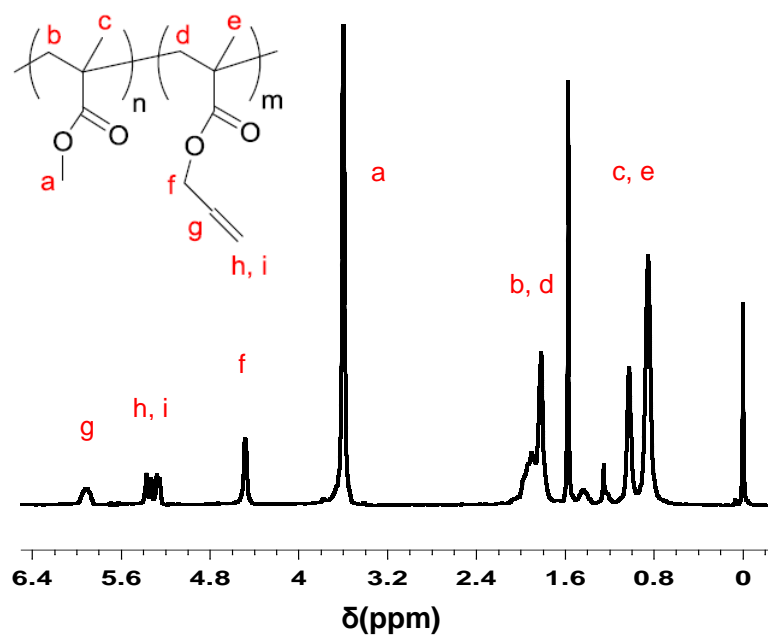
Table 5.3. Comparison of the theoretical and experimental composition of SCNPs **N5** and **N6**, as determined by EA.

	Theoretical ^a				Experimental			
	C%	H%	O%	S%	C%	H%	O% ^b	S%
N5	58.18	8.01	28.21	5.60	58.03	8.06	29.80	4.11
N6	55.66	7.68	26.67	9.99	55.38	7.26	29.46	7.90

^a Calculated by assuming a degree of thiol-ene or thiol-yne coupling of 100%.

^b Obtained as $\text{O}\% = 100 - (\text{C}\% + \text{H}\% + \text{S}\%)$.

a)



b)

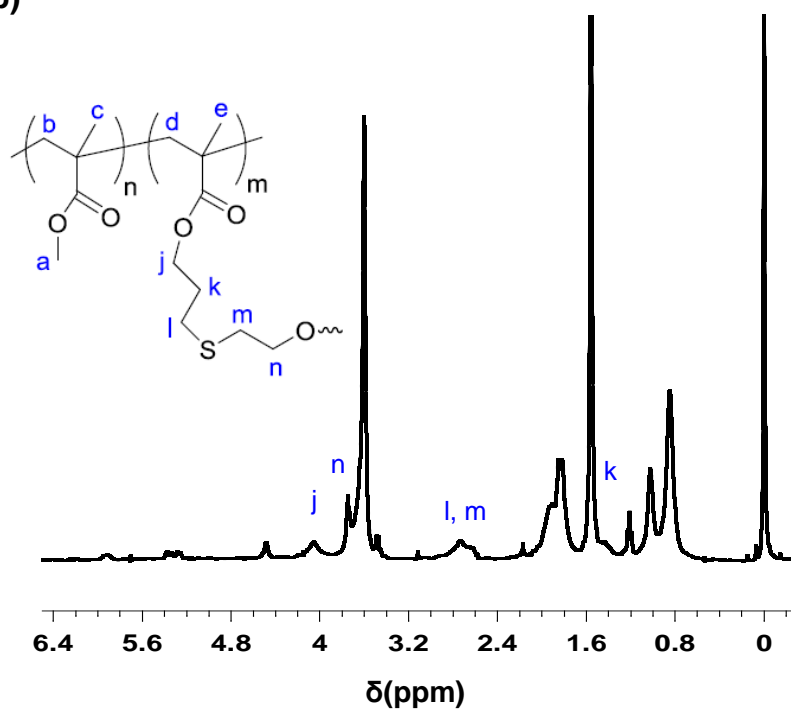


Figure 5.12. ^1H NMR spectra of a) precursor **P5** and b) SCNP **N5** synthesized through TEC reaction.

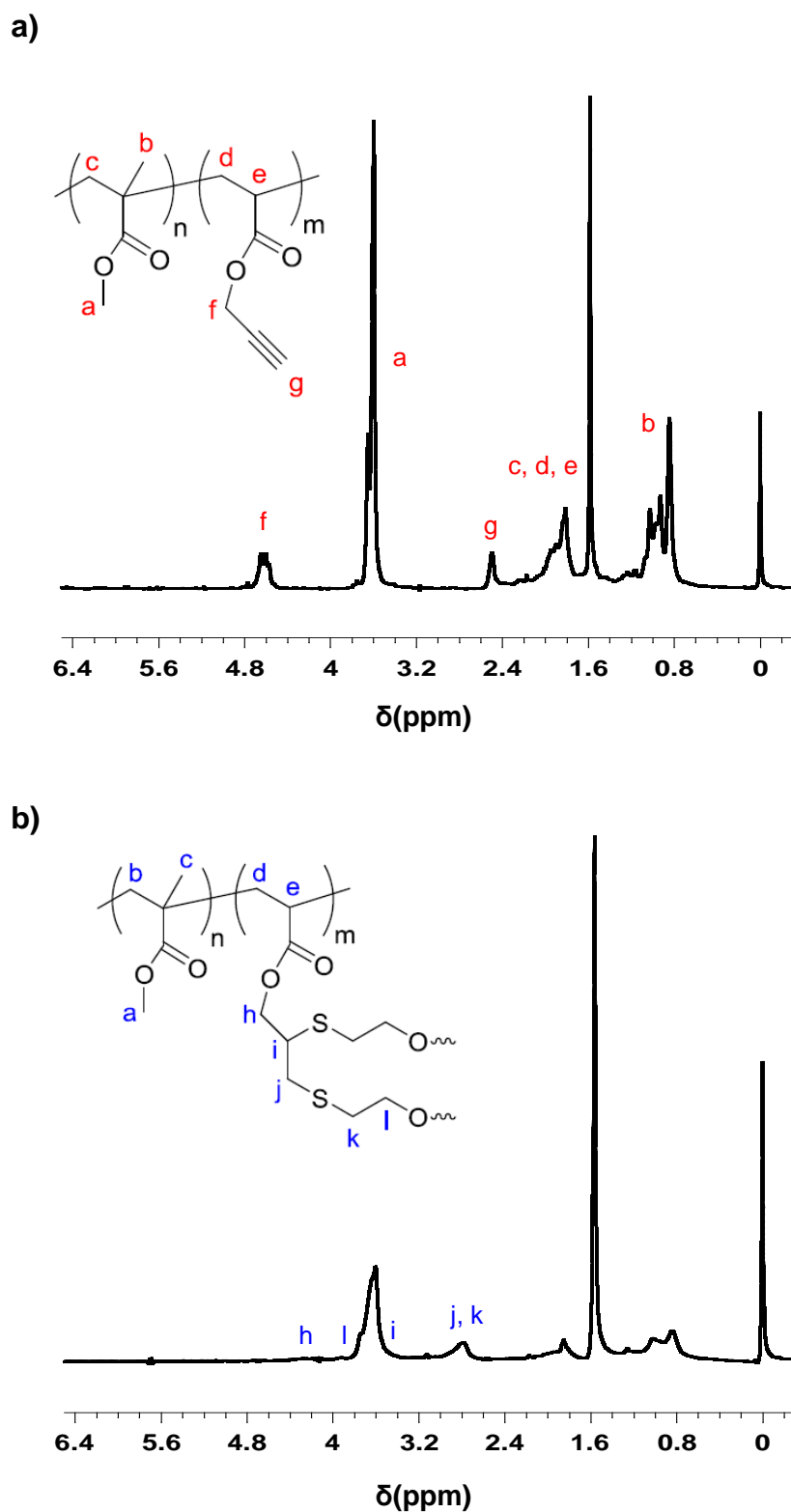


Figure 5.13. ^1H NMR spectra of a) precursor **P6** and b) SCNP **N6** synthesized through TYC reaction.

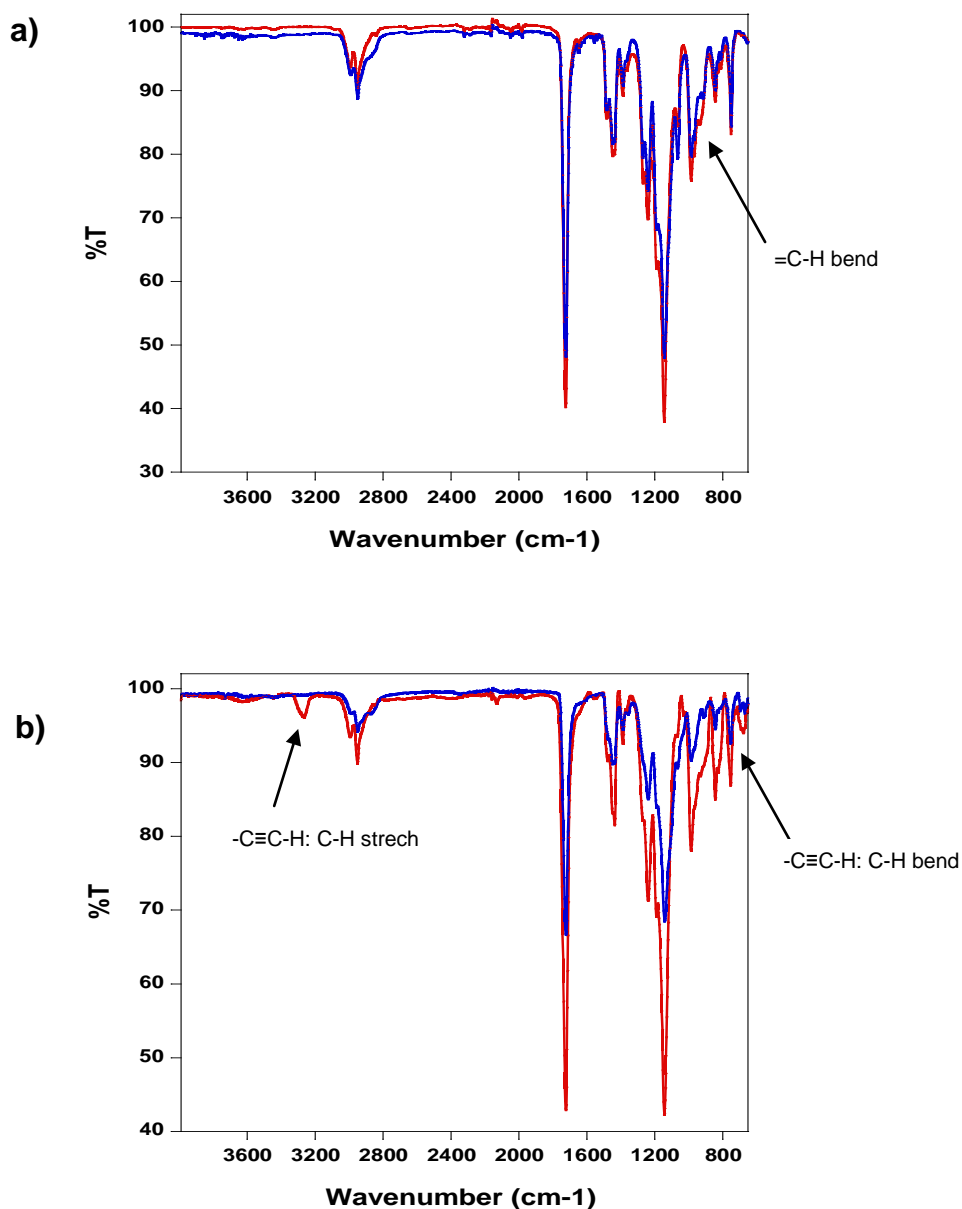


Figure 5.14. a) Comparison of the FTIR spectra of precursor **P5** and SCNP **N5**. The intensity of the $-\text{CH}=\text{CH}_2-$ vibration change upon SCNP formation. b) Comparison of the FTIR spectra of precursor **P6** and SCNP **N6**. Disappearance of the $-\text{C}\equiv\text{C}-\text{H}$ vibration bands upon SCNP formation is observed.

5.3.4. Molecular dynamics (MD) simulations and small angle X-ray scattering (SAXS)

SAXS measurements were also performed for precursors **P5** and **P6** and the corresponding SCNPs **N5** and **N6**, synthesized through photoactivated TEC and TYC reactions, respectively (Figure 5.15). From the slopes of the scattering curves in the Porod regime (indicated by the rectangle in Figure 5.15) the effective exponent ν was

determined as^[31] $d\Sigma/d\Omega \propto Q^{-1/\nu}$. This power-law directly reflects the scaling of the SCNP size vs. its molecular weight.^[32] The value obtained for this parameter is $\nu = 0.58 \pm 0.02$ for both precursors. This is in perfect agreement with the Flory exponent for a polymer in good solvent $\nu = 0.59$ (self-avoiding random walk).^[32] For **N5** $\nu = 0.51 \pm 0.02$ was obtained, which is similar to that corresponding to a polymer in θ -solution ($\nu = 0.50$).^[32] The scattering curve of SCNP **N6** in solution displays a much more pronounced slope, delivering $\nu = 0.37 \pm 0.02$. This value is close to that of a globular or spherical object ($\nu = 1/3$).^[32] Thus, the analysis of the exponents indicates more compact structures resulting from the TYC route than from the TEC reaction in good agreement with the SEC results showed in Figure 5.5 and DLS measurements showed in Figure 5.11, showing a value of R_H of 4.9 ± 0.3 nm for **N5** and 3.6 ± 0.2 nm for **N6**. In fact, the later value is very close to that expected for a globule of $M_p = 139.1$ KDa and density similar to that of PMMA, $\rho = 1.2$ g/mL: $R_H = [3M_p/(4\pi\rho N_A)]^{1/3} = 3.58$ nm, where N_A is Avogadro's number. In the case of **N5**, R_H was found to be around 35% higher than that expected for a globule.

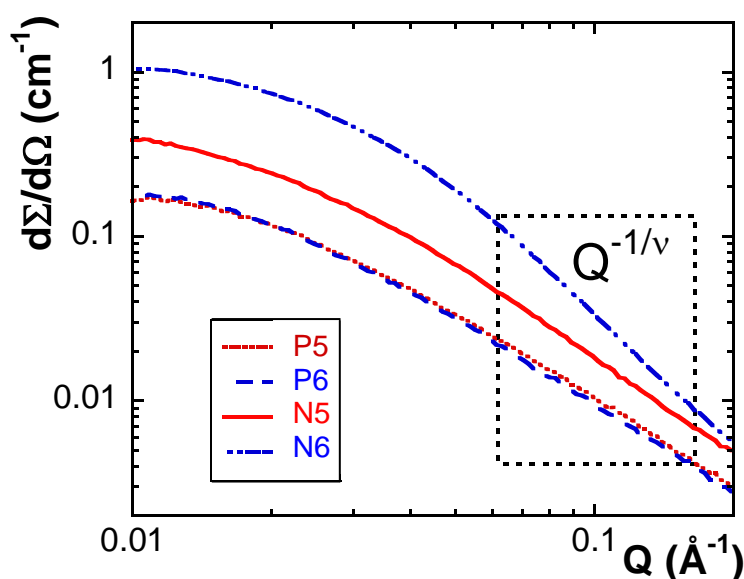


Figure 5.15. Differential scattering cross section obtained by SAXS for THF solutions at 8 mg/mL of precursors **P5** and **P6** and SCNPs **N5** and **N6**. The rectangle shows the Porod regime in which the effective exponents have been determined.

Since the differential scattering cross sections, $d\Sigma/d\Omega$, were determined in absolute units, the second virial coefficient of the osmotic pressure series expansion, A_2 , was also estimated. First, the apparent molecular mass M_{app} was calculated from the low- Q

limit of $d\Sigma/d\Omega$,^[33] i.e., $d\Sigma/d\Omega (Q \rightarrow 0) = K c M_{app}$. K is the contrast constant and c the concentration. The apparent mass and the weight average molecular mass, M_w , are related by: $M_{app} = M_w / [1 + 2 A_2 c M_w + \dots]$. For both precursors the resulting values of A_2 are very close and about $1.5 \times 10^{-3} \text{ mL}\cdot\text{mol/g}^2$, qualifying THF as good solvent for these copolymers. The value of A_2 significantly decreases for the nanoparticles, becoming much closer to the θ -point (i.e., $A_2 \approx 0$). $A_2 \approx 4 \times 10^{-4} \text{ mL}\cdot\text{mol/g}^2$ was obtained for **N5** and $A_2 \approx 2 \times 10^{-4} \text{ mL}\cdot\text{mol/g}^2$ for **N6**. These results are compatible with the values observed for the exponents ν . The weak tendency towards bad solvent conditions for the case of **N6** is in agreement with the observation of the presence of multi-chain aggregates when nanoparticle synthesis was carried out at high **P6** concentration (Figure 5.7b).

MD simulations revealed the physical origin of the nearly globular character of **N6** in solution. Simulations were based on the bead-spring model of Kremer and Grest.^[33] The precursor was modeled as a backbone of N_b connected beads. A side group was attached to each bead of the backbone. Two kind of side groups were attached: i) unreactive groups, containing a single bead, and ii) active groups, containing three beads, only the end bead being the reactive “functional group”. 20% of active groups and 80% of unreactive side groups were used, randomly distributed along the backbone of the precursor.

Bonding between the functional groups of the precursor was mediated by linear cross-linkers (bridges) of 12 beads (Figure 5.16). The two end beads of each bridge were its reactive functional groups, and formed bonds with the functional groups of the precursor. A functional group of a bridge was allowed to form a single bond with a functional group of the precursor. A functional group of the precursor was allowed to form n_{max} bonds with functional groups of the bridges. Two models of the precursor were investigated, with monofunctional ($n_{max} = 1$, model EC1) and bifunctional groups ($n_{max} = 2$, model EC2). When n_{max} bonds of a given functional group of the precursor are formed, it is referred as “fully bonded”. In the model EC2 this included the possibility of forming the two bonds with the two functional groups of a same bridge. In order to achieve full cross-linking, the used number of bridges for a given precursor was half (model EC1) or identical (model EC2) to the number of functional groups of the precursor. Precursors and bridges were propagated by Langevin dynamics.^[34]

Simulations were performed for precursors of backbone length $N_b = 50, 100, 200$ and 400 beads. At least 300 realizations were simulated for each value of N_b . Only the fully cross-linked nanoparticles (i.e., with all functional groups of the precursor being fully

bonded) were used for statistical averages. In all cases the number of fully cross-linked nanoparticles was larger than 100.

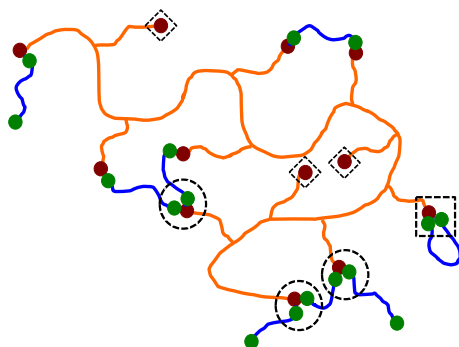


Figure 5.16. Scheme of the cross-linking process. Red and green beads represent functional groups of the precursor and the bridges, respectively. A pair of contacting red and green beads forms a bond. The rest of the precursor (orange, unreactive side groups are omitted) and the bridges (blue) are represented with lines. The dashed black circles indicate fully bonded functional groups of the precursor, which are bonded to two functional groups of different bridges. The dashed square indicates a fully bonded functional group of the precursor, which is bonded to the two functional groups of a same bridge. Fully unbonded red functional groups of the precursor are indicated by the dashed black diamonds).

Figure 5.17 shows representative snapshots of two different SCNPs of the bifunctional model (EC2) for $N_b = 400$, displaying globular and elongated morphologies.

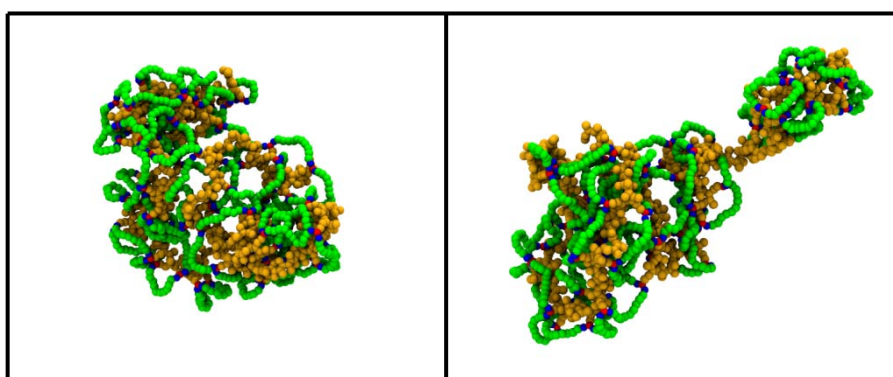


Figure 5.17. Typical snapshots of fully cross-linked nanoparticles of the bifunctional model EC2, with $N_b = 400$. These can show globular (left) and elongated (right) morphologies. Yellow and green beads are unreactive beads of the precursor and the bridges, respectively. Red and blue beads are the functional groups of the precursor and the bridges, respectively.

The morphological polydispersity of SCNPs obtained from realizations of a same precursor can be characterized by the distribution, $p(\bar{a})$, of the time-averaged asphericity \bar{a} . The asphericity parameter a of an instantaneous configuration of the nanoparticle can be calculated from their gyration tensor,^[35,36] and quantifies deviations of that configuration from a sphero-symmetrical shape ($a = 0$). For each individual SCNP, \bar{a} is obtained by averaging a over its trajectory, i.e, over its conformational dynamic fluctuations.

Figure 5.18a shows results (circles) of $p(\bar{a})$ for the case $N_b = 400$, both for the monofunctional (EC1) and bifunctional (EC2) models. For comparison we include the single value of the precursor ($\bar{a} \approx 0.45$), and the corresponding distributions (squares and diamonds) for SCNPs obtained from the same precursor ($N_b = 400$ and 20% of functional groups) but using other two different models for intrachain bonding. These two models,^[37,38] denoted as SP1 and SP2, don't have explicit bridges. The precursor of model SP1 has a single type of monofunctional group (as in the usual experimental precursors), whereas the model SP2 have two types (in identical fractions) of orthogonal monofunctional groups, i.e, bonding is only permitted between functional groups of the same type. In the models SP1 and SP2^[37,38] the bridges are not included for computational efficiency, and a bonding event just occurs when two functional groups of the precursor find each other within their capture radius. The absence of explicit bridges in the models SP1 and SP2 leads to a significant differences with the SCNPs obtained from the models EC1 and EC2 with explicit bridges investigated in this chapter. In average, the SCNPs of the bifunctional model EC2 of this work are more compact than those of the models SP1 and SP2, as indicated by the shift of $p(\bar{a})$ to smaller values of the asphericity (Figure 5.18a).

Figure 5.18b shows the average squared radius of gyration, $\langle R_g^2 \rangle$ vs. N_b , for the SCNPs obtained from the model with explicit bridges EC1 and EC2. The data can be described by a power-law $\langle R_g^2 \rangle \propto N^{2\nu}$, yielding exponents $\nu = 0.46$ and $\nu = 0.41$ for the models EC1 and EC2, respectively. This is in close agreement with the experimental trend observed by SAXS, i.e., the decrease from $\nu \approx 0.50$ for **N5** to $\nu \approx 0.37$ for **N6** (Figure 5.15), and confirms the simulated model as a qualitatively realistic picture of the cross-linking process.

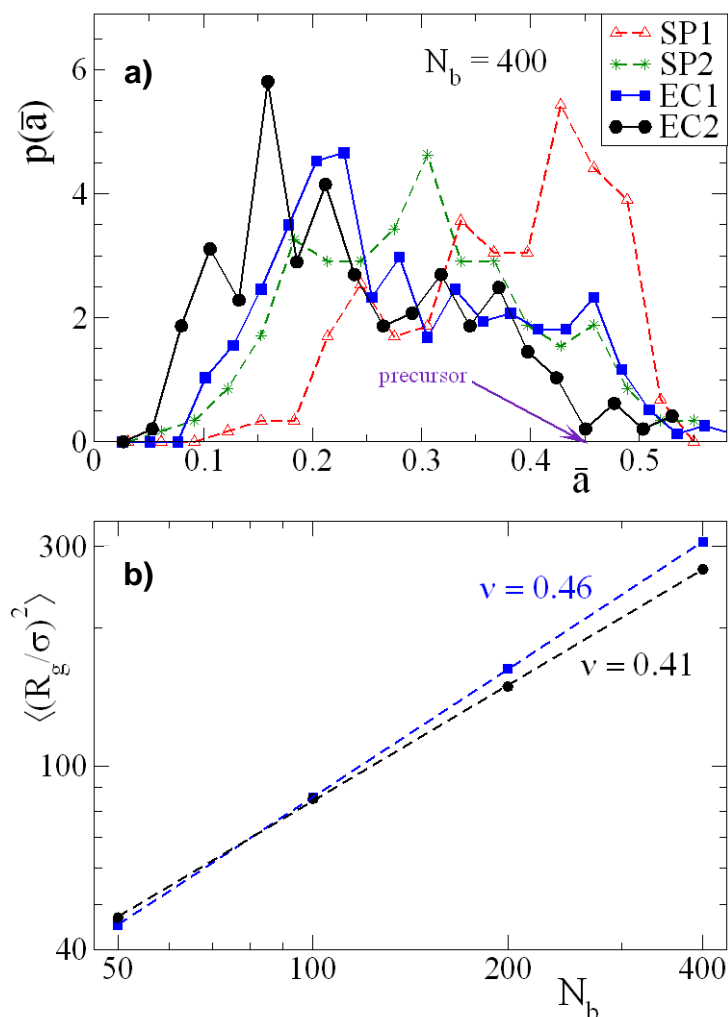


Figure 5.18. a) Distributions of time-averaged asphericities for SCNPs obtained from the same type of precursors ($N_b = 400$ and 20% of functional groups). Different data sets correspond to different models of the cross-linking route: i) mediated by explicit bridges (this work, squares: EC1; circles: EC2). ii) without explicit bridges (as in references 37,38), with a single type of monofunctional groups (SP1, triangles) and two types of orthogonal monofunctional groups (SP2, stars). The arrow indicates the single value for precursor ($\bar{a} \approx 0.45$). b) Average squared radius of gyration (normalized by σ^2) vs. N_b (models EC1 and EC2, this work). The dashed lines are fits to a power law $\langle R_g^2 \rangle \propto N^{2\nu}$, yielding exponents $\nu = 0.46$ and $\nu = 0.41$ for EC1 and EC2, respectively.

Though the model with explicit bridges does not yet provide the exponent $\nu = 1/3$ expected for globular objects, a considerable improvement towards compaction, consistent with the shift to smaller asphericities (Figure 5.18a), has been achieved respect to the models SP1 and SP2, which show scaling exponents $\nu \approx 0.5$.^[37,38] The microscopic origin of the differences observed between the SCNPs obtained from the different models and its consequences are going to be analyzed. As mentioned above, in the models SP1 and SP2, bridges are not implemented, and a bond is formed when

two functional groups of the precursor find each other within their capture radius. It has been shown that this simple approach provides a qualitatively realistic picture^[37,38] for SCNPs synthesized by the usual experimental protocols, in which SCNPs formation occurs by direct reaction between the functional groups of the precursor (as e.g., Glasser-Hay homocoupling or CuAAC click chemistry), or it is mediated by small cross-linkers (as, e.g., metal complexation or Michael addition using small acrylates). Both experimental routes are equivalent from a fundamental point of view in the *coarse-grained* picture of the models SP1 and SP2.

As mentioned before, literature data for experimental sizes of SCNPs^[39] confirms that, in general, state-of-the-art techniques produce SCNPs with morphologies resembling those of chains in θ -solvent or intrinsically disordered proteins, i.e, with $\nu \approx 0.5$, consistently with the simulation results for the generic models SP1, SP2.^[37,38] In the usual techniques where bonding occurs directly between the functional groups or is mediated by small cross-linkers, long-range loops (bonds involving long contour distances along the precursor backbone), which are the efficient mechanism for global compaction of the SCNP, are statistically very infrequent. The inhibition of long-range loops is a direct consequence of the self-avoiding character of the precursor conformations. As revealed by simulations,^[37,38] most of the bonding events involve short contour distances which just lead to local globulation of the SCNPs. The few created long-range loops are insufficient for global compaction. The use of two orthogonal functional groups (as in the model SP2) increases the average contour distance between groups that can form mutual bonds. This leads to more compact objects than in the model SP1 (Figure 5.18a) but these remain far from being globular and still show scaling exponents close to $\nu \approx 0.5$.^[37,38] As discussed in reference 38, further increasing the number of different types of functional groups beyond two (multi-orthogonal chemistry) leads to a progressive compaction approaching the globular state, so, the use of multi-orthogonal chemistry is *a priori* a promising route to synthesize compact SCNPs.

The model EC2 investigated in this chapter, with explicit and relatively long bridges, and with bifunctional groups in the precursor, provides a much more realistic picture for the synthesis of SCNPs based on TYC reaction than the models SP1 and SP2. It qualitatively reproduces and rationalizes the scaling behavior observed by SAXS for **N6**, and points to an efficient strategy to improve compaction of SCNPs. This strategy is based on the intrachain bonding mediated by relatively long cross-linkers, combined with the use of bi- or multifunctional groups in the precursor, as exemplified here with

the use of thiol-yne coupling reaction. Thus, the dangling cross-linkers can perform wide explorations of their surroundings, increasing considerably the probability of forming loops between functional groups separated by long contour distances. This ingredient combined with bi- or multifunctionality gives the possibility of high compaction through merging of several long-range loops to a single node, unlike in the case of, e.g., small multifunctional cross-linkers,^[40,41] which cannot perform wide explorations and therefore most of the merging events involve short-range loops.

These features are confirmed by representing the distribution $P(s)$ of contour distances between mutually bonded functional groups (direct bond for the models SP1 and SP2 or connected by the same bridge for the model of this work). The contour distance, $s = |i-j|$, is just defined (Figure 5.19) as the number of backbone beads comprised between the two backbone beads (i, j) to which the side groups of the mutually bonded functional groups are attached. Figure 5.19 shows the normalized $P(s)$ for the model EC2 with explicit bridges of this work, in comparison with the results for the models SP1 and SP2.^[37,38] Again, the comparison is made for SCNPs obtained from the same precursors with $N_b = 400$ and 20% of functional groups. It is observed that bonding over long contour distances is considerably enhanced in the bifunctional model EC2 with explicit bridges, leading to much stronger compaction of the SCNP. Thus, $P(s > 100)$ for the model with explicit bridges is about one order of magnitude larger than for the model SP1 that qualitatively represents the usual synthesis routes. Note that bonding with $s = 0$ is not possible (by construction) in the SP1 and SP2 models, but it occurs in the model EC2 (the dashed line extends to $s = 0$). These events are very infrequent ($< 4\%$ of the total for $N_b = 400$) and correspond to a functional group of the precursor bonded to the two functional groups of a same cross-linker, adopting a ring-like conformation.

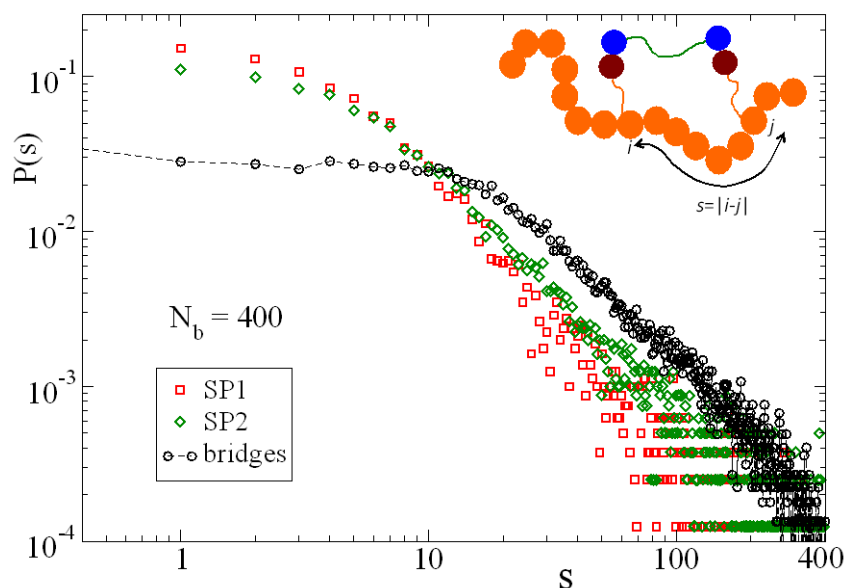


Figure 5.19. Distribution of contour distances between mutually bonded functional groups, obtained from the same type of precursors. The scheme at the top-right defines the contour distance s between two functional groups of the precursor (red beads) connected by a cross-linker (represented by the green line and its two end groups as blue beads). The main backbone of the precursor and the corresponding side groups are represented by orange beads and lines, respectively. Different data sets of $P(s)$ correspond to different models for the cross-linking route: i) mediated by explicit bridges (circles joined by dashed line, bifunctional model EC2, this work); ii) without explicit bridges,^[37,38] with a single type of monofunctional groups (SP1, squares) and two types of orthogonal monofunctional groups (SP2, diamonds).

5.4. Conclusions

A new strategy for the synthesis of SCNPs using the UV light through simple and fast TEC and TYC reactions has been explored. The photoactivated synthesis allowed a faster reaction time, lower reaction temperature and the possibility to control the reaction spatially and temporally.

Concerning the synthesis of polymer precursors, a redox initiated RAFT polymerization technique was employed, allowing the synthesis of unstable monomers without protecting them at room temperature and thus avoiding the second step of deprotection.

The characterization by SAXS of SCNPs synthesized *via* TEC reactions revealed that they showed open morphologies, resembling those of chains in θ -solvent or

intrinsically disordered proteins, which is the usual morphology for SCNPs synthesized with the state-of-the-art techniques. On the contrary, SCNPs synthesized *via* TYC reactions, revealed a near globular morphology in solution. MD simulations explained the microscopic origin of this considerable difference in the morphology.

The obtaining of more compact nanoparticles using TYC reaction is based on the combination of relatively cross-linkers with multifunctional groups in the precursor, increasing the probability of forming loops between functional groups separated by long contour distances. This eventually leads to global compaction due to the probability of forming long-range loops.

5.5. References

1. B. J. Adzima, Y. Tao, C. J. Kloxin, C. A. DeForest, K. S. Anseth, C. N. Bowman, *Nature Chem.* **2011**, *3*, 256.
2. M. A. Tasdelen, Y. Yagci, *Angew. Chem. Int. Ed.* **2013**, *52*, 5930.
3. E. J. Foster, E. B. Berda, E. W. Meijer, *J. Am. Chem. Soc.* **2009**, *131*, 6964.
4. J. He, L. Tremblay, S. Lacelle, Y. Zhao, *Soft Matter* **2011**, *7*, 2380.
5. P. G. Frank, B. T. Tuten, A. Prasher, D. Chao, E. B. Berda, *Macromol. Rapid Commun.* **2014**, *35*, 249.
6. C. E. Hoyle, T. Y. Lee, T. Roper, *J. Polym. Sci., Part A: Polym. Chem.* **2004**, *42*, 5301.
7. B. D. Fairbanks, T. F. Scott, C. J. Kloxin, K. S. Anseth, C. N. Bowman, *Macromolecules* **2009**, *42*, 211.
8. A. F. Senyurt, H. Wei, C. E. Hoyle, S. G. Piland, T. E. Gould, *Macromolecules* **2007**, *40*, 4901.
9. E. Lovelady, S. D. Kimmins, J. Wu, N. R. Cameron, *Polym. Chem.* **2011**, *2*, 559.
10. D. Konkolewicz, A. Gray-Weale, S. Perrier, *J. Am. Chem. Soc.* **2009**, *131*, 18075.
11. G. Chen, J. Kumar, A. Gregory, M. H. Stenzel, *Chem. Commun.* **2009**, 6291.
12. S. B. Rahane, R. M. Hensarling, B. J. Sparks, C. M. Stafford, D. L. Patton, *J. Mater. Chem.* **2012**, *22*, 932.
13. T. Brummelhuis, H. Schlaad, *Polym. Chem.* **2011**, *2*, 1180.
14. C. Wendeln, S. Rinnen, C. Schulz, T. Kaufmann, H. F. Arlinghaus, B. Jan Ravoo, *Chem. Eur. J.* **2012**, *18*, 5880.
15. S. S. Naik, J. W. Chan, C. Comer, C. E. Hoyle, D. A. Savin, *Polym. Chem.* **2011**, *2*, 303.
16. G. Yilmaz, M.U. Kahveci, Y. Yagci, *Macromol. Rapid Commun.* **2011**, *32*, 1906.
17. M. Lo Conte, S. Pacifico, A. Chambery, A. Marra, A. Dondoni, *J. Org. Chem.* **2010**, *75*, 4644.
18. C. E. Hoyle, A. B. Lowe, C. N. Bowman, *Chem. Soc. Rev.* **2010**, *39*, 1355.
19. M. J. Kade, D. J. Burke, C. J. Hawker, *J. Polym. Sci., Part A: Polym. Chem.* **2010**, *48*, 743.
20. A. B. Lowe, C. E. Hoyle, C. N. Bowman, *J. Mater. Chem.* **2010**, *20*, 4745.

21. C. E. Hoyle, C. N. Bowman, *Angew. Chem. Int. Ed.* **2010**, *49*, 1540.
22. A. Dondoni, A. Marra, *Chem. Soc. Rev.* **2012**, *41*, 573.
23. A. Massi, D. Nanni, *Org. Biomol. Chem.* **2012**, *10*, 3791.
24. B. S. Sumerlin, N. V. Tsarevsky, G. Louche, R. Y. Lee, K. Matyjaszewski, *Macromolecules* **2005**, *38*, 7540.
25. A. Ruiz de Luzuriaga, N. Ormategui, H. J. Grande, I. Odrizola, J. A. Pomposo, I. Loinaz, *Macromol. Rapid Commun.* **2008**, *29*, 1156.
26. G. Li, H. Zheng, R. Bai, *Macromol. Rapid Commun.* **2009**, *30*, 442.
27. A. Sanchez-Sanchez, I. Asengo-Sanz, L. Buruaga, J. A. Pomposo, *Macromol. Rapid Commun.* **2012**, *33*, 1262.
28. J. A. Pomposo, I. Perez-Baena, L. Buruaga, A. Alegría, A. J. Moreno, J. Colmenero, *Macromolecules* **2011**, *44*, 8644.
29. T. R. Lutz, Y. He, M. D. Ediger, H. Cao, G. Lin, A. A. Jones, *Macromolecules* **2003**, *36*, 1724.
30. J. Colmenero, M. Brodeck, A. Arbe, D. Richter, *Macromolecules* **2013**, *46*, 1678.
31. P. Lindner, Th. Zemb. *Neutrons, X-rays and Light: Scattering Methods Applied to Soft Condensed Matter*, Elsevier Science: North-Holland, Amsterdam, **2002**.
32. M. Rubinstein, R. H. Colby, *Polymer Physics*, Oxford University Press, Inc.: New York, **2003**.
33. K. Kremer, G. S. Grest, *J. Chem. Phys.* **1990**, *92*, 5057.
34. M. P. Allen, D. J. Tildesley, *Computer simulation of liquids*, Oxford University Press, Oxford (UK), **1989**.
35. J. Rudnick, G. Gaspari, *Science* **1987**, *237*, 384.
36. E. J. Rawdon, J. C. Kern, M. Piatek, P. Plunkett, A. Stasiak, K. C. Millett, *Macromolecules* **2008**, *41*, 8281.
37. A. J. Moreno, F. Lo Verso, A. Sanchez-Sanchez, A. Arbe, J. Colmenero, J. A. Pomposo, *Macromolecules* **2013**, *46*, 9748.
38. F. Lo Verso, J. A. Pomposo, J. Colmenero, A. J. Moreno, *Soft Matter* **2014**, *10*, 4813.
39. J. A. Pomposo, I. Perez-Baena, F. Lo Verso, A. J. Moreno, A. Arbe, J. Colmenero, *ACS Macro Lett.* **2014**, *3*, 767.
40. A. Sanchez-Sanchez, S. Akbari, A. Etxeberria, A. Arbe, A. J. Moreno, J. Colmenero, J. A. Pomposo, *ACS Macro Lett.* **2013**, *2*, 491.

41. A. Sanchez-Sanchez, S. Akbari, A. J. Moreno, F. Lo Verso, A. Arbe, J. Colmenero, J. A. Pomposo, *Macromol. Rapid Commun.* **2013**, *34*, 1681.

Chapter 6. Conclusions

This work studied several aspects of the process of synthesis of Single Chain Polymer Nanoparticles (SCNP). During this process, a polymer chain folds onto itself, and several cross-linking bonds are created, stabilizing the new shape of the molecule.

The methodological approach adopted in this study was to reproduce in the laboratory the synthesis processes, and to apply a large range of characterization techniques for obtaining detailed information about both the precursor polymer chains and the resulting SCNPs. Molecular dynamic (MD) simulation was used for gaining a deeper understanding about the microscopic processes taking place during the synthesis.

The **first main topic** addressed was the validation of scaling laws relating several properties of the SCNPs with those of their precursors. An extensive bibliographic research was carried out in order to compile a large collection of experimental data for validating the laws.

It was found that the apparent molecular weight of the SCNP and that of the precursor are linked through the equation $M_{app} = cM^\beta$, with β being a parameter related to the fractal and soft nature of the nanoparticle. Similarly, the polydispersity index is related through the equation $PDI_{app} = (PDI)^\beta$. The values of β indicate that the nanoparticle's hydrodynamic behavior is similar to that of linear polymers in θ -solvent.

The analysis of the hydrodynamic radius of SCNP in solution shows that is related to the molecular weight through the equation $R_H \propto M^\nu$. This law displays certain dependency in the chemical nature of the precursor and the amount of reactive cross-linker. It was found that the hydrodynamic radius of the SCNPs is larger than that of compact or partially swollen globules of the same nature and molecular mass, indicating that the morphology of the nanoparticles is sparse.

The last property analyzed was the intrinsic viscosity, which is related to the molecular weight of the precursor following the equation $[\eta] = K_\eta M^\alpha$. The intrinsic viscosity of SCNPs is systematically smaller than that of linear chains, and low-functionality stars. This is due to the complex architecture at the nanoscale of the nanoparticle. However, when compared with hyperbranched and dendrimeric polymers, the behavior of the intrinsic viscosity is more complex because it depends on the molecular weight and amount of cross-linker of the SCNP.

The **second main topic** explored during this thesis was the ability of SCNPs to act as efficient catalysts. The collapse process was carried out using the $B(C_6F_5)_3$ catalyst, which at the end of the cross-linking process was trapped inside the nanoparticles, endowing them with enzyme-mimetic activity.

SANS measurements together with simulation work determined that SCNPs displayed a relative open structure, which is potentially a favorable feature when using the nanoparticles as catalysts due to the easier diffusion of the reactants to the catalytic sites.

The efficiency of the nanoparticles as catalysts was tested through two different reactions. The first reaction analyzed was the $B(C_6F_5)_3$ catalyzed reduction of α -diketones to silyl-protected 1,2-diols. A remarkably value of TOF was obtained when compared with other polymer catalytic systems. The second reaction analyzed was the polymerization of THF in the presence of a little amount of GPE. The result was the obtaining of polyTHF gel. Therefore, these SCNPs displayed reductase and polymerase enzyme-mimetic activity.

The **last main topic** studied was the possibility of using thiol-yne (TYC) and thiol-ene (TEC) reactions as simple and efficient ways for synthesizing nanoparticles. Furthermore, the possibility of photoactivating the processes was also explored, as an interesting option which offers enhanced selective control.

In TYC and TEC reactions, double and triple bonds are typically protected in order to avoid secondary reactions, which take place due to the relatively elevated temperature involved in the polymerization process. An alternative path using a redox initiated RAFT polymerization was studied here. This process allowed achieving polymerization at room temperature, and eliminating the need to protect the double and triple bonds.

The characterization by SAXS of SCNPs synthesized *via* TEC reactions revealed that they showed a relative open morphology. On the contrary, nanoparticles synthesized *via* TYC reactions, showed a near globular morphology in solution. MD simulations explained the difference in morphology for both types of nanoparticles. Therefore, a promising strategy for the synthesis of compact nanoparticles was achieved, based on the combination of relatively long cross-linkers with multifunctional groups in the precursor.

Publications obtained during the Thesis:

1. I. Perez-Baena, I. Asenjo-Sanz, A. Arbe, A. J. Moreno, F. Lo Verso, J. Colmenero, J. Pomposo, *Macromolecules* **2014** (under revision).

Efficient route to compact single-chain nanoparticles: photoactivated synthesis via thiol-yne coupling reaction

2. I. Perez-Baena, A. J. Moreno, J. Colmenero, J. A. Pomposo, *Soft Matter* **2014** (In press).

Single-chain nanoparticles vs. Star, hyperbranched and dendrimeric polymers: Effect of the nanoscopic architecture on the flow properties at diluted solutions.

3. J. A. Pomposo, I. Perez-Baena, F. Lo Verso, A. J. Moreno, A. Arbe, J. Colmenero, *ACS Macro Lett.* **2014**, *3*, 767.

How far are single-chain polymer nanoparticles in solution from the globular state?

4. I. Perez-Baena, F. Barroso-Bujans, U. Gasser, A. Arbe, A. J. Moreno, J. Colmenero, J. A. Pomposo, *ACS Macro Lett.* **2013**, *2*, 775.

Endowing single-chain polymer nanoparticles with enzyme-mimetic activity

5. A. Sanchez-Sanchez, I. Perez-Baena, J. A. Pomposo, *Molecules* **2013**, *18*, 3339.

Advances in click chemistry for single-chain nanoparticle construction

6. P. Khanjari, I. Perez-Baena, L. Buruaga, J. A. Pomposo, *Macromol. Symp.* **2012**, *321-322*, 145.

Unimolecular nanoparticles via carbon-carbon “click” chemistry for all-polymer nanocomposites.

7. J. A. Pomposo, I. Perez-Baena, L. Buruaga, A. Alegria, J. Colmenero, *Macromolecules* **2011**, *44*, 8644.

On the apparent SEC molecular weight and polydispersity reduction upon intramolecular collapse of polydispersity chains to unimolecular nanoparticles

Appendix I. Size Exclusion Chromatography

Note. The following text is an extract of the Master Thesis of the author of this Thesis. It contains a detailed description of the working principle of the Size Exclusion Chromatography (SEC) and the relevant dynamic magnitudes which are used to analyze and process the information obtained with this set up. The text has been added as complementary information for the reader unfamiliar with the subject. This information is mainly relevant to the discussions exposed in chapter 3 of this Thesis.

I.1. Size Exclusion Chromatography (SEC)

Size exclusion chromatography is a standard technique for determining molar mass (molecular weight) averages and molar mass (molecular weight) distributions, MMDs (MWDs), of polymers. The principle of SEC is the separation of molecules based strictly on their hydrodynamic radius (R_H) or volume (V_H), rather than their molecular weight. By definition, R_H is the radius of a hypothetical sphere that diffuses with the same speed as the molecule under examination. In the case of the polymers, R_H and R_G , the radius of gyration, are related by means of a constant, where the latter one is defined by the following expression [26]:

$$R_G^2 = \frac{\sum m_i r_i^2}{\sum m_i} \quad (1)$$

where m_i is the mass of the i^{th} atom in the particle and r_i is the distance from the center of mass to the i^{th} particle.

The separation process takes place in a column which is packed with porous microparticles of typically 5 to 20 μm such as silica, polymers (e.g. styrene-divinylbenzene copolymer, polyhydroxymethacrylate, polyvinyl alcohol)... Because of their size, the larger molecules are excluded from some of the pores in the packing material and therefore elute faster through the column than the smaller molecules, which penetrate more deeply into the pores and elute later. In effect, the molecules are classified by size, with the largest one eluting first and the smallest one last. Figure 9 illustrates the mechanism of SEC separation [27].

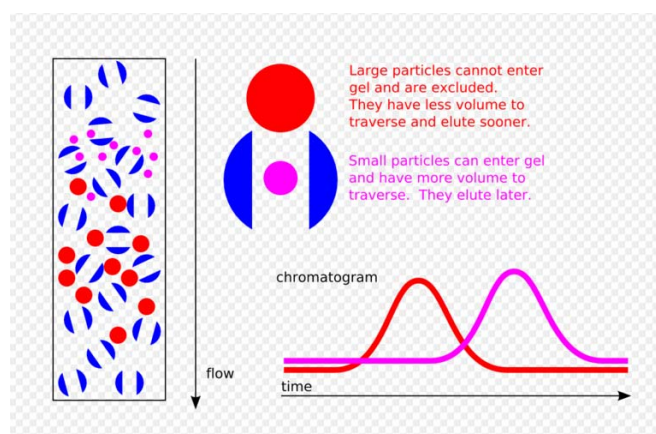


Figure 9. Schematic illustration of SEC.

In a SEC process, the mobile phase (solvent), known as liquid carrier, is continuously flowing through the system. The sample solution is then injected and carried through the column(s) where the size separation process takes place. When the sample elutes from the column(s) it passes through a detector or series of detectors and the output is often analyzed by a SEC software package on the computer.

Figure 10 illustrates the recorded SEC chromatogram for a polymer sample. After the injection of the sample, the detector gives a basic line until the first bigger molecules start coming out, increasing the response of the detector gradually, until it reaches to a maximum and then goes decreasing gradually and return again to the basic line when all the molecules have already come out.

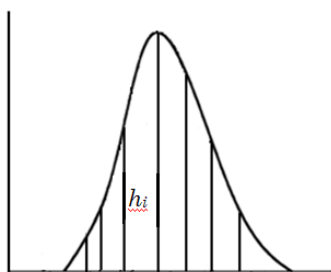


Figure 10. Illustration of SEC chromatogram.

From the moment we introduced the sample into the column, a given sample will be detected at time t (usually given in minutes), that is called retention time of that sample. If the flow of the liquid carrier is F (ml/min), the multiplication of both gives the so called elution volume, V_e :

$$V_e = Ft \quad (2)$$

The height of the peak in each moment depends, for the same polymer and solvent, on the amount of molecules that comes out in that moment. Hence, the height of the peak is proportional to the amount or mass m_i of the molecule that in a given time comes out from the column:

$$h_i = km_i \quad (3)$$

Or conversely:

$$m_i = k' h_i \quad (4)$$

where k' is a proportionality constant, identical for all the samples.

I.1.1. Molecular weight and SEC

A curve such as Figure 10, gives heights at different elution volumes, but indirectly, it also provides an image of the size distribution of different polymer chains in solution that form the sample, and consequently, the distribution of molecular weights.

It is very useful to obtain different average molecular weights that are characteristic for a fixed molecular weight distribution. Hence, the number average molecular weight is defined as:

$$\bar{M}_n = \frac{\sum_i N_i M_i}{\sum_i N_i} = \frac{\sum_i m_i}{\sum_i m_i / M_i} \quad (5)$$

where N_i refers to a molecules of molecular weight M_i . If we use the expression $m_i = k' h_i$, it transforms into:

$$\bar{M}_n = \frac{\sum_i h_i}{\sum_i h_i / M_i} \quad (6)$$

Similarly, the weight average molecular weight can also be calculated using the same variables:

$$\bar{M}_w = \frac{\sum_i m_i M_i}{\sum_i m_i} = \frac{\sum_i h_i M_i}{\sum_i h_i} \quad (7)$$

Another important parameter is the polydispersity index (PDI) which indicates the distribution of individual molecular masses in a sample. The PDI has a value equal to or greater than one. It can be written as:

$$PDI = \frac{\bar{M}_w}{\bar{M}_n} \quad (8)$$

In the chromatogram, the ordinate is the height h_i but the abscissa is the elution volume, proportional to the elution time and related with the size in solution of the molecules, although not with their molecular weights. This reasoning shows that this technique is not in principle an absolute technique for obtaining molecular weights, and so it requires the calibration with well-defined polymer standards (e.g. direct calibration) or the use of absolute-molecular-weight (e.g. light scattering) detectors.

I.1.2. Direct calibration

Under the same conditions of column, temperature, flow and solvent, different standards are introduced in the chromatogram, obtaining for each standard its elution

volume. Then, the logarithm of the molecular weight for each standard versus the elution volume is represented leading to a calibration curve (Figure 11).

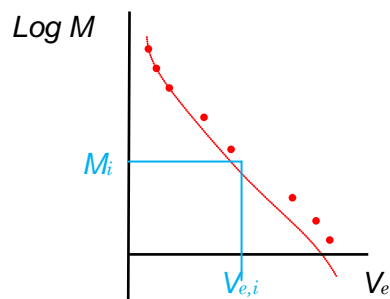


Figure 11. Direct calibration curve obtained from polymers with very low polydispersity and different molecular weights.

Is important to note that the direct calibration curve, obtained by a series of standards of a particular polymer, is valid, in principle, for that polymer.

SEC with direct calibration has become a very powerful technique to determine the apparent molecular weight of soft nanoparticles (most of the systems reviewed in section 1.1. have been measured by SEC with direct calibration). In this sense, it is very important to compare the molecular weight of the polymers precursor (M_w) and the molecular weight of the resulting nanoparticles (apparent molecular weight, M_{app}) under the same conditions of flow, solvent and temperature (Figure 12).

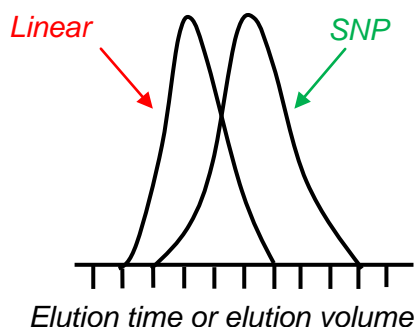


Figure 12. SEC of the linear polymer and the nanoparticle (SNP).

If only intramolecular cross-linking occurs, due to the chain collapse, the apparent molecular weight (M_{app}) should be lower than the molecular weight of its polymer

precursor (M_w), although in fact the actual molecular weight (as determined by light scattering) should remain largely unchanged. This reduction of the molecular weight after intramolecular chain collapse is a consequence of the reduction of its hydrodynamic volume, V_H .

I.1.3. Universal calibration

We have mentioned that SEC is based on the separation of molecules depending on their hydrodynamic volume. Taken into account that:

$$[\eta] = \frac{2.5V_H N_A}{M} \quad (9)$$

and

$$V_H = c \left\{ \frac{4}{3} \pi (\langle r^2 \rangle^{1/2})^3 \right\} \quad (10)$$

We can define a magnitude proportional to the mentioned hydrodynamic volume through this expression:

$$[\eta]M = \Phi \langle r^2 \rangle^{3/2} \quad (11)$$

The universal calibration is based on the idea that any two samples with the same size in solution (same hydrodynamic volume) will come out from the column at the same time, regardless of their chemical nature, having therefore the same elution volume. More explicitly, if a sample of any polymer is analyzed and having the direct calibration curve, done for example with polystyrene, one chain of the sample and other of the polystyrene will come out at the same time (in identical conditions of temperature, flow, solvent and column) if:

$$[\eta]_A M_A = [\eta]_B M_B \quad (12)$$

where A refers to the polymer used for the calibration and B refers to the sample to be analyzed.

This approach was demonstrated by Benoit and co-workers in the 70's, as can be appreciated in Figure 13, in which the curve is obtained when values of the result $[\eta]M$ for different polymers of different chemical nature and different morphologies (branched, linear, star...) are represented in the same diagram.

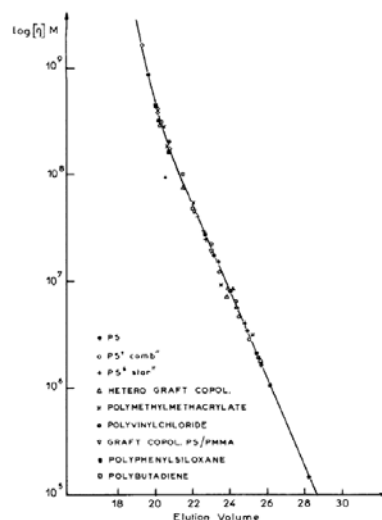


Figure 13. Illustration that proves that the elution volumen depends on $[\eta]M$ regardless of the polymer used.

Taking into account the Mark-Houwink expression $[\eta] = kM^\alpha$, the previous equation can be re-written as:

$$k_A M_A^{\alpha_A+1} = k_B M_B^{\alpha_B+1} \quad (13)$$

Where k and α are Mark-Houwink constants. Using these equations, it is very easy to obtain the different averages. Once we have the values of h_i and M_i (in this case $M_{i,A}$) from the chromatogram and from the calibration curve, we calculate $M_{i,B}$ using the last expression and immediately we obtain M_n and M_w through eqs. 6 and 7.

1.1.4. SEC as a direct technique for the determination of molecular weights

The need to use a universal calibration means that this technique is an indirect method for measuring molecular weights, since the separation of molecules is not based on molecular weight, but on the size. However, recently, new types of detectors have been introduced allowing the direct determination of molecular weights. The most common are viscosimetric and light scattering detectors, allowing the determination of the actual M_w and R_G values.

1.1.5. Complementary techniques to SEC

As previously indicated, the evolution of size reduction upon intramolecular cross-linking of individual chains to single-chain nanoparticles has been followed mainly by size exclusion chromatography (SEC) [7-13,15-20,28-30]. Other complementary

techniques are dynamic light scattering (providing R_H) [7,9,11,13-15,17-20,28,31, 32] and viscosimetry [13,14,19]. The size and morphology of the resulting nanoparticles due to the chain collapse process has been investigated by field emission scanning electron microscopy (FE-SEM) [7,8], atomic force microscopy (AFM) [9,10,13-16,18,28,29] and transmission electron microscopy (TEM) [12,17-19,31-33] whereas the cross-linking degree has been determined qualitatively by Fourier transform infrared spectroscopy [17,19,20,28] and quantitatively by nuclear magnetic resonance spectroscopy [7,11,28,32]. Thermal properties of the resulting nanoparticles have been determined mostly by differential scanning calorimetry [7,10,16,32] and thermogravimetric analysis [28]. Additionally, in some special cases, the intramolecular reaction process has been monitored by ultraviolet-visible [15,29,31] and photoluminescence [13,28] spectroscopies.

I.2. References

- [1] Nagarajan, R. *Symposium Series*, **2008**, 996, 2.
- [2] Eva Harth, Brooke Van Horn, Victor Y. Lee, David S. Germack, Chad P. Gonzales, Robert D. Miller, Craig J. Hawker, *J. Am. Chem. Soc.*, **2002**, 124, 8653.
- [3] Graeme Moad, Ezio Rizzardo, San H. Thang, *Acc. Chem. Res.*, **2008**, 41, 1133.
- [4] James E. Martin, B. E. Eichinger, *Macromolecules*, **1983**, 16, 1345.
- [5] V. A. Davankov, M. M. Ilyin, M. P. Tsyurupa, G. I. Timofeeva, L. V. Dubrovina, *Macromolecules*, **1996**, 29, 8398.
- [6] Jian Tao, Guojun Liu, *Macromolecules*, **1997**, 30, 2408.
- [7] David Mecerreyes, Victor Lee, Craig J. Hawker, James L. Hedrick, Andreas Wursch, Willi Volksen, Teddie Magbitang, Elbert Huang, Robert D. Miller, *Adv. Mater.*, **2001**, 13, 204.
- [8] Kyoung-sun PARK, Dae-yong KIM, Sang-kuk CHOI, Dong Hack SUH, *Jpn. J. Appl. Phys.*, **2003**, 42, 3877.
- [9] Jing Jiang, S. Thayumanavan, *Macromolecules*, **2005**, 38, 5886.
- [10] Anna E. Cherian, Frank C. Sun, Sergei S. Sheiko, Geoffrey W. Coates, *J. AM. CHEM. SOC.*, **2007**, 129, 11350.
- [11] Eva Harth, Brooke Van Horn, Victor Y. Lee, David S. Germack, Chad P. Gonzales, Robert D. Miller, Craig J. Hawker, *J. Am. Chem. Soc.*, **2002**, 124, 8653.
- [12] Teresa A. Croce, Sharon K. Hamilton, Matthew L. Chen, Hubert Muchalski, Eva Harth, *Macromolecules* **2007**, 40, 6028.
- [13] Chinessa T. Adkins, Hubert Muchalski, Eva Harth, *Macromolecules*, **2009**, 42, 5786.
- [14] Myungeun Seo, Benjamin J. Beck, Jos M. J. Paulusse, Craig J. Hawker, Sang Youl Kim, *Macromolecules*, **2008**, 41, 6413.
- [15] E. Johan Foster, Erik B. Berda, E. W. Meijer, *J. Am. Chem. Soc.*, **2009**, 131, 6964.

- [16] Erik B. Berda, E. Johan Foster, E. W. Meijer, *Macromolecules*, **2010**, *43*, 1430.
- [17] Alaitz Ruiz de Luzuriaga, Nerea Ormategui, Hans J. Grande, Ibon Odriozla, José A. Pomposo, Iraida Loinaz, *Macromol.r Rapid Commun.*, **2008**, *29*, 1156.
- [18] Lin Cheng, Guolin Hou, Jianjun Miao, Daoyong Chen, Ming Jiang, Lei Zhu, *Macromolecules*, **2008**, *41*, 8159.
- [19] Judit Eva Fleischer Radu, Levente Novak, John F. Hartmann, Neda Beheshti, Anna-Lena Kjoniksen, Bo Nyström and János Borbély, *Colloid Polym. Sci.*, **2008**, *286*, 365.
- [20] J. Benjamin Beck, Kato L. Killops, Taegon Kang, Kulandaivelu Sivanandan, Andrea Bayles, Michael E. Mackay, Karen L. Wooley, Craig J. Hawker, *Macromolecules*, **2009**, *42*, 5629.
- [21] Irma Perez-Baena, Iraida Loinaz, Daniel Padro, Ignacio García, Hans J. Grande, Ibon Odriozola, *J. Mater. Chem.*, **2010**, *20*, 6916.
- [22] Alaitz Ruiz de Luzuriaga, Irma Perez-Baena, Sarah Montes, Iraida Loinaz, Ibon Odriozola, Ignacio García, José A. Pomposo, *Macromol. Symp.*, **2010**, *296*, 303.
- [23] Halime Cengiz, Binnur Aydogan, Sahin Ates, Engin Acekalin, Yusuf Yagci, *Desi. Monomomers Polym.*, **2011**, *14*, 69.
- [24] Zoya Zarafshani, Jean-Francois Lutz, *Chem. Biol.*, **2009**, *2*, 133.
- [25] Alice E. van der Ende, Evan J. Kravitz, Eva Harth, *J. Am. Chem. Soc.*, **2008**, *130*, 8706.
- [26] Sadao Mori, Howard G. Barth, *Size exclusion chromatography*, Springer-Verlay Berlin Heidelberg, Germany **1999**.
- [27] Javier Areizaga, M. Milagros Cortazar, José M. Elorza, Juan J. Iruin. *Polimeros*, Editorial Síntesis, **2002**.
- [28] M. E. Mackay, T. T. Dao, A. Tuteja, D. L. Ho, B. V. Horn, H. C. Kim, C. J. Hawker, *Nature Mater.* **2003**, *2*, 762.
- [29] P. Taranekar, J. Y. Park, D. Patton, T. Fulghum, G. J. Ramon, R. Asvincula, *Adv. Mater.* **2006**, *18*, 2461.
- [30] G. Njikang, G. Liu, S. A. Curda, *Macromolecules* **2008**, *41*, 5697.

- [31] M. Bodnar, J. Hartmann, J. Borbely, *Biomacromolecules* **2006**, 7, 3030.
- [32] A. E. Van-der-Ende, E. Kravitz, E. Harth, *J. Am. Chem. Soc.* **2008**, 130, 8706.
- [33] G. Wulff, B. O. Chong, U. Kolb, *Angew. Chem. Int. Ed.* **2006**, 45, 2955.
- [34] J. Aitchison, J. A. C. Brown, *The Log-normal Distribution*, Cambridge University Press, **1957**.
- [35] Liu, J. W., Mackay, M. E., Duxbury, P. M., *Macromolecules*, **2009**, 42, 8534.
- [36] Perrin, F. *J. Phys. Radium*, **1936**, 7, 1.
- [37] Hansen, S. *J. Chem. Phys.*, **2001**, 121, 9111.